SOI Waveguide Based Optical Microsystems for Biophotonic Enzymatic Detection

ARVIND CHANDRASEKARAN

A Thesis

in

The Department

of

Mechanical and Industrial Engineering

Presented in partial fulfillment of the requirements for the
Degree of Master of Applied Science (Mechanical Engineering) at
Concordia University
Montreal, Quebec, Canada

March 2006

Library and
Archives Canada

Published Heritage
Branch

395 Wellington Street
Ottawa ON K1A 0N4
Canada

Bibliothèque et
Archives Canada

Direction du
Patrimoine de l'édition

395, rue Wellington
Ottawa ON K1A 0N4
Canada

Your file Votre référence
ISBN: 0-494-14301-0
Our file Notre référence
ISBN: 0-494-14301-0

NOTICE:
The author has granted a non-exclusive license allowing Library and Archives Canada to reproduce, publish, archive, preserve, conserve, communicate to the public by telecommunication or on the Internet, loan, distribute and sell theses worldwide, for commercial or non-commercial purposes, in microform, paper, electronic and/or any other formats.

The author retains copyright ownership and moral rights in this thesis. Neither the thesis nor substantial extracts from it may be printed or otherwise reproduced without the author's permission.

AVIS:
L'auteur a accordé une licence non exclusive permettant à la Bibliothèque et Archives Canada de reproduire, publier, archiver, sauvegarder, conserver, transmettre au public par télécommunication ou par l'Internet, prêter, distribuer et vendre des thèses partout dans le monde, à des fins commerciales ou autres, sur support microforme, papier, électronique et/ou autres formats.

L'auteur conserve la propriété du droit d'auteur et des droits moraux qui protège cette thèse. Ni la thèse ni des extraits substantiels de celle-ci ne doivent être imprimés ou autrement reproduits sans son autorisation.

In compliance with the Canadian Privacy Act some supporting forms may have been removed from this thesis.

While these forms may be included in the document page count, their removal does not represent any loss of content from the thesis.

Conformément à la loi canadienne sur la protection de la vie privée, quelques formulaires secondaires ont été enlevés de cette thèse.

Bien que ces formulaires aient inclus dans la pagination, il n'y aura aucun contenu manquant.

Canada

ABSTRACT

SOI waveguide based optical microsystems for biophotonic enzymatic detection

Arvind Chandrasekaran

Medical diagnostics using microsystems have gained a lot of importance in the recent years to develop a fully integrated, cost effective and easy-to-use sensor for in-situ detection of biomolecules. In the present work, the feasibility of developing an evanescent wave biosensor on Silicon-On-Insulator (SOI) platform through waveguide based Micro-Electro-Mechanical Systems (MEMS) is studied.

Miniaturization is one of the greatest advantages of using silicon as the biosensor material. The suitability of microfabrication and the ease of controlling waveguide geometries through different micromachining techniques render SOI as an ideal platform for evanescence based biosensing. Given the need to use infrared optical spectrum for silicon waveguiding, this thesis proposes biosensing through evanescence as suitable means for optically integrated SOI technology.

Herein, the proposed waveguide system has been modeled through Finite Difference (FD) technique for different evanescent field conditions and the results for modal parameters have been compared with Finite Element Modeling (FEM) simulated through FEMLAB. Scalar Beam Propagation Method (BPM) simulations have been carried out with R-Soft for rectangular and anisotropic waveguides and the results of propagation constants obtained from R-Soft have been compared with the FD method and FEM.

The microfabrication feasibility of the SOI waveguides has been demonstrated by two processes, namely, the SOI MicraGeM process technology, an industry defined process, and the in-house technique of anisotropic etching with Tetra Methyl Ammonium Hydroxide (TMAH). The post processing operations carried out on MicraGeM devices have been explained and fabrication results for both micromachining techniques have been presented through Scanning Electron Micrographs (SEM). In order to overcome the problem of surface roughness created in some microfabrication processes, a hybrid micromachining technique suitable for reducing surface roughness in different optical microsystems environment is presented. The improvement in surface roughness due to the proposed technique is demonstrated by experimental characterization of the roughness parameters using SEM and Atomic Force Microscopy (AFM).

The phenomenon of evanescence has been demonstrated with the enzyme Horse Radish Peroxidase (HRP), upon its reaction with Hydrogen Peroxide (H_2O_2). The optical behaviour of the enzyme and the antibody has been characterized under different wavelengths of light in order to facilitate different applications. Evanescence measurements have been carried out on rectangular rib waveguides fabricated through the MicraGeM technology and the anisotropic rib waveguides fabricated with TMAH micromachining. The phenomenon of evanescence due to the change in the refractive index of the cladding material has been demonstrated through BPM simulations with R-Soft.

ACKNOWLEDGEMENTS

At the outset, I sincerely thank Dr. Muthukumaran Packirisamy for having provided me an opportunity to work under his supervision and introducing me to the exciting field of Biophotonic MEMS. His guidance, practical ideas, encouragement and not to mention the financial support have been instrumental and inspirational in the successful completion of this thesis.

I would like to express my thanks to Dr. Ion Stiharu for his willingness to discuss any concept and for providing me valuable tips during the course of the thesis. I would like to thank Dr. Rama Bhat for his teaching instructions and his ideas during the courses of the academic program. My sincere thanks to Danius Juras, technical officer, and Mr. Gilles who have helped me with my experimental setups.

I am very grateful to Mr. Eric Duchesne of Ecole Polytechnique, Montreal for his invaluable assistance with the Scanning Electron Microscopy (SEM). I would like to thank Mr. Sébastien Chénard for his assistance with the oxidation process. It is time to acknowledge the assistance of Mr. Vito Logiudice, Mr. Neil Lemaire and Mr. Don Berry of Nanofab laboratory, McGill University, Montreal for their invaluable assistance with the diamond saw dicing and photolithography. It has been a wonderful experience to work at the microfabrication laboratories at the Ecole Polytechnique and McGill University during the course of the thesis. I would also like to thank Mr. Heng Wang, Concordia University, for his assistance with the Atomic Force Microscopy (AFM).

It has been my pleasure to be a part of the Optical Microsystems laboratory of Concordia University. It has been an enjoyable experience to work with colleagues Mr. Avinash Bhaskar, Mr. Amritsar Jeetender Singh, Mr. Gino Rinaldi, Mr. Rakesh Kalyanaraman, Mr. Ashwin Acharya, Mr. Kim Young Soo and the list goes on. I would like to appreciate the help of all my friends here in Montreal, who have made my sojourn a very memorable one so far.

Above all, I wish to express my heartfelt thanks to my parents Mr. Chandrasekaran and Mrs. Neela Chandrasekaran, and my sister Aparna, for encouraging me, supporting me and motivating me right throughout my career.

Dedicated to my parents

TABLE OF CONTENTS

CHAPTER 2 - MODELING OF WAVEGUIDE BASED BIOSENSORS AND ROUGHNESS INFLUENCE

CHAPTER 3 - FABRICATION OF SOI WAVEGUIDE BASED MOEMS

CHAPTER 4- HYBRID MICROMACHINING

CHAPTER 5 – BIOPHOTONIC ENZYMATIC DETECTION

CHAPTER 6 – CONCLUSIONS AND FUTURE WORKS

APPENDIX

LIST OF FIGURES

LIST OF TABLES

NOMENCLATURE

AFM	Atomic Force Microscope
BPM	Beam Propagation Method
CH_3COOH	Acetic Acid
CIP	Centre for Integrated Photonics
CMC	Canadian Microelectronics Corporation
CMOS	Complementary Metal Oxide Semiconductor
CsOH	Cesium Hydroxide
dpi	Dots per inch
DNA	Deoxyribo Nucleic Acid
DRIE	Deep Reactive Ion Etching
EDP	Ethylenediamine Pyrocatechol
EM	Electro-Magnetic wave
FD	Finite Difference
FEA	Finite Element Analysis
FEM	Finite Element Modeling
Fe_2O_3	Ferrous Oxide
FET	Field Effect Transistor
GRIN	Graded Index Lens
HCl	Hydrochloric Acid
HNA	Hydrofluoric and Nitric Acid
H_2O_2	Hydrogen Peroxide

HRP	Horse Radish Peroxidase
ICP	Inductively Coupled Plasma
IPA	Isopropyl Alcohol
IUPAC	International Union of Pure and Applied Chemistry
KOH	Potassium Hydroxide
LiOH	Lithium Hydroxide
μTAS	Micro-Total Analysis Systems
MEMS	Micro -Electro-Mechanical Systems
MicraGeM	Micralyne Generalized MEMS
MOEMS	Micro-Opto-Electro-Mechanical Systems
MST	Micro Systems Technology
MUMPs	Multi-User MEMS Process System
MZI	Mach-Zehnder Interferometer
NH_4OH	Ammonium Hydroxide
OADM	Optical Add/Drop Multiplexers
OEIC	Opto Electronic Integrated Circuits
OSA	Optical Spectrum Analyzer
psi	Pounds per square inch
PDE	Partial Differential Equation
RI	Refractive Index
RIE	Reactive Ion Etching
RPM	Revolutions Per Minute
SCREAM	Single Crystal Reactive Etching And Metallization

SCSi	Single Crystal Silicon
SEM	Scanning Electron Microscopy
Si	Silicon
SiF_4	Silicon Tetrafluoride
SiO_2	Silicon dioxide
SOI	Silicon-on-Insulator
SPR	Surface Plasmon Resonance
TE	Transverse Electric
TM	Transverse Magnetic
TMAH	Tetra Methyl Ammonium Hydroxide
UV	Ultra Violet Light
XeF_2	Xenon difluoride

LIST OF SYMBOLS

α	Waveguide side-wall taper angle
α_{ab}	Absorption coefficient
α_{ev}	Evanescence coefficient in cm^{-1}
α_m	Angle made by the photomask with respect to the wafer flat.
α_{sc}	Attenuation factor or scattering loss coefficient for waveguides
α_{sw}	Scattering coefficient in waveguides
β	Propagation constant
β_{ab}	Absorbance loss in dB/cm
β_{FD}	Propagation constant obtained with FD computation
β_{FEM}	Propagation constant obtained with FEM analysis
β_{ev}	Total evanescent light loss in dB
β_{HRP}	Evanescent light loss due to HRP , in dB/cm
β_{RS}	Propagation constant obtained with R-Soft
β_{sf}	Scattering loss in non-waveguide based devices (dB/cm)
β_{sp}	Evanescent light loss in dB/cm due to the specimen (HRP or H_2O_2)
β_{sw}	Optical loss due to scattering in waveguide (dB/cm)
γ	Denoted by the expression $\frac{dn_2k_0\sqrt{2}}{W_s}$
∇	Differential operator
ε	Permittivity of medium

ε_o	Permittivity of free space
ξ	Locus of points parallel to the boundaries in FD computation
η	Locus of points along the boundaries in FD computation
λ	Wavelength of light
μ	Permeability of medium
μ_o	Permeability of free space
μl	micro litres
μm	micrometers
μs	micro seconds
ϕ	Generalized Electric or Magnetic field
ϕ_e	Field relations for external boundary conditions
ρ	Surface roughness in non-waveguide based systems
$\Re_{\lambda}$	Resistivity of the photodetector measured in Amp/W
σ	Standard deviation of roughness variation
θ_i	Angle of incidence of light in non-waveguide based systems
θ_{ic}	Angle of incidence of the light with respect to the waveguide axis
ω	Frequency of the wave oscillation
A_{λ}	Absorbance measured with light of wavelength λ
c	Velocity of light in vacuum, 3 x 10^8 m/s
°C	Degree Celsius
cm	Centimeters
$C(u)$	Auto correlation function for waveguide sidewall roughness

d	Waveguide width
d_p	The depth of penetration of an evanescent wave
dB	Decibels
dx	Incremental distances between the grid points in the x-direction
dy	Incremental distances between the grid points in the y-direction
D_λ	Dark Intensity
Da	Daltons, 1 Da = 1.660540 x 10^{-24} kg
e	Constant of value 2.71828
E	Electric field of Electro-Magnetic wave
EP	Evanescent power loss computed by BPM
f	Under-relaxation factor for FD computation
$f(x_s,\gamma)$	Roughness function for waveguides
hr	Hour
H	Magnetic field of Electro-Magnetic wave
H_w	Height of SOI rib waveguide used in FEMLAB modeling
Hz	Hertz
i	Coordinates of points along x-axis
$I_{i,j}$	Numerator function for calculation of β in the FD technique
j	Coordinates of points along y-axis
k	Wavenumber
k_0	Wavenumber of free space
$\bar{k}$	Reference wave number given by $\bar{k} = k_0\beta$

kDa	kilo Daltons
kg	kilograms
kHz	kilo Hertz
l_{ab}	Absorbance length
L_c	Autocorrelation length
L_{HRP}	Length of the waveguide covered by HRP
L_{sp}	Length of the waveguide covered by the specimen (HRP or H_2O_2)
m	meters
mid	Locus of points forming the line of symmetry along any axis in FD computation
min	Minutes
n_1	Refractive index of waveguide core
n_2	Refractive index of clad
n_3	Refractive index of covering medium for waveguide
n_{eff}	Effective refractive index
n_m	Refractive index of the medium
nm	Nanometers
num	Numerator function given by $(\nabla^2\phi + k^2n^2\phi)\phi$
N	Refractive Index of covering medium taken for FEM analysis
P_0	Input light power
P_t	Power of light transmitted through the glass slides
P_{input}	Input Power
P_{output}	Output Power

P_{pd}	Power of light measured in Watts , calculated from photodetector
ΔP_{HRP}	Evanescent power loss due to HRP
ΔP_{sp}	Power loss due to the evanescence produced by the specimen
R	(dx/dy) in FD computation
R_a	Average surface roughness value
R_L	Load resistance in the photodetector
R_{rms}	Root-Mean-Square roughness value
R_λ	Intensity of light passing through the reference medium
S_λ	Intensity of light passing through the sample
t	Height of the waveguide core in µm
t1	Height of rib of waveguide core in µm
TP	Total power in the optical field
u	Slow varying field given by $\phi(x,y,z) = u(x,y,z)e^{i\bar{k}z}$.
$\bar{u}$	Position of surface roughness along the distance of the waveguide
U	Denoted by the expression $d\sqrt{n_1^2 k_0^2 - \beta^2}$
V	Denoted by the expression $k_0\ d\sqrt{n_1^2\ - n_2^2}$
w	Width of rib of waveguide core in µm
W	Watts
WP	Waveguide power calculated across the area of the waveguide
W_s	Denoted by the expression $d\sqrt{\beta^2 - n_2^2 k_0^2}$
W_w	Width of SOI rib waveguide used in FEMLAB modeling

x_s	Denoted by the expression $\frac{W_s L_c}{d}$
x	x-direction in the 3D axis
y	y-direction in the 3D axis
z	z-direction in the 3D axis

Chapter 1

Introduction

1.1 Introduction to MOEMS

Micro Systems Technology (MST) or Micro Electro Mechanical Systems (MEMS) has allowed the integration of mechanical, optical and electronic functions through Micro Opto Electro Mechanical Systems (MOEMS). In general, MOEMS is assumed to be a micro device which deals with light. MOEMS derives its functionality from the miniaturization of optical, electronics and mechanical elements.

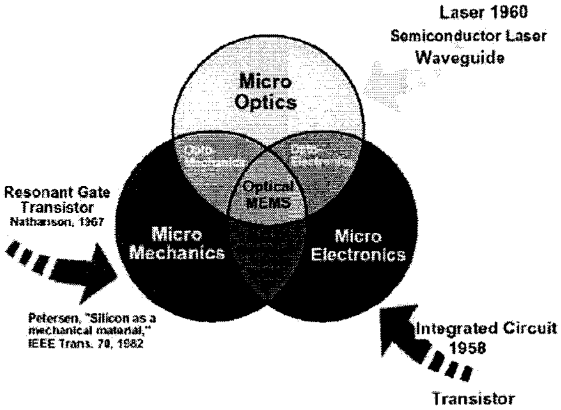

Figure 1.1: Fusion of three technologies in the history of MOEMS [1].

Non-conventional machining and semiconductor process technology have opened up new arenas for MOEMS to such an extent that the field has a tremendous potential to enhance its applicability given the ability of the system to be integrated with other complementary modules of fluidic, thermal and biophotonic functions, which opens up the possibility for several applications in the areas of aerospace, telecommunications, vehicle systems, biomedical sciences and biosensing [2]. Examples of optics-based micro devices include the interferometers, beam splitters, micro bends, optical gyroscopes, photodiodes, micromirrors, Optical Add/Drop Multiplexers (OADM) and microswitches. Integrated microphotonic devices can now be fabricated with many optical components integrated on single chip [2].

It should be accepted that MOEMS is the technology for the future because the optomechanical solution has many advantages over traditional MEMS. The achievement of significant optical attenuation even by a small variation in the mechanical movement of the device, low insertion loss, small cross-talk and the availability of wide bandwidth in free space are some of the features which have made MOEMS successful [2].

1.1.1 Silicon based MOEMS

Silicon based optoelectronics in the telecommunication wavelength has gained a significant momentum over the past few years. The considerable potential of Si-based optoelectronic integrated circuits (OEIC's) is beginning to be realized and this area holds promise for a wide range of applications from high-capacity on-chip optical interconnects to optical communications receivers and ultimately transmitters [3].

With very good mechanical, optical and electronic properties of silicon material, silicon based micro devices form an ideal platform for integrated MOEMS with possible electronic circuits and microprocessors [4]. Silicon waveguides with high refractive index difference offer considerable advantages with miniaturization due to low optical losses [5]. The naturally occurring oxide of silicon (SiO_2) is an excellent insulator material and has a very high etching selectivity compared to silicon, facilitating easy micromachining of silicon. Alternatively, the compatibility of industrial CMOS (Complementary Metal Oxide Semiconductor) technology to the MOEMS is enhanced by the use of silicon based materials, such as, silicon nitride, silicon dioxide, polysilicon etc., as the CMOS enables fabrication of MOEMS components within the same process flow [6].

Silicon-On-Insulator (SOI) devices based integrated waveguide systems has formed the backbone of many microphotonic and nanophotonic components [7]. The important parameters which have to be taken into consideration in waveguiding are the refractive index of the core, its electro-optical effects, optical losses and the transparency regions. Given the huge refractive index difference between the silicon and the insulator oxide layer, SOI system provides low loss waveguides (<0.2 dB cm^{-1}) with single-mode operation and low birefringence [8]. Appropriate geometry with the use of an asymmetric waveguide allows bend radius as short as 0.1 mm [9]. SOI based waveguides can be fabricated in smaller dimensions in the near-micrometer ranges which is of great advantage in integrating a number of optical components within a small area. Many kinds of SOI based waveguide devices have been fabricated, such as, optical waveguide switches [10], optical directional couplers [11], star couplers [12], photodetectors [13], Mach-Zehnder interferometers [8], photonic crystal waveguides [14] etc. Commercialization of these SOI based devices has been active with photonic industries for the realization of integrated optoelectronic devices.

In the present work, SOI has been used for fabricating waveguides for biophotonic applications. The microfabrication has been carried out by conventional chemical wet etching process and also the MicraGeM (Micralyne Generalized MEMS) process [15], which is discussed about in the further sections.

1.2 Introduction to Biosensors and Biophotonics

Biotechnology and medical diagnosis are currently in need of devices for the continuous monitoring and selective detection of biological species. The advent of MOEMS devices enables the use of various microstructures in biosensing applications with unique benefits in the detection of chemical and biological specimen.

According to a recently proposed IUPAC (International Union of Pure and Applied Chemistry) definition [16], "A biosensor is a self-contained integrated device which is capable of providing specific quantitative or semi-quantitative analytical information using a biological recognition element (biochemical receptor) which is in direct spatial contact with a transducer element". The application of biomatrices for tailoring biosensors and bioelectronics is of substantial importance [17]. MOEMS based biosensors can be defined as optoelectronic detection based micro devices that use chemical and biological species for detection and quantification of targets of interest by optical methods based upon the presence, activity or the concentration of an analyte [18].

A biosensor should be clearly distinguished from a bioanalytical system, which requires additional processing steps, such as reagent addition. Furthermore, a biosensor should be distinguished from a bioprobe which is either disposable after one measurement, i.e. single use, or unable to continuously monitor the analyte concentration. These biosensors based devices find extensive usage in chemical detection, clinical diagnostics, food processing, environmental analysis and forensic applications.

Biophotonics is a specialized area of biotechnology which is defined by the techniques of photon-based imaging, detection and experimental manipulation of biological materials. The key areas of biophotonics are optical sectioning microscopy, photon limited microscopy, fluorescent probes, spectral and lifetime imaging, caged bioactive probes and non-imaging experimental optical techniques [19].

1.2.1 Methods of biosensing

Modern optical biosensors have evolved from the developments made in communication industry, information technology and molecular biology. There have been numerous biophotonic detection methods which have been employed for biosensing. The major phenomena of optical biosensing can be short-listed as absorbance, reflectance, luminescence, chemiluminescence, scattering, and evanescence. All the biophotonic detection techniques are based upon these above mentioned optical principles.

Many other techniques have been devised to be used in conjunction with the optical technology for biosensing. Lin et al. [20] have described the integration of capillary electrophoresis with fiber optic technology for the detection of analytes. Surface Plasmon Resonance (SPR) is one of the important biophotonic techniques which has been used widely with the combination of fiber-optic technology in past years [21]. There have been other techniques of detection of the biological pathogens as well, which include the photonic disk resonators [22,23], and cantilever response methods [24, 25].

1.2.2 Specimens used in biosensing

The application of the biosensor depends upon the type of specimens which are used for. A biosensor is constructed for the recognition of a particular kind of specimen set, the performance of which may not be compatible when used with other specimen even though same detection principle is used.

The bioreceptor component can be classified into five groups [26], namely, Enzymes, Antibodies/Antigens, Nucleic acids, Cellular structures or whole cells and Biomimetic receptors. Enzymes are proteins that catalyze specific chemical reactions. These can be used in a purified form and can be present in a micro-organism or in a live tissue. The mechanisms of operation of these bioreceptors can involve catalytic transformation of the analyte into a sensor-detectable product, detection of an analyte that acts as enzyme inhibitor or activator, or evaluation of the modification of enzyme properties upon interaction with the analyte [27].

An antigen is a molecule that triggers the immune response of an organism to produce an antibody. The biosensing is based upon the specific and high affinity interaction of antibody binding with antigen. A tracer is used to generate signals, for e.g., fluorescent molecules, radioisotope or any enzyme. The recognition process for Nucleic acids is based on the complementary nature of base pairs (adenine and thymine or cytosine and guanine) of adjacent strands in the double helix of DNA. These sensors are usually known as genosensors. Alternatively, the recognition signals can be generated by the interaction of small pollutants with DNA [26, 28]. The Cellular structures could be whole cells i.e. the whole microorganism such as bacteria or fungi, or a specific cellular component, or a non-catalytic receptor protein, to be used as the biorecognition element. Biomimetic receptors are genetically engineered molecules [26], artificial membranes or Molecularly Imprinted Polymers (MIP), which mimic a bioreceptor. The most recent investigations in artificial receptors include application of a combined approach of computer (molecular) modeling and MIP and the application of combinatorial synthesis for the development of new sensing layers [26]. In the case of biosensing with different varieties of bioreceptors, some of the biomolecule sets which have been experimented for biosensing using waveguide based systems are in Table 1.1. While the vast majority of evanescence based waveguides make use of specific antibodies and/or nucleic acid probes for analyte detection, other types of recognition molecules, such as, enzymes, receptors, gangliosides, peptides and nucleic acid aptamers, complex and simple sugars, and antimicrobial peptides are also used in this process [18] .

Table 1.1 : Sample of the biomolecule sets used for biosensing using waveguide based biophotonic devices.

Recognition molecule	Analyte detected	Method of detection	Ref. No.
Hapten	Carbaryl	Mach-Zehnder Interferometry	29
Ruthenium –Ligand complex	Glucose oxidase	Fluorescence	30
PMMA clad layer	Bacteria	Metal Clad Leaky Waveguide	31
Polyaniline	HCl /Ammonia	Evanescence	32
Anti-ricin IgG antibody	Ricin	Evanescence	33
Cyclotetrachromotropylene	Urease/ Acetylcholine Esterase	Evanescence	34
HRP Homovanillic Acid	Hydrogen Peroxide	Fluorescence	35
Oligonucleotide-Antibody	DNA Polymerase	Surface Plasmon Resonance	36
Anti-HRP	Bovine Serum Albumin	Grating coupler	37
Anti –Methotrexate	Blood plasma, MTT	Young`s interferometry	37
Antimicrobial peptides a	E. coli, Salmonella typhimurium	Fluorescence	38
Peptide aptamer	Staphylococcal enterotoxin B (SEB)	Evanescence	39
Antibody anti-hCG	Human Choriogonadotropin	Surface Plasmon Resonance	40
Anti-rabbit IgG, MPTMS*, TMB**	Stanozolol dopant	Surface Plasmon Resonance	41
Captan	glutathione-S-transferase	Absorbance	42

* Mercaptopropyltrimethoxysilane

** 3,3,5,5-tetramethylbenzidine

1.2.3 Challenges in Biophotonics

However, there are some challenges which need to be addressed in biosensing. Primarily, the issue of immobilization of the bio-component with the substrate is important for the proper biosensing. The other main problem in the effective usage of biosensors is the coupling of the biological species with the device. It is essential to bind the analyte onto the biosensor for effective biosensing functionality of the device.

Immobilization of biological specimen has also been carried out with soft lithography methods. One of the lithography techniques is the microcontact patterning [43] which relies on transfer or specimens such as thiols, proteins etc from an inked elastomeric stamp to selected regions of the substrate. Micropatterning with photolithography has been carried out on several biological species such as Biotin-Avidin [44], a conducting polymer poly(3,4-ethylene-dioxythiophene) [45], copolymeric hyrogels like Polymethacrylic acid and Polyethylene Glycol Dimethacrylate [46], Rabbit Immunoglobulin G and Bovine Serum Albumin [47]. The other common methods of immobilization of the biomolecules include the surface adsorption, molecule entrapment, covalent binding and intermolecular cross-linking [48].

The integration of microfluidics is a significant aspect of biosensing because it not only introduces the biological environment into the micro-optical system but also enables working with smaller sample volumes conveniently. There have been some works which were carried out in this direction in order to introduce microfluidics into biophotonic modules. Figure 1.2 shows biophotonic microfluidic plates integrating optical waveguides beneath microfluidic channels to enable optical coupling of fluids, developed by the Centre for Integrated Photonics (CIP), United Kingdom [49]. Micromolding in capillaries (MIMIC) is a technique which was developed to fabricate three dimensional structures for allowing the fluid flow in the channels, by using a PDMS mould [50]. This technique was later enhanced to pattern biomolecules with submicron resolution on a variety of substrates including gold, glass and polystyrene [51]. Patterning of enzymes on the substrate of the device has also been achieved by restriction of fluid flow to the desired regions of the substrate [43]. The same research group has also experimented with laminar flow patterning of cells in which two liquids have been allowed to flow adjacently without mixing and thereby enabling the patterning of not only the cells, but the culture medium itself in a highly controllable fashion. Though a lot of work has been done in biosensing, research and development on silicon based biophotonic devices in the micro scale is still an ongoing process.

Figure 1.2: Integrated microfluidic biophotonic wafer fabricated at the Centre for Integrated Photonics, United Kingdom [49].

1.2.4 Classification of MOEMS based biosensors

In general, MOEMS based biophotonic devices can be grouped into two broad classifications of optical microsystems, namely, the waveguide based devices and the non- waveguide based devices. The waveguide based systems operate on the principle of total internal reflection of light in the waveguides. Some examples of such systems are the Mach-Zehnder interferometers, optical resonators, multiplexers, demultiplexers, OADM and optical gyroscopes. The non-waveguide based optical microsystems such as Fabry-Perot interferometers and optical switches operate in free space wherein light is reflected off the surface of the device.

Both the above mentioned systems can be fabricated by standard microfabrication techniques. But for optimal performance of the device, it is essential to minimize the optical transmission losses induced from some of the fabrication defects arising due to lithographic mismatches and surface roughness. Thus, it is very important to obtain a control over the manufacturing process and thereby improve the performance of the microfabricated optical microsystems.

1.3 Fabrication of MOEMS – Micromachining techniques

Microfabrication is a very essential and a crucial phase of MOEMS process technology, by means of which different parameters of the microsystems such as the geometry, surface roughness etc. are controlled. Etching is an important micromachining process, which involves physical or chemical removal of a material. The etching can be isotropic, i.e. equal etching rates on all the directions, and anisotropic etching, wherein the etch rate on a substrate is dependant upon the direction of the crystallographic planes along which the etching occurs.

Apart from the well known industry-defined microfabrication processes, such as, MUMPs [52], SCREAM [53], and Sandia Ultra Planar technology techniques, there are other processes which have been developed for the successful fabrication of integrated MOEMS devices, like the Protolyne [54], MicraGeM etc. High sensitivity biosensing devices have also been fabricated with precise designing using the CMOS microelectronics technology [55]. The Protolyne is a glass chip prototyping technology provided by Micralyne [54]. This technology enables the user to develop a network of bulk-micromachined channels and features with eight reservoirs in glass substrate for microfluidic applications as shown in Figure 1.3, which could be integrated for biophotonic applications.

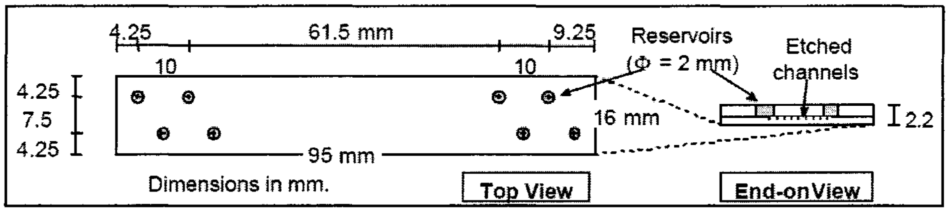

Figure 1.3: Protolyne Microfluidic chip layout [54].

Micromachining can be broadly classified as bulk micromachining and surface micromachining, wherein the former method employs 'bulk' removal of material from the substrate and the latter method involves processing done on a substrate in the form of deposition or selective removal of layers of materials [56].

1.3.1 Surface Micromachining

Surface micromachining has developed since the early 1980's from academic "proof-of-concept" demonstrations into a commercially important technology [57]. This process is based on selective building up and removal of different layers of materials. However, the bulk of the substrate remains unetched.

There have been several surface micromachining techniques which have been employed in order to fabricate microstructures. MUMPS is one of the standard surface-micromachining processes, developed by the MCNC, has been widely used in the MEMS community to make polysilicon-based, moveable microstructures [58], such as mirrors [59], micro power sources [60,61] and even microchannels for BioMEMS applications [62] using three polysilicon layers, two oxide layers and a metal layer. Sato et al. [63] have used the electrochemical deposition method inorder to fabricate an x-ray imaging sensor. Lift off process is another technique which is used mainly for deposition of metals on the substrate in selective regions using a negative mask. The Sandia-Ultra Planar multi level technology, developed by the Sandia national laboratories [64] is a five layer polysilicon surface micromachining technique which can be used in fabrication of complex MEMS mechanisms. Figure 1.4a shows a micro gear fabricated at the Sandia laboratories using this process. Figure 1.4b shows a glass microchannel fabricated with surface micromachining technique at the Berkley Sensor and actuator center, located at California [62].

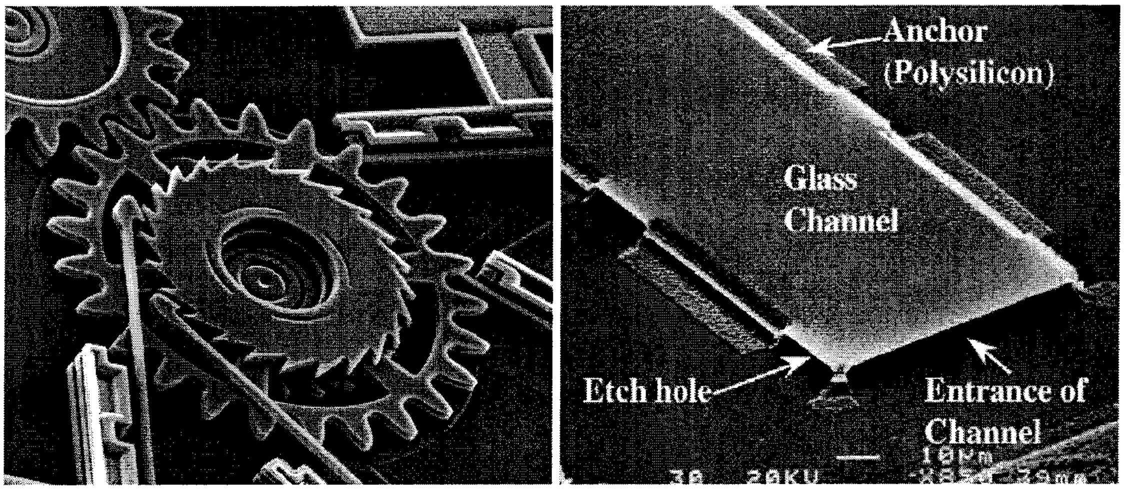

Figure: 1.4: (a) SEM of ratcheting system that was fabricated in the five-layer technology at Sandia national laboratories. (b) A SEM micrograph showing a glass microchannel fabricated at Berkley Centre for Sensors and Actuators [62].

Other devices which have been fabricated using the surface micromachining technique include Fabry Perot interferometer [65], piezoresistive microcantilever [66], Field Effect Transistor (FET) pressure sensor [67] and thermally driven micropump [68].

There are three key challenges in fabrication of microstructures using surface micromachining [69]:

1. Control of stress and stress gradient in the structural layer to avoid bending or buckling of the released microstructure.
2. High selectivity of the sacrificial layer etchant to functional layers
3. Avoidance of sticking of the released microstructure to the substrate.

Technologies that merge different surface micromachining processes with various electronic processes have also been demonstrated [70,71]. Although they require complex fabrication processes, there are major incentives in integrating electronics and surface microstructures [72].

1.3.2 Bulk Micromachining

As mentioned before, bulk micromachining refers to the bulk removal of the material from the substrate by the process called etching. There are several etching methods applied in bulk micromachining process [73]. Single Crystal Reactive Etching and Metallization (SCREAM), a bulk micromachining technology patented by the McDonald's research group at the Cornell University [74], which can be used for fabricating high aspect ratio beams, suspended beams and also embedded channels into single crystal silicon substrate. In Plasma/Reactive Ion Etching (RIE) [73], the chemical reactions are driven by the applied RF potentials and the gas formed from the plasma reacts with the surface atoms of the substrate forming compounds which are subsequently removed from the surface. Though the machining results in some amount of underetching of the sample, methods have been devised to control this phenomenon during the process. However, the selectivity of etching is lower, which makes it difficult to control the process. Another method called the Deep Reactive Ion Etching (DRIE) is a high aspect ratio silicon etching method which uses Inductively Coupled Plasma (ICP) source to supplement the RIE system. Many devices such as optical switches, vertical micromirrors and inertial sensors with high aspect ratios have been micromachined with DRIE [75-77].

As mentioned before, the classification of etching also branches out to the selectivity of the etchant to the direction of etch, namely, isotropic and anisotropic etching. The non-plasma based dry isotropic etching of silicon is achieved by typically fluorine containing gases like xenon difluoride and interhalogens such as BrF_3 and ClF_3. Isotropic wet silicon etching is done with "HNA" (a combination of hydrofluoric acid HF, nitric acid HNO_3, and acetic acid CH_3COOH) [78]. Other anisotropic etchants of silicon include Tetra Methyl Ammonium Hydroxide (TMAH), potassium hydroxide (KOH), sodium hydroxide (NaOH), lithium hydroxide (LiOH), cesium hydroxide (CsOH) and ammonium hydroxide (NH_4OH) [79].

1.3.2.1 Isotropic etching with XeF_2

A simple and inexpensive etching process is the gas phase etching carried out with xenon difluoride, XeF_2. Xenon difluoride is chosen as an etchant for its properties such as isotropic etching of silicon, high selectivity to etching of Aluminum, silicon dioxide, silicon nitride and photoresist, and high controllability of etching via temperature and partial pressure of the reactants. XeF_2 is a white crystal at room temperature and atmospheric pressure. However, at a pressure of around 4 torr at room temperature [6], it sublimates and isotropically etches silicon as given by the reaction:

$$2XeF_2 + Si \rightarrow 2Xe + SiF_4 \tag{1.1}$$

There is no need for any physical excitation in the etching process. Figure 1.5 shows the scheme of the XeF_2 etch setup. The samples to be etched are to be carefully dehydrated prior to etching because XeF_2 upon reaction with water or vapor forms HF (Hydrofluoric acid) during the reaction, which is highly toxic. Considering the propensity of HF to etch the oxide layer, the formation of HF will also pose a problem during etching of silicon dioxide masked surfaces. The process of dehydration is also essential in order to prevent the formation of polymer silicon fluoride, which could stop or slow down the etching, drastically [80].

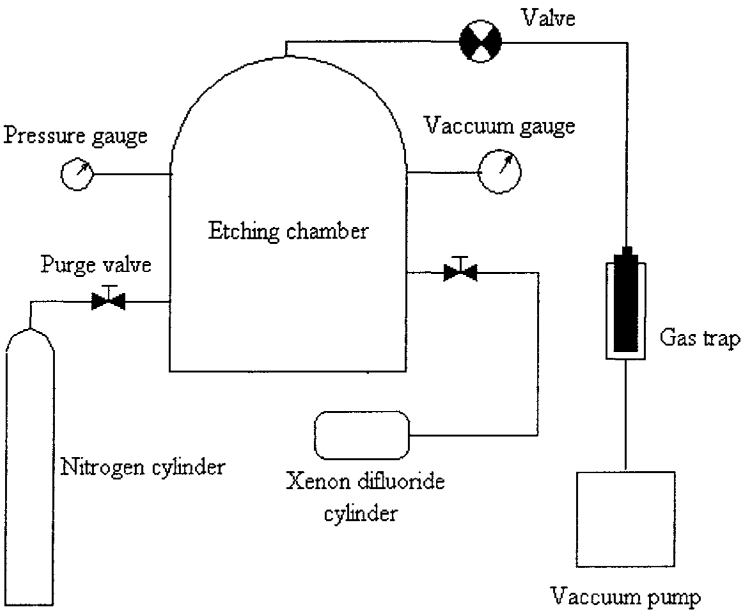

Figure 1.5: Schematic of Xenon difluoride pulse etching setup.

There are many advantages [81] of XeF_2 gas phase etching of silicon as follows:

(i) XeF_2 isotropically etches silicon with the etch rate being limited by the incident flux. By carefully combining both wet and dry etching processes, overhanging structures can be realised.

(ii) The etch rates for XeF_2 can be varied from 1~3 μm/min. Higher etch rates can be easily achieved with simple hardware and vacuum control system, operating at room temperature when compared to the RIE system.

(iii) The use of XeF_2 can be an environmentally conducive etching process because a large amount of XeF_2 can be converted to SiF_4 and Xe which can be recycled for use again, whereas, in the case of RIE, a large portion of the parent fluorocarbon gas is pumped into the atmosphere.

(iv) XeF_2 is very selective in attacking silicon dioxide. When the etching of silicon can be controlled, the silicon dioxide layers act as etch stop for the XeF_2. This is a very important property of XeF_2 which enables microfabrication of Silicon-On-Insulator (SOI) wafers with this process.

However, as mentioned before, the XeF_2 bulk etching method is not conducive to many microsystems applications, especially in the optical arena due to high surface roughness. Hence, a hybrid micromachining technique has been proposed in this thesis, in order to reduce the surface roughness caused by XeF_2 etching.

1.3.3 Choice of microfabrication process

It is important to choose a fabrication process that suits each application. While unrestricted geometry of microfabrication can be achieved with isotropic etching, the shape of the structure and hence the design is limited in the case of anisotropic etching due to the very nature of the process itself. For example, the waveguide structures that are applied in typical optical microsystems are schematically shown in Figure 1.6. But the control over the shape of the channel that is micromachined is absolutely necessary and in such cases anisotropic etching is not favorable.

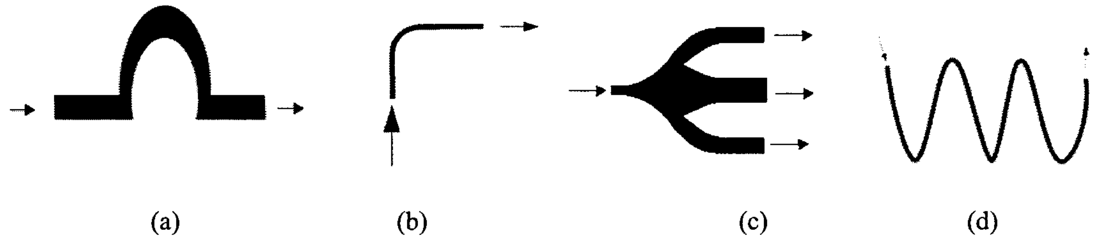
(a) (b) (c) (d)

Figure 1.6: Schematic diagram of some of the typically curved waveguides required to be micromachined (a) straight waveguide (b) bent waveguide (c) waveguide splitter (d) curved waveguide (Arrow indicates the direction of light transmission).

Possible methods which could be employed for fabricating such structures with bulk micromachining etching techniques are deep reactive ion etching and wet/dry chemical etching. The complexity in the geometries of structures is an important issue in deciding the microfabrication process. A combination of both these dry etching processes, such as reactive ion etching and gas phase XeF_2 etching has been demonstrated for microfabrication [82].

Another factor which has to be taken into consideration while deciding the microfabrication process in order to fabricate a device is surface roughness of the device after etching. Roughness could be sometimes useful in the case of microfluidic applications with the need for increased turbulence and hence better mixing. But microfabrication induced roughness poses a major problem in the design of optical micro devices like waveguides and micromirrors which require highly smooth surfaces. The surface roughness plays an important role in the performance of optical microsystems as optical characteristics of MOEMS, such as scattering loss, insertion loss, return loss, noise and cross talk are influenced primarily by this parameter. The potent problem with using the XeF_2 is the roughness of the etched surface which aggravates with continued etching [6]. Hence, this process cannot be employed wholly in order to microfabricate optical microsystems. Therefore, it is essential for the user to decide upon the microfabrication technique that should be employed for etching a particular system.

In this thesis, anisotropic etching of silicon has been carried out with TMAH for the microfabrication of silicon waveguides. The procedure and the etching setup are explained and detailed in Chapter 3. TMAH has also been used for hybrid micromachining process in order to smoothen out the rough surfaces resulting from isotropic etching. This procedure is presented in Chapter 4.

1.4 Packaging

One of the most crucial phases of developing a MOEMS device is packaging. The significance of packaging is echoed for the synthesis of many biophotonic microsystems such as Lab-on-a-chip devices or Micro-Total Analysis Systems (μTAS), wherein it is essential to integrate different individual components with due consideration of cost, performance and reliability. Packaging is important for the success of a microsystem because of the following advantages it offers:

(i) *Protection from environment*: Environmental pollutants of size of nearly the same order of magnitude as the microsystem may cause a lot of problems for the devices. Hence it is required that the device be protected from foreign elements.

(ii) *Mechanical support*: Packaging enables the isolation of the device from thermal and mechanical shocks, vibrations, and other physical damages.

(iii) *Integration with other microsystems*: Electrical integration of a device with other systems is made possible with packaging. Electrical bondings are also essential in order to actuate certain devices. Thus, packaging is very important for dynamic structures.

(iv) *Commercialization*: Successful device operation and ease of device handling coupled with cost effectiveness by means of proper packaging will directly enable better commercialization of the product.

1.4.1 Types of MEMS packaging

It cannot be laid down as a standard to define a particular packaging style for the MEMS devices because each of the applications demand a different type of packaging in order to optimize the performance and meet the requirements of the system. However, in general, the different types of MEMS packaging can be classified as metal packaging, ceramic packaging, plastic packaging, flip-chip packaging [83] and thin-film multi-layer packaging. Integrated multichip packaging integrating MEMS with other microelectronic technologies can be achieved by Chip-On-Flex and the Multi-Chip-Module process [84]. Packaging is now enabled with simulation softwares [85] which enable performance of various analyses like thermal, stress/strain, deformation, vibrational etc., thus reducing the number of prototyping cycles usually required during the packaging process.

1.5 Testing of MOEMS based biosensors

It is essential to corroborate the results of the simulation and analytical modeling with the experimental results for the development of successful MOEMS devices. This calls for the testing of the proposed biophotonic microsystem under different conditions in order to study the performance and the repeatability of the device along with the other practical issues, which have to be taken into consideration in the design and fabrication methods, so as to improve upon the performance of the device.

The main factors which have to be taken into consideration for any biophotonic testing are the choice of biological specimen to be tested with and the wavelength of light chosen. Not all species are optically active in a particular wavelength range of light and hence the optical detection may not be possible under those circumstances. The different enzyme sets which have been used for experiments, has been listed previously and the principle of evanescence has been demonstrated in several of those works using the techniques such as SPR, MZI and fluorescence. But, it is essential to characterize the optical activity of a particular enzyme before testing.

1.6 Rationale and scope of the thesis

Optical microsystems and microphotonic devices offer a tremendous scope in the detection of various biological and chemical specimens. However, the success of this technology will be fully realized only with the confidence in the utilization of these devices for the specific applications.

Taking a note of that idea, this thesis has been built upon with the following objectives:

- To demonstrate the feasibility of developing integrated microfluidic optical biophotonic MEMS device on SOI platform.

- To study the application of evanescent field principle on silicon waveguide based microsystems for biosensing.

- To improve the modeling and design of silicon waveguides and compare them with the theoretical modeling using Finite Difference Method, Finite Element Method and Beam Propagation Method.

- To study the feasibility of using standard micromachining techniques and the MicraGEM process technology for the synthesis of the waveguide based biophotonic devices and the effects of fabrication tolerance in the performance of the device.

- To design and experimentally characterize the optically integrated circuits and suitable components in order to validate the feasibility.

- To understand the possibility of applying optically integrated SOI based microsystems platform for biophotonic applications.

- To develop a hybrid micromachining technique in order to improve the surface roughness of XeF_2 micromachined silicon waveguides and make cost effective optically integrated SOI technology.

1.7 Layout of the thesis

An introduction to MOEMS and Biophotonics is provided in Chapter 1 along with the literature study. This chapter also briefs about the different microfabrication procedures available for MOEMS fabrication, packaging of micro and a brief introduction to the biophotonic testing. The need for the present work to develop a waveguide based biosensor on SOI platform is discussed in the rationale of the thesis.

The design and modelling of anisotropic waveguides for evanescence based biosensing is given in Chapter 2. The principle of evanescence is introduced and the possibility of evanescence based biosensing with the anisotropic waveguides is discussed. The modeling of the evanescent waveguide using Finite Difference (FD) method is presented. The modelling includes the analysis of both the straight waveguide approach to solve for waveguide modes, is extended to the tapered waveguide. The analytical study also includes Finite Element Modeling (FEM), in order to study the effective propagation indices of the light under different evanescent conditions and birefringence calculation. The Beam Propagation study is also detailed in this chapter along with the method of BPM and the results of simulation. The results of propagation constants obtained with the different methods of simulation are compared.

The fabrication feasibility of anisotropic SOI waveguides is detailed in Chapter 3. Two different fabrication methods are discussed, namely, the SOI MicraGEM process and the anisotropic etching using TMAH. The strategic design of MicraGeM waveguides and the optimized post processing technique employed are explained. The various steps involved in the anisotropic microfabrication process flow are discussed in detail. The fabrication results and the post processing techniques are explained along with the SEM pictures of the various fabricated designs.

In Chapter 4, a hybrid micromachining process suitable for roughness reduction in optical microsystems is explained. The improvement in surface roughness due to the proposed technique is demonstrated by experimental characterization of the roughness parameters using Scanning Electron Microscope (SEM) and Atomic Force Microscope (AFM) and the effect of surface roughness on the waveguide based and the non waveguide based optical microsystem environments is also discussed.

The experimental biophotonic testing procedure and the test results are presented in Chapter 5. The optical characterization of protein Horse Radish Peroxidase (HRP) and its antibody Hydrogen Peroxide (H_2O_2) by absorbance method under different wavelengths is detailed. The evanescence testing procedure employed on the waveguides fabricated through MicraGeM process and the SOI anisotropically etched waveguides are explained and the results are presented. The evanescence principle is demonstrated on the different waveguides and the comparison between the experimental evanescent loss and the predicted loss from BPM simulations is also presented.

The conclusions and future works are presented in Chapter 6.

Chapter 2

Modeling of Waveguide based Biosensing and Roughness Influence

2.1 Introduction

An optical waveguide is a light conduit consisting of slab, strip or circular dielectric structure, through which Electromagnetic (EM) waves are transported [86]. A waveguide consists of two layers, namely, the core and the clad. Waveguide core is the dielectric medium through which the light is guided and cladding is referred to the dielectric medium which surrounds the core. The refractive index of a dielectric material is the ratio of velocity of electromagnetic radiation in vacuum to the velocity of EM radiation through that medium [87]. The basic principle behind waveguiding is Total Internal Reflection (TIR) wherein, when light enters the waveguide core that has a higher refractive index than the clad, it undergoes a series of reflection at the walls of the core before emerging out, as illustrated schematically in Figure 2.1.

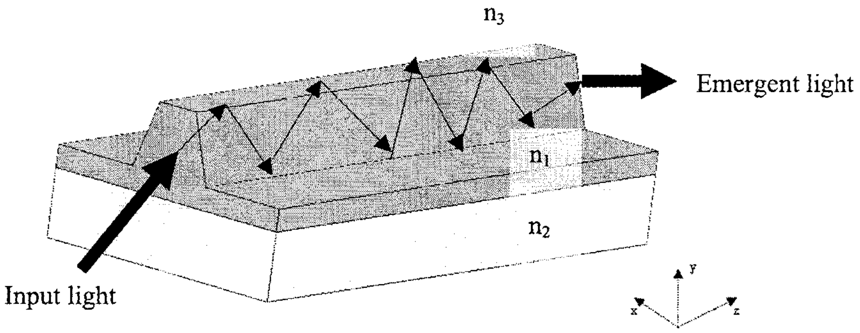

Figure 2.1: Illustration of waveguiding with Total Internal Reflection phenomenon.

The waveguides can be classified as rib/ridge, slab, circular and buried waveguides. The different waveguide configurations include straight, bent, branched, Mach-Zehnder, etc., as shown in Figure 2.2.

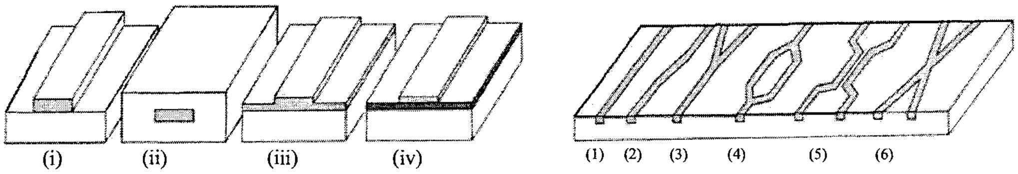

Figure 2.2: Schematic [86] of (a) different types of the waveguides (i) strip (ii) buried (iii) rib (iv) slab (b) some of the geometries of waveguides (1) straight (2) s-bend (3) Y-branched (4) Mach-Zehnder (5) Directional couplers (6) Intersecting waveguides. The dark region represents the waveguide core.

Waveguide based devices form a significant classification of MOEMS based biosensors. The various advantages [88] of waveguide based biosensors, such as, immunity to electromagnetic interferences, ease of optical integration with other systems and the integration of these devices with microfluidics have made them an exciting class of biosensors. These waveguide based devices operate on different optical principles, such as, Surface Plasmon Resonance (SPR), fluorescence, interferometry, etc. as discussed in Section 1. Herein, the principle of evanescence is employed for biosensing.

2.2 Principle of evanescent wave coupling

Whenever light is propagated through a waveguide, some light escapes out of the waveguide into the surrounding medium. This light field, which is lost out of the waveguide at the core-cladding interface, is known as the evanescent field. This light in the evanescent field is considered as an optical loss as it is not guided through the waveguide. The schematic representation of evanescent field is as shown in Figure 2.3.

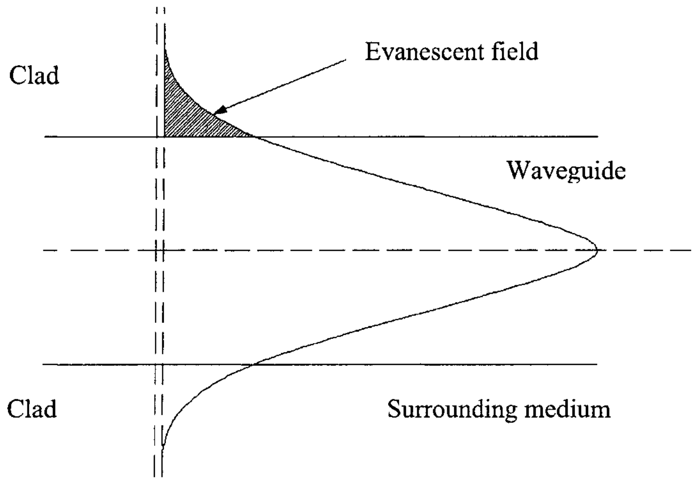

Figure 2.3: Schematic representation of the evanescent field theory

Evanescent field can be created under two conditions, that is, when the refractive index of the cladding is higher than that of the core and secondly when the refractive index of the cladding is lesser than the core refractive index. In the former situation, since the refractive index of the cladding is higher, the guided wave mode is transferred to radiation mode and the resulting partially leaky waveguide system depends upon the intensity modulation because of the radiation field. In the second situation, when the refractive index of the cladding is lesser than that of the core, the evanescent field can still be created through the intensity modulation caused by the light absorption of the evanescent field energy in the cladding. The interaction between the evanescent field in the cladding and external perturbation results in the attenuation of the guided light in the waveguide core through absorption and fluorescence [88].

The depth of penetration (d_p) of an evanescent wave is the distance at which the amplitude of evanescent field wave is (1/e) times the amplitude at the surface [89]. Mathematically, the depth of penetration is given by the expression

$$d_p = \frac{\lambda}{2\pi[(n_1^2 Sin^2\theta_{ic} - n_2^2)]^{1/2}} \tag{2.1}$$

Here, θ_{ic} is the angle of incidence of the light with respect to the waveguide axis, n_1 and n_2 are the refractive indices of the core and the clad respectively. From the above expression, for a wavelength of light 1550 nm propagated through a Silicon waveguide of refractive index of the core to be 3.48, the depth of penetration is found to be around 70 nm.

The evanescent wave biosensors show a great potential for the sensing of biomolecular interactions and the fact that there have not been any labeling requirements have made the evanescent wave biosensors very useful for a wide range of applications in biomedical, environmental, industrial, chemical and biological warfare to genomic and proteomics fields [90]. Though there are several optical biosensing methods, the feasibility of controlling the evanescence through anisotropic etching renders this technique useful for fabrication of SOI waveguide based biosensors.

2.2.1 Maxwell's equations for rib waveguides

The electromagnetic wave propagation along the optical waveguides for the case of no charge and no current conditions is described by the Maxwell's equations, which can be given by the following relations:

$$\nabla \bullet \vec{E} = 0 \tag{2.2a}$$

$$\nabla \bullet \vec{H} = 0 \tag{2.2b}$$

$$\nabla \times \vec{E} = \frac{-\partial \vec{H}}{\partial t} \tag{2.2c}$$

$$\nabla \times \vec{H} = \mu\varepsilon \frac{\partial \vec{E}}{\partial t} \tag{2.2d}$$

where, $\vec{E}$ and $\vec{H}$ are the electric and magnetic field vectors respectively and μ, ε are the permeability and permittivity of free space respectively. The above equations are a set of coupled PDE's. These equations are decoupled as follows. When the curl of Equation (2.2c) is taken

$$\nabla \times (\nabla \times \vec{E}) = \nabla(\nabla \bullet \vec{E}) - \nabla^2 \vec{E} = \nabla \times \left(\frac{-\partial \vec{H}}{\partial t} \right) = -\frac{\partial}{\partial t}\left(\nabla \times \vec{H}\right) \tag{2.3}$$

Since $\nabla \bullet \vec{E} = 0$ for no charge condition, the above equation becomes

$$-\nabla^2 \vec{E} = -\frac{\partial}{\partial t}\left(\nabla \times \vec{H}\right) \text{ or } \nabla^2 \vec{E} - \frac{\partial}{\partial t}\left(\nabla \times \vec{H}\right) = 0 \tag{2.4}$$

By substituting Equation 2.2d in the above Equation 2.4,

$$\nabla^2 \vec{E} - \frac{\partial}{\partial t}\left(\mu\varepsilon \frac{\partial \vec{E}}{\partial t} \right) = 0 \Rightarrow \nabla^2 \vec{E} - \mu\varepsilon \left(\frac{\partial^2 \vec{E}}{\partial t^2} \right) = 0$$

$$\therefore \nabla^2 \vec{E} - \frac{1}{c^2}\left(\frac{\partial^2 \vec{E}}{\partial t^2} \right) = 0 \tag{2.5}$$

Here, c is the velocity of light in vacuum given by $c = \sqrt{\mu\varepsilon}$. Similarly, when the curl of Equation 2.2d is considered,

$$\nabla \times (\nabla \times \vec{H}) = \nabla(\nabla \bullet \vec{H}) - \nabla^2 \vec{H} = \nabla \times \left(\mu\varepsilon \frac{\partial \vec{E}}{\partial t} \right) \tag{2.6}$$

Since $\nabla \bullet \vec{H} = 0$,

$$\nabla^2 \vec{H} + \nabla \times \left(\mu\varepsilon \frac{\partial \vec{E}}{\partial t} \right) = 0 \text{ or } \nabla^2 \vec{H} + \mu\varepsilon \left(\nabla \times \frac{\partial \vec{E}}{\partial t} \right) = 0 \Rightarrow \nabla^2 \vec{H} + \mu\varepsilon \frac{\partial}{\partial t} \left(\nabla \times \vec{E} \right) = 0 \qquad (2.7)$$

Substituting Equation 2.2c and rewriting the above Equation 2.7, the following equation is obtained

$$\nabla^2 \vec{H} - \mu\varepsilon \left(\frac{\partial^2 \vec{H}}{\partial t^2} \right) = 0 \text{ or } \nabla^2 \vec{H} - \frac{1}{c^2} \left(\frac{\partial^2 \vec{H}}{\partial t^2} \right) = 0 \qquad (2.8)$$

Equations 2.5 and 2.8 represent second order decoupled Maxwell's equations for waveguiding. The order of the equation has increased as a result of decoupling the electric and magnetic fields. In general, Equations 2.5 and 2.8 can be written as

$$\nabla^2 \phi - \frac{1}{c^2} \frac{\partial^2 \phi}{\partial t^2} = 0 \qquad (2.9)$$

where ϕ is taken as the generalized form of either the electric or magnetic field and c is the velocity of light in vacuum.

If monochromatic light of constant frequency ω is considered in the present problem, then $\phi(x,y,z,t) = \phi(x,y,z)e^{-j\omega t}$. Substituting this relation in Equation 2.9, the decoupled Maxwell's equation can be written as an eigenvalue equation as

$$\nabla^2 \phi + \frac{\omega^2}{c^2} \phi = 0 \qquad (2.10)$$

The above expression is popularly known as the Helmholtz equation.

Let the term $\frac{\omega^2}{c^2}$ be denoted as k^2, where k is given as nk_0, with n being the refractive index of the medium and k_0 known as wavenumber of the free space. Now, the eigenvalue equation can be framed as

$$\nabla^2\phi(x,y,z)+k^2\phi(x,y,z)=0\text{, or }[\nabla^2+k^2]\phi(x,y,z)=0 \qquad (2.11)$$

where k is the eigenvalue and ϕ is the eigenvector. If it is assumed that

$\phi(x, y, z) = \phi(x,y)e^{-j\beta z}$,

then the Equation 2.11 can be written as

$$\nabla^2\phi(x,y)+[n^2k_0^2-\beta^2]\phi(x,y)=0, \qquad (2.12)$$

which is the general equation for 2-dimensional (2D) wave propagation along the z-axis. Here, n is the refractive index of the medium through which the light is propagating. This equation is valid over the entire x-y section. The term β is called the propagation constant and can be represented as $\beta = n_{eff}\, k_0$, where n_{eff} is called the effective index of propagation. The condition for the propagation of light through a waveguide is given as $n_2k_0 < \beta < n_1k_0$, where n_1 and n_2 are respectively the refractive indices of the waveguide core and the clad. When the value of β is beyond this range, the light enters into the radiation mode, as described in Section 2.2.

The Electromagnetic waves could be either Transverse Electric (TE) waves or Transverse Magnetic (TM) waves. In the case of TE waves, there is no electric field component in the direction of propagation and similarly with the TM waves, there is no magnetic field component along the direction of propagation of the wave. Therefore,

For TE waves, $\vec{\boldsymbol{E}} = (0, \boldsymbol{E}_y, 0)$ and $\vec{\boldsymbol{H}} = (\boldsymbol{H}_x, 0, \boldsymbol{H}_z)$

For TM waves, $\vec{\boldsymbol{E}} = (\boldsymbol{E}_x, 0, \boldsymbol{E}_z)$ and $\vec{\boldsymbol{H}} = (0, \boldsymbol{H}_y, 0)$

The birefringence is defined as the difference in the effective index of propagation between the TE and TM waves.

2.2.2 Design of evanescent wave biosensor

When the medium of waveguiding, i.e., the core of the waveguide is silicon of refractive index 3.48, it is not possible to allow evanescence out of waveguide by using any biological specimen which has a higher refractive index than silicon. Therefore, it is not possible to construct an evanescent wave biosensor using the former of the evanescent field approaches mentioned in Section 2.2. However it is still possible to use silicon waveguides as biosensors when the principle of evanescence is applied with the refractive index of the modified cladding material being lesser than the core, by allowing the interaction of the biomolecules with the propagating modes at the waveguide surface.

The principle of operation of the proposed biosensor is as shown in Figure 2.4. The light guided through the waveguide is attenuated through the evanescent field because of the presence of enzymes. This attenuation depends upon the optical properties of the enzyme present. When the concentration of the enzyme is changed by means of a reaction with corresponding anti-enzymes or dilution in any other form, the changes in the optical properties also cause a variation of the attenuation of the guided light. The study of this variation can be made use of as a biosensing technique in detecting the change in concentration of the analyte which is proportional to the intensity attenuation. This principle is applied for the fabrication of evanescence based biosensor.

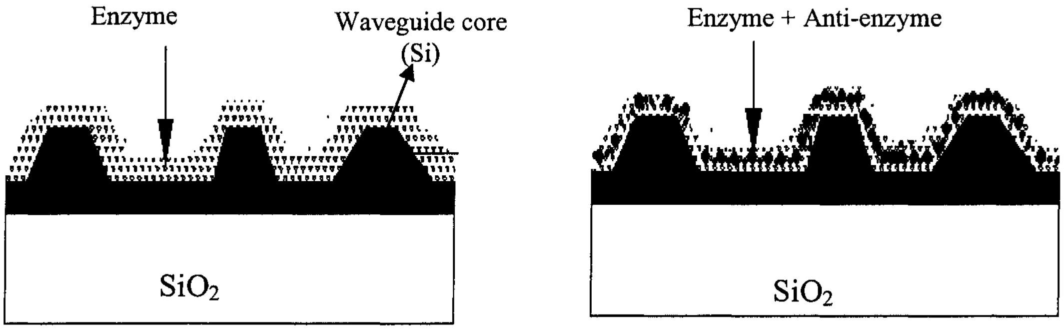

Figure 2.4: A schematic of evanescent wave biosensor on SOI platform.

However, in order to obtain significant evanescence, it is important that the evanescent field is sufficiently large enough so as to allow enough interaction between the optical mode and the biological environment producing the evanescence. Thus, the geometric parameters on which the evanescence depends upon are the length of the waveguide and the area of interaction between the biological environment and the waveguide. In the present work, SOI rib waveguides are used in order to achieve these conditions. By anisotropic etching, it is possible to fabricate a tapered rib waveguide, also incorporating microfluidic channels across them. Depending upon the sidewall angle of the rib waveguide, the area of interaction between the biological samples and the waveguide changes and the evanescence vary. Thus, the evanescent wave coupling can be controlled by the method of fabrication of the waveguide, and optical and geometric properties of the waveguide.

2.3 Modeling of evanescent waveguide biosensors

Modal analysis is a critical part of the design and modeling of semiconductor optoelectronic devices, which provides the details about the different modes of propagation, the mode shapes, the propagation constants and the relative modal excitations with respect to the input field by the overlap integrals [91]. There have been several techniques which have been applied in order to find out the propagation constants and the confinement factors of evanescence based optical waveguide devices.

Propagation of optical power in waveguides can be investigated by solving Maxwell's equations subjected to the appropriate boundary conditions [92]. There exist many numerical results because of different approaches to the problem and also different discretization and boundary conditions. So, no particular method can claim to be more accurate than others. For the tapered waveguide structures, no precise analytic solution has been obtained because there are no particular boundary conditions which are applicable to the taper. So, approximate methods have to be employed in solving for modal parameters in tapered waveguide systems.

The evanescent field condition can be produced in the waveguide system by varying the following parameters, namely, the refractive index of the cladding material, the length of the evanescent field and the area of interaction between the waveguide core and the biological specimens. The study of evanescence by varying the evanescent field length is carried out by beam propagation methods. In practical applications of SOI based sensors, it is possible to increase the evanescent coupling by inclining the side wall of the waveguide, thereby introducing a side-wall taper in order to increase the sensing area.

In this chapter, three approaches to the modal analysis has been discussed, namely, the Finite Difference Method (FDM), the Finite Element Method (FEM) with FEMLAB [93] and Beam Propagation Method with R-Soft [94], in order to find the propagation constants of the waveguides under the different conditions of evanescence.

2.3.1 The Finite Difference (FD) technique

The Finite Difference (FD) method is one of the methods for solving Partial Differential Equations (PDE's). This method has been successfully implemented in many areas of micro-photonics, physics and engineering because of its simplicity. It has proven very effective for calculations of the propagation constants and field profiles of the modes supported by a wide range of waveguide technologies [95]. More recently, it has also been applied in the time domain and in beam propagation [96].

Herein, a solution of the scalar wave equation by the FD method is presented. A comprehensive description of the method of obtaining the different modes of propagation is detailed. The boundary conditions are discussed and a comparison of the results with the Finite Element Modeling (FEM) using FEMLAB [93] is also presented. The method proposed by Delage [92] was used for waveguides with straight side-walls. However, it is very essential to model the waveguide system with taper for study of evanescence.

Hence, this work extends the straight waveguide approach for modelling the tapered waveguides with improved evanescent coupling.

2.3.1.1 Input parameters and meshing

Maxwell's vector wave equation for sinusoidal waves applied to non-magnetic semiconductor is given by the expression [92]

$$\nabla^2 \vec{E} + k_0^2 n^2 \vec{E} = -\nabla \bullet \left(\frac{\nabla n^2}{n^2} \right) \bullet \vec{E} \tag{2.13a}$$

$$\nabla^2 \overrightarrow{H} + k_0^2 n^2 \overrightarrow{H} = -\left(\frac{\nabla n^2}{n^2} \right) \times \nabla \times \overrightarrow{H} \tag{2.13b}$$

where $\vec{E}$ and $\overrightarrow{H}$ are respectively the electric and magnetic field vectors, n is the refractive index of the medium, and k_0 is the free space wave number.

If the variation of the refractive index represented by the term $(\nabla n^2 / n^2)$ is negligible, both the above equations lead to the same scalar equation. Furthermore, if a modal propagation is considered for waveguides with symmetry in the direction of the propagation, the following expression is obtained for scalar field

$$\nabla^2 \phi(x, y) + k_0^2 n^2 \phi(x, y) = k_0^2 \beta^2 \phi(x, y) \tag{2.14}$$

where ϕ is the field amplitude representing either the electric or the magnetic field. The direction of propagation is along z-direction and β is the propagation constant. This scalar wave equation is discretized accordingly in order to calculate the field values at each of the grid points.

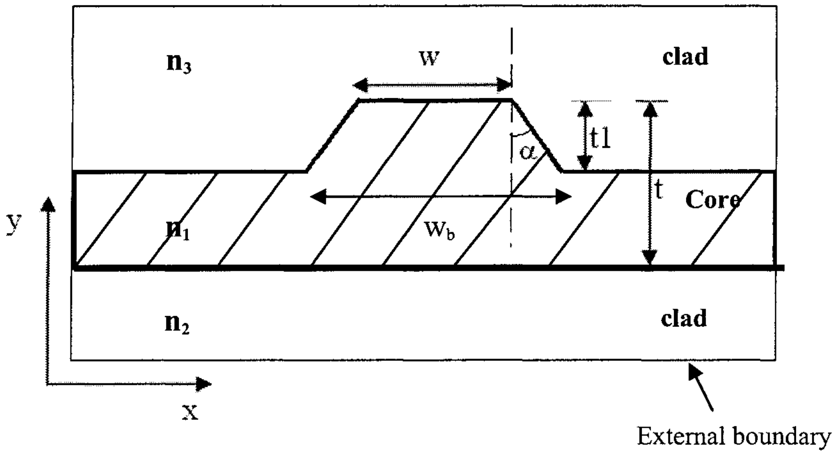

Figure 2.5: Different parameters of a tapered rib waveguide taken for Finite Difference computation.

The following parameters are used for the demonstration of the present modelling on a geometry shown in Figure 2.5.

n_1 = 3.48, refractive index of silicon core.

n_2 = 1.48, refractive index of Silicon dioxide insulator.

n_3 = refractive index of the cladding material

tl = height of rib of core in μm

t = height of core in μm

w = width of rib of core in μm

α = side-wall taper angle.

w_b= width of the waveguide base

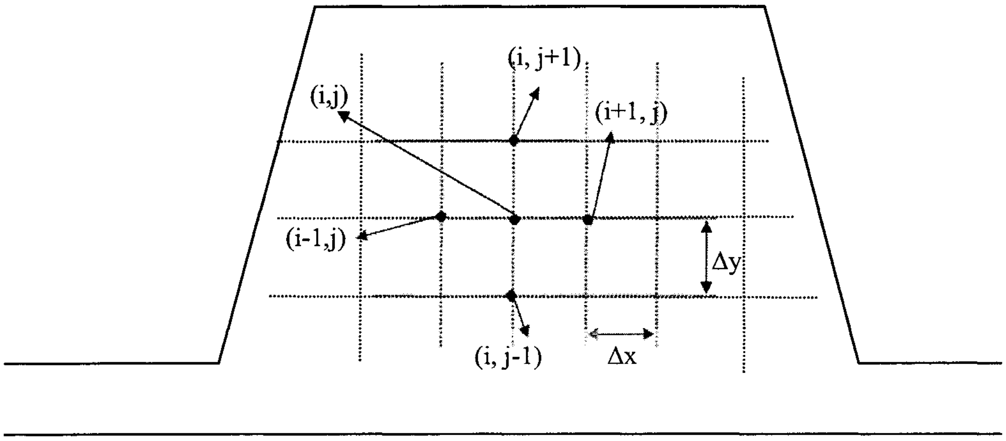

Figure 2.6: Distribution of grid points in the computational domain

2.3.1.2 Finite difference relations

The scalar wave Equation 2.14 is discretized [92] in order to formulate the finite difference relation. The operator ∇^2 is given by the following finite difference relation:

$$\nabla^2 \phi_{i,j} = \frac{\phi_{i+1,j} + \phi_{i-1,j} - 2\phi_{i,j}}{dx^2} + \frac{\phi_{i,j+1} + \phi_{i,j-1} - 2\phi_{i,j}}{dy^2} \tag{2.15}$$

where i and j are the co-ordinates of the grid points along the x and y axes respectively, $\phi_{i,j}$ is the field value at the grid point (i,j), dx and dy are the incremental distances between the grid points in the x and y directions respectively. For any point (i,j) in the grid, the neighboring 4 points are given by (i+1,j), (i-1,j), (i,j+1) and (i, j-1) as shown in Figure 2.6. The scalar wave Equation 2.14 is rewritten to give the following basic finite difference relation where the amplitude of the field at each point of the grid $\phi_{i,j}$, except those points for which a particular boundary condition applies, is given by a weighted average of the value of the four neighboring grid points [90].

$$\phi_{i,j}^{(n+1)} = \frac{\phi_{i+1,j}^{(n)} + \phi_{i-1,j}^{(n)} + R^2(\phi_{i,j+1}^{(n)} + \phi_{i,j-1}^{(n)})}{2 + 2R^2 + k_0^2 dx^2(\beta^2 - n^2)} \tag{2.16}$$

In the above equation, $R^2 = \left(\frac{dx}{dy}\right)^2$. The field value of specified points is calculated from above relation using the values of previous iteration and stored accordingly in the matrix $\phi^{(n+1)}$ of the order Nnx x Nny, where Nnx and Nny are the total number of points along the x and y axes respectively. In the meshing scheme used, the mesh points coincide with the boundaries. Continuity relations are applied for all these boundary points (i=η or j=η) and the function is continuous at a boundary if the value of the function and its first derivative are continuous and same at the boundary on both sides. η+ and η- are points (η + Δη) and (η- Δη) respectively just near the boundaries, such that Δη →0.

$$\left(\frac{\partial\phi}{\partial x}\right)_{\eta+} = \left(\frac{\partial\phi}{\partial x}\right)_{\eta+1} - dx\left(\frac{\partial^2\phi}{\partial x^2}\right)_{\eta+1} \tag{2.17a}$$

$$\left(\frac{\partial\phi}{\partial x}\right)_{\eta-} = \left(\frac{\partial\phi}{\partial x}\right)_{\eta-1} + dx\left(\frac{\partial^2\phi}{\partial x^2}\right)_{\eta-1} \tag{2.17b}$$

The following relations are applied for boundaries parallel to y and x axis, respectively.

$$\phi_{\eta,j} = \frac{4(\phi_{\eta+1,j} + \phi_{\eta-1,j}) - (\phi_{\eta+2,j} + \phi_{\eta-2,j})}{6} \tag{2.18a}$$

$$\phi_{i,\eta} = \frac{4(\phi_{i,\eta+1} + \phi_{i,\eta-1}) - (\phi_{i,\eta+2} + \phi_{i,\eta-2})}{6} \tag{2.18b}$$

The relations given in Equations 2.18(a) and 2.18(b) are applied along the boundary lines as shown in Figure 2.7. At the corners where a boundary parallel to y-axis meets one parallel to x-axis, the following linear combination of the two relations is applied.

$$\phi_{\xi x,\xi y} = \frac{\phi_{\eta\leftarrow\xi x,j\leftarrow\xi y} + R^2\phi_{i\leftarrow\xi x,\eta\leftarrow\xi y}}{1 + R^2} \tag{2.19}$$

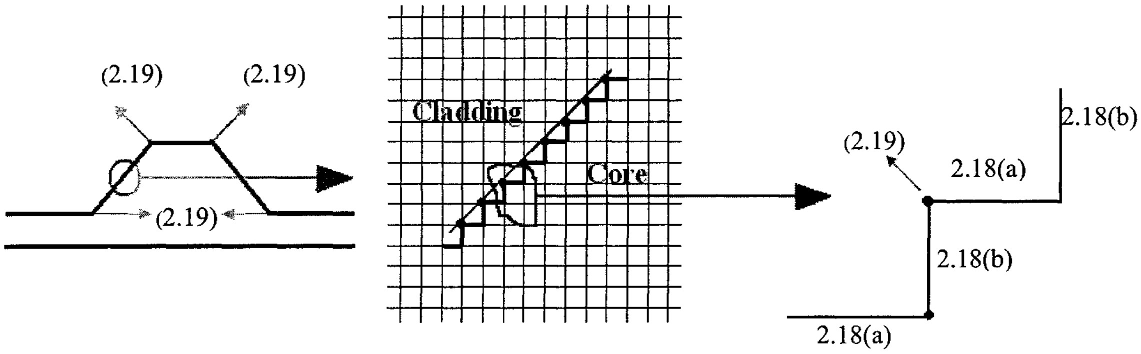

Figure 2.7: Tapered section of waveguide as modeled in the Finite Difference method.

The Equations 2.18 and 2.19 are applied to the points shown in the Figure 2.7. The boundary conditions for the tapered section are applied as shown in Figure 2.7. Herein, the taper is discretized into many steps of finer spacing. The Equation (2.18a) and (2.18b) are applied at the grids on the horizontal and vertical boundaries while the Equation 2.19 is applied at the corner grid points denoted by (2.19) in Figure 2.7. Since there is no concrete boundary condition definition for the slopes of the waveguide, this approximation is carried out so as to create boundary conditions along the waveguide tapers by computing them as small steps.

Using the above equations, the field value within the waveguide can be estimated. The field in a region far from the guiding region is usually set at zero, but the values are not absolutely negligible. This problem can be alleviated if external boundary conditions are introduced based on the assumption of an exponential decrease of the field. Thus, in the case of these external boundaries that define the outer boundary of the computation region, the field is calculated by assuming an exponential decay of the field value from the waveguide core. Thus, the fields on external boundaries are computed as given by the following relations:

$$\phi(x,y) = \phi(x_{\max}, y)\exp[-a_1|x - x_{\max}|], \quad 0 \le x \le x_{\max} \tag{2.20a}$$

$$\phi(x,y) = \phi(x_{\min}, y)\exp[-a_2|x_{\min} - x|], \quad x_{\min} \le x \le 0 \tag{2.20b}$$

$$\phi(x,y) = \phi(x, y_{\max})\exp[-a_3|y - y_{\max}|], \quad 0 \le y \le y_{\max} \tag{2.20b}$$

$$\phi(x,y) = \phi(x, y_{\min})\exp[-a_4|y_{\min} - y|], \quad y_{\min} \le y \le 0 \tag{2.20b}$$

Here, a_1, a_2, a_3 and a_4 are attenuation coefficients for exponential field decay. From the above equations, the following relations can be obtained.

$$\phi_{i\max+1,j} \times \phi_{i\max-1,j} = \phi^2_{i\max,j} \tag{2.21a}$$

$$\phi_{i\min+1,j} \times \phi_{i\min-1,j} = \phi^2_{i\min,j} \tag{2.21b}$$

$$\phi_{i,j\max+1} \times \phi_{i,j\max-1} = \phi^2_{i,j\max} \tag{2.21c}$$

$$\phi_{i,j\min+1} \times \phi_{i,j\min-1} = \phi^2_{i,j\min} \tag{2.21d}$$

From the expressions given in Equation 2.21, the relations for the external boundary and the four corner points are obtained and applied to the respective regions of the waveguide.

$$\phi_{x,y\max} = \frac{\phi_{x-1,y\max} + \phi_{x+1,y\max} + R^2\phi_{x,y\max-1}}{2 + 2R^2 + k_0^2 dx^2\{\beta^2 - n^2\} - R^2\dfrac{\phi_{x,y\max}}{\phi_{x,y\max-1}}} \tag{2.22a}$$

$$\phi_{x,y\min} = \frac{\phi_{x-1,y\min} + \phi_{x+1,y\min} + R^2\phi_{x,y\min+1}}{2 + 2R^2 + k_0^2 dx^2\{\beta^2 - n^2\} - R^2\dfrac{\phi_{x,y\min}}{\phi_{x,y\min+1}}} \tag{2.22b}$$

$$\phi_{x\max,y} = \frac{\phi_{x\max-1,y} + R^2\{\phi_{x\max,y+1} + \phi_{x\max,y-1}\}}{2 + 2R^2 + k_0^2 dx^2\{\beta^2 - n^2\} - \dfrac{\phi_{x\max,y}}{\phi_{x\max-1,y}}} \tag{2.22c}$$

$$\phi_{x\min,\,y} = \frac{\phi_{x\min+1,y} + R^2\{\phi_{x\min,\,y+1} + \phi_{x\min,\,y-1}\}}{2 + 2R^2 + k_0^2 dx^2\{\beta^2 - n^2\} - \dfrac{\phi_{x\min,\,y}}{\phi_{x\min+1,y}}} \tag{2.22d}$$

$$\phi_{x\min,\,y\min} = \frac{\phi_{x\min+1,y\min} + R^2\phi_{x\min,\,y\min+1}}{2 + 2R^2 + k_0^2 dx^2\{\beta^2 - n^2\} - \dfrac{\phi_{x\min,\,y\min}}{\phi_{x\min-1,y\min}} - R^2\dfrac{\phi_{x\min,\,y\min}}{\phi_{x\min,\,y\min+1}}} \tag{2.22e}$$

$$\phi_{x\min,\,y\max} = \frac{\phi_{x\min+1,y\max} + R^2\phi_{x\min,\,y\max-1}}{2 + 2R^2 + k_0^2 dx^2\{\beta^2 - n^2\} - \dfrac{\phi_{x\min,\,y\max}}{\phi_{x\min-1,y\max}} - R^2\dfrac{\phi_{x\min,\,y\max}}{\phi_{x\min,\,y\max-1}}} \tag{2.22f}$$

$$\phi_{x\max,\,y\max} = \frac{\phi_{x\max-1,y\max} + R^2\phi_{x\max,\,y\max-1}}{2 + 2R^2 + k_0^2 dx^2\{\beta^2 - n^2\} - \dfrac{\phi_{x\max,\,y\max}}{\phi_{x\max-1,y\max}} - R^2\dfrac{\phi_{x\max,\,y\max}}{\phi_{x\max,\,y\max-1}}} \tag{2.22g}$$

$$\phi_{x\max,\,y\min} = \frac{\phi_{x\max-1,y\min} + R^2\phi_{x\max,\,y\min+1}}{2 + 2R^2 + k_0^2 dx^2\{\beta^2 - n^2\} - \dfrac{\phi_{x\max,\,y\min}}{\phi_{x\max-1,y\min}} - R^2\dfrac{\phi_{x\max,\,y\min}}{\phi_{x\max,\,y\min+1}}} \tag{2.22h}$$

2.3.1.3 Estimation of propagation constant

In order to obtain convergence of the field values, an under-relaxation scheme is applied for convergence of the iterated values. After the under relaxation scheme is applied for iteration, the field value for the subsequent iteration is updated as

$$\phi^{(n+1)} = \phi^{(n)} + f\,(\phi_e - \phi^{(n)}) \tag{2.23}$$

wherein, ϕ_e is the initially assigned field value and f is the under-relaxation factor, which is taken as a constant of value 0.8. The above relations are applied iteratively at each mesh point until the difference in field values in successive iterations $\phi^{(n+1)}$ - $\phi^{(n)}$ is less than 0.025 % of the maximum amplitude of the field. In other words, the required criteria for convergence is given by the relation

$$Max\left\{\frac{\{\phi_{i,j}^{(n+1)}-\phi_{i,j}^{(n)}\}}{\phi_{i,j}^{(n)}}\right\}<0.00025 \tag{2.24}$$

The value of β is calculated every iteration using the relation mentioned by Robertson et al. [97]

$$\beta^2=\frac{\iint(\nabla^2\phi+k_0^2n^2\phi)\phi dxdy}{\iint k_0^2\phi^2 dxdy} \tag{2.25}$$

Both numerator and denominator are discretized and their values are calculated at each point. Forward and backward difference methods are applied according to the position of mesh point in the structure.

Numerator (i,j) = $(\nabla^2\phi_{i,j}+k_0^2n^2\phi_{i,j})\phi_{i,j}\Delta x\Delta y$

Denominator (i,j) = $k_0^2\phi_{i,j}^2.\Delta x.\Delta y$

Numerator and Denominator in the expression for β^2 are as follows

$$Numerator=\iint(\nabla^2\phi+k_0^2n^2\phi)\phi dxdy \tag{2.26a}$$

$$Denominator=\iint k_0^2\phi^2 dxdy$$

(2.26b)

The integrated value over each mesh is given by

$$I_{i,j}=\frac{num_{i,j}+num_{i,j+1}+num_{i+1,j+1}+num_{i+1,j}}{4}.\Delta x.\Delta y \tag{2.27}$$

$I_{i,j}$ is computed for all the elements and arranged together. The points on the corners of external boundary will be used only once during integration as they are connected to only one element. Similarly, other points on the external boundary will be used only twice. So, on simplification, the numerical integration formula for numerator becomes as follows:

$$\begin{aligned}\text{Numerator} = &\frac{\sum num_{i,j}\Delta x_{i,j}.\Delta y_{i,j}}{4} \text{ (for i, j} = \xi) \\ &+ \frac{\sum num_{i,j}\Delta x_{i,j}.\Delta y_{i,j}}{2} \text{ (for i, j} = \eta) \\ &+ \sum num_{i,j}\Delta x_{i,j}.\Delta y_{i,j} \text{ (for i, j} \neq (\xi, \eta))\end{aligned} \tag{2.28}$$

If the point (i, j) is on boundary of two different grid sizes, then the grid spacing is taken as $\Delta x = (\Delta x1 + \Delta x2)/2$ and $\Delta y = (\Delta y1 + \Delta y2)/2$. In a similar way, the denominator given in the integral form in expression 2.26 (b) can be computed numerically. Finally the propagation constant β is calculated as

$$\beta = \sqrt{\left(\frac{numerator}{denomenator}\right)} \tag{2.29}$$

2.3.1.4 Initial conditions

The condition for obtaining the first mode of propagation, as shown in Figure 2.8(a) is $\phi_{\text{mid-1,j}} = \phi_{\text{mid+1,j}}$. where 'mid' is the locus of points forming the line of symmetry along the y-axis and 'j' is the co-ordinate of the grid points along the y-axis. Thus, the first mode condition is derived by equating the slope at the mid point to zero. So, from the condition of field derivative equal to zero at only one location, the first mode of propagation is obtained. The above condition is satisfied by assigning a same initial positive value to all the mesh points. The initial condition for obtaining the second mode is $\phi_{\text{mid,j}} = 0$. All the mesh points in positive region are initially assigned an arbitrary positive value and similarly negative value is assigned to all points in negative region, as shown in Figure 2.8(b). The points on the symmetry line are kept as zero except for two points close to the outer boundary, which are assigned non-zero values, so as to prevent imaginary values of the propagation constants while applying boundary conditions.

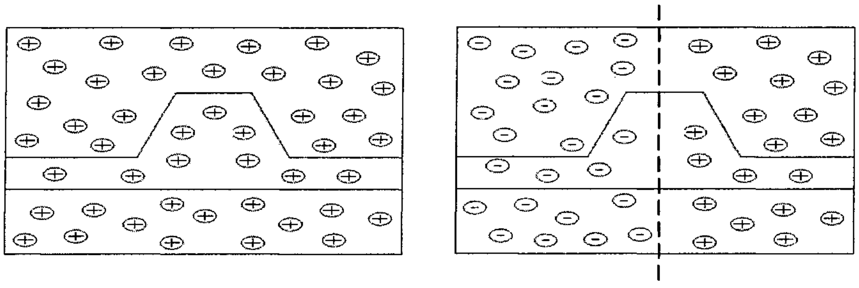

(a) First mode (b) Second mode

Figure 2.8: (a) polarization distribution of initial value in the different waveguide regions for first mode of propagation and (b) for second mode of propagation

2.3.1.5 Flowchart

Figure 2.9 shows the flowchart for finding the value of propagation constant by FD computation.

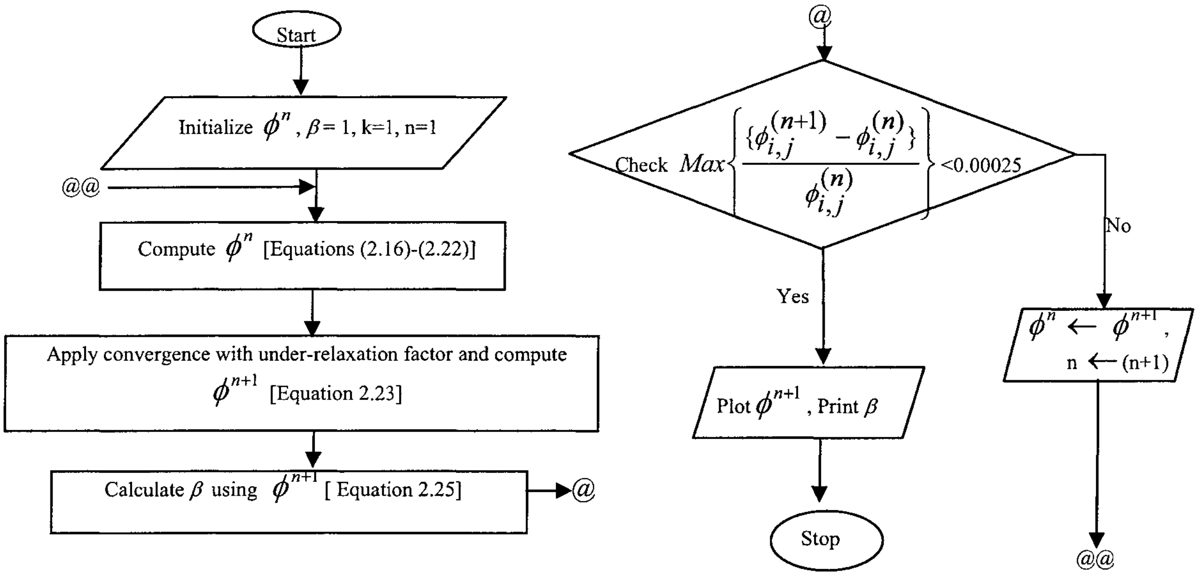

Figure 2.9 : Flowchart for finding the value of propagation constant from the FD computation

2.3.1.6 Results of FD computation

The various geometrical parameters chosen for modeling of SOI based waveguides as modeled with the FD technique is given in Table 2.1. The geometry of the waveguide was selected in order to satisfy the single mode condition for tapered waveguide system [98] is given by the following expression:

$$\frac{W_b}{t} \leq c_{fd} + \frac{\frac{t1}{t}}{\sqrt{(1-(\frac{t1}{t})^2 - \frac{(t-t1)^2}{\sqrt{2}W_b t}}} \qquad (2.30)$$

where W_b is the width of the waveguide base, and c_{fd} is taken as 0.3. As per the relation 2.30, the different parameters considered for modelling are given in Table 2.1.

Table 2.1: Different parameters used for modelling the tapered and straight waveguides using the FD technique.

Type of waveguide	**Parameter**			
	w (μm)	**t (μm)**	**t1(μm)**	**λ (μm)**
Tapered	2	5	4	1.55
Straight	4	4	3	1.55

Figure 2.10 gives the field distribution obtained for the first and the second modes as simulated from the finite difference method for waveguides of different sidewall taper angles. The modes of propagation as simulated for waveguides without sidewall tapers are given in Figure 2.11. It can be seen that the symmetry of the field distribution has been very well predicted by the finite difference method. The values of the propagation constants obtained for different taper angles for the first and second modes of propagation are as listed in Table 2.2.

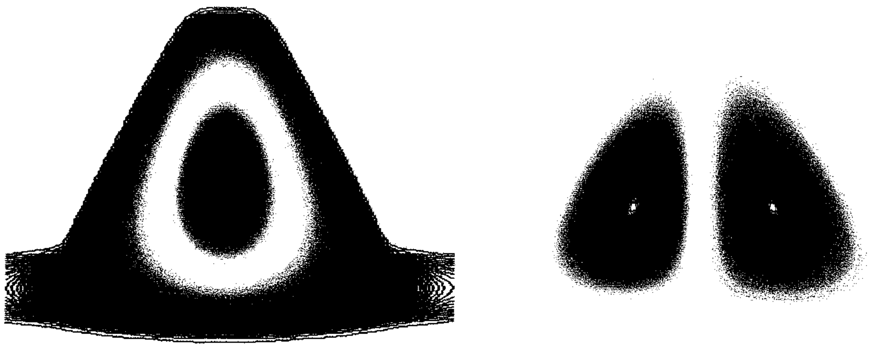

First mode shape ($N_{eff} = 3.4735$) Second mode shape($N_{eff} = 3.4646$)

(a)

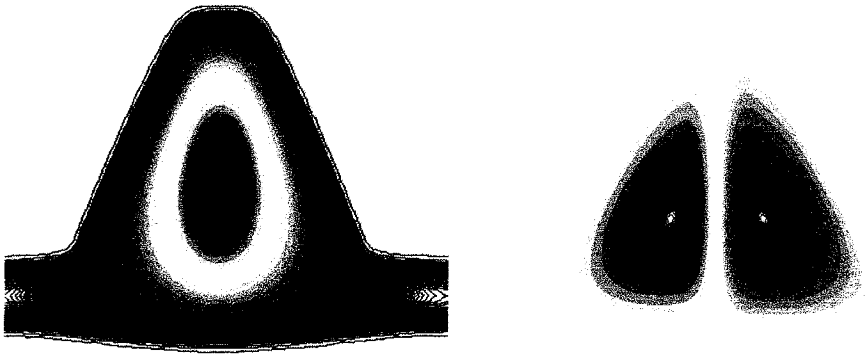

First mode shape ($N_{eff} = 3.4732$) Second mode shape ($N_{eff} = 3.4559$)

(b)

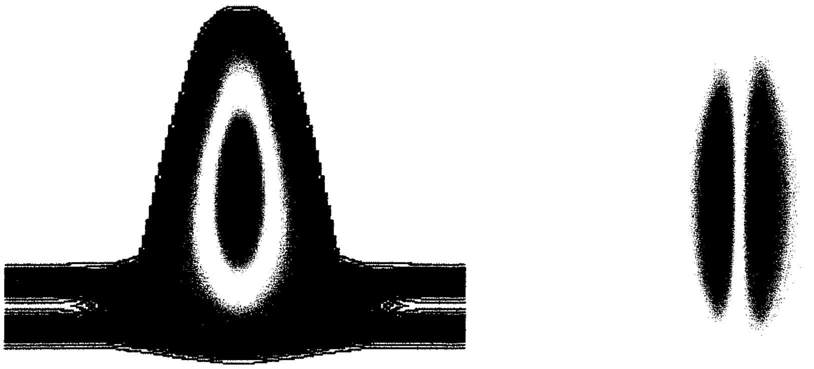

First Mode shape ($N_{eff} = 3.4723$) Second mode shape ($N_{eff} = 3.4157$)

(c)

Figure 2.10: Predicted field distributions for the first and second mode of propagation using FD method for waveguides with sidewall taper angle (a) 35.26° (b) 25° (c) 15°.

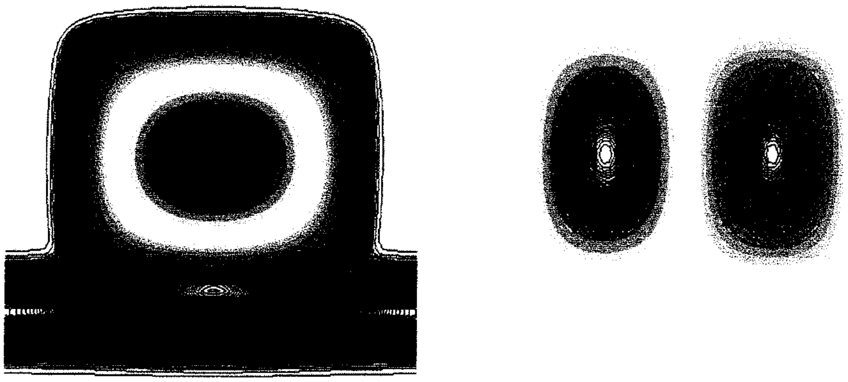

First mode shape ($N_{eff} = 3.4658$) Second mode shape ($N_{eff} = 3.4503$)

Figure 2.11: Predicted field distributions for the first and second mode of propagation using FD method for waveguides without sidewall taper

Table 2.2: Propagation constants for second mode obtained from Finite Difference Method for the first and second modes of propagation

Taper Angle α	Propagation constants	
	I mode	**II mode**
0	3.4658	3.4503
10	3.4706	3.3523
15	3.4723	3.4157
20	3.4729	3.4439
25	3.4732	3.4559
30	3.4734	3.4612
35.26	3.4735	3.4646

All the above results have been obtained taking the covering medium to be air for which the refractive index is one. So, with this method, one can now model an evanescence based sensor through the change in refractive index of the cladding and estimate the resulting influence of evanescence coupling.

2.3.2 Finite Element Method

The Finite Element Method (FEM) is a powerful tool to solve many Partial Differential Equations (PDE) in various disciplines of engineering [99]. The underlying principle of this method is that a complicated domain can be sub-divided into a series of smaller regions, called elements, in which the differential equations are appropriately solved. By assembling the set of equations for each individual element, the behaviour over the entire problem domain is determined.

One of the more outstanding features of the FEM lies on its ability to fit arbitrarily shaped domains by using curved-edge elements [100]. This is a major advantage of the FEM over other computational methods widely used in engineering, like the finite difference method, which only can use rectangular meshes because of the creation of specific nodal points. The other major advantage of the FEM consists in its ability of computing the unknown field everywhere within the computational domain, instead of only at some fixed points.

FEMLAB [93] is a finite element modeling and solver software package for various physics and engineering applications. FEMLAB also offers a smooth interface to MATLAB and its toolboxes for a large variety of preprocessing and post-processing possibilities. The FEMLAB solves Partial Differential Equations (PDE) that describe a model. Herein, the PDE's can be represented in three ways, namely, coefficient form (suitable for linear or nearly linear problems), general form (intended for nonlinear problems), and weak form (that works as a high-level finite element modeling language).

Furthermore, it is possible to set up models as stationary or time-dependent, linear or nonlinear, scalar or multi-component. The package also performs eigen frequency or eigen mode analyses.

2.3.2.1 Computation of solution using FEMLAB

Herein, the FEM for two dimensional waveguide modal analyses has been carried out by solving Maxwell's equation. The generalized Maxwell's equation for wave propagation has been explained in Section 2.2.1. The modal analysis is carried out using FEMLAB in order to compute the effective index of propagation for different modes under different evanescent conditions. Under the *2-D Electromagnetics module,* the required mode is selected, depending on whether the mode analysis is carried out for TE, TM or hybrid waves.

Any FEM problem consists of three basic steps: domain discretization, selection of interpolation functions and computing the solution to the formulated equation. The discretization of domain is one of the most important steps in FEM, because, the manner in which a domain is discretized affects the computation time and the accuracy of the storage results. In FEMLAB, once the structure and the boundary conditions are defined, meshing is automatically generated by the software. However, the meshing parameters such as the maximum element size and the curvature factor can be defined by the user. The modes are then solved for and all the results of the simulation are obtained using the post processing options for analysis.

2.3.2.2 Results

From the FEMLAB analyses, the different mode shapes of wave propagation through the waveguides were obtained and the values of the effective mode indices were used to calculate the birefringence which is computed as the difference between the effective index of propagation under TE and TM fundamental modes. The typically different modes of propagation under TE condition for waveguide for sidewall taper angle of 20° are as shown in Figure 2.12.

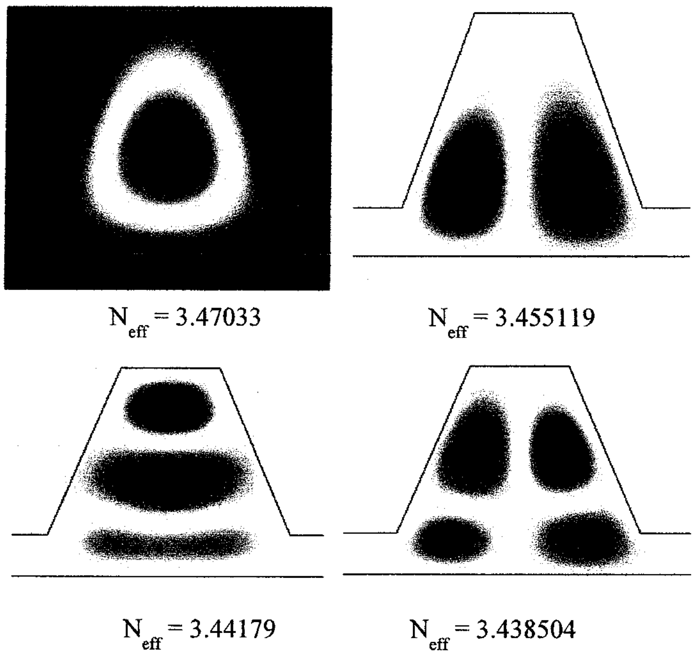

$N_{eff} = 3.47033$ $N_{eff} = 3.455119$

$N_{eff} = 3.44179$ $N_{eff} = 3.438504$

Figure 2.12: Field distributions simulated with FEMLAB for TE waves in waveguides with taper angle 20°

The variation of birefringence for different tapers and with different refractive indices of the covering medium is shown in Figure 2.13. The cladding material considered for birefringence study here is Hydrogen Peroxide (H_2O_2). However, from the literature, there have not been any results on the optical properties of the biological species available in the range of telecommunication wavelength. But for the present work, the refractive index of H_2O_2 is extrapolated from the results available for the refractive indices at different concentrations of hydrogen peroxide for wavelengths in the range of visible light [101]. The refractive index of H_2O_2 for different concentrations at 20 °C of the sample as extrapolated from the data available for visible spectrum is given in Table 2.3.

Table 2.3: Refractive index of H_2O_2 for different concentrations at 20°C for wavelength of light 1550 nm.

H_2O_2 (% conc.)	Refractive index(N)
49.7	1.3315
79.9	1.3412
99	1.3601

The birefringence decreases with increase in the taper angle of the waveguide and increases with the increase in the refractive index of the surrounding medium. The study of birefringence has been restricted to the calculation of the value and no further analysis was carried out using birefringence.

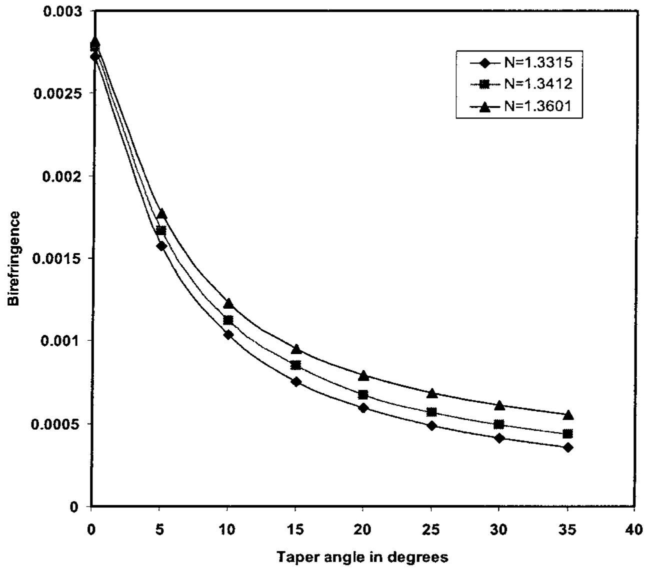

Figure 2.13: Plot of the variation of birefringence with respect to the waveguide taper angle at different refractive indices of the covering medium.

2.3.3 The Beam Propagation Method (BPM)

The Beam Propagation Method (BPM) is a versatile instrument for calculating the wave propagation through optical circuits of different complexities [102]. There have been numerous applications of using the BPM technique for modeling photonic devices like multimode waveguide devices [103], Optical interconnects [104], Photonic crystals [105], Polarization splitters [106] etc. The conceptual simplicity and the flexibility of the method to extend the basic methods to suit other effects of interest like the inclusion of non-linearities and polarizations counts for a few of the several reasons towards the popularity of this technique.

The scalar BPM analysis uses the Helmholtz equation [91] for monochromatic waves, given as

$$\frac{\partial^2\phi}{\partial x^2}+\frac{\partial^2\phi}{\partial y^2}+\frac{\partial^2\phi}{\partial z^2}+k^2(x,y,z)\phi=0 \tag{2.31}$$

Herein, the scalar Electric field $E(x,y,z,t)=\phi(x,y,z)e^{-i\omega t}$ and $k = k_0 n$ where $k_0 = 2\pi/\lambda$. If the variation in ϕ is assumed to be only due to propagation of light in the z-direction and that there is no variation of the refractive index , then the variation would be factored by introducing a slow varying field such that $\phi(x,y,z) = u(x,y,z)e^{i\bar{k}z}$.

In this equation, $\bar{k}$ represents the average phase variation in the field of ϕ and is called as the reference wavenumber. This reference wavenumber can be denoted with a reference refractive index β such that $\bar{k} = k_0 \beta$. Hence the Helmholtz equation now becomes

$$\frac{\partial^2 u}{\partial x^2} + \frac{\partial^2 u}{\partial y^2} + \frac{\partial^2 u}{\partial z^2} + 2i\bar{k}\frac{\partial u}{\partial z} + (k^2 - \bar{k}^2)u = 0 \tag{2.32}$$

Since the variation of u is assumed to be very slow with respect to z, the term $\frac{\partial^2 u}{\partial z^2}$ can be neglected and the equation can be written as $\frac{\partial u}{\partial z} = \frac{i}{2\bar{k}}[\frac{\partial^2 u}{\partial x^2} + \frac{\partial^2 u}{\partial y^2} + (k^2 - \bar{k}^2)u]$. This is the basic BPM equation in 3-dimensions (3D). Simplification of the above equation to 2-dimensions (2D) is obtained by omitting any dependency on y. Given an input field, u(x, y, z=0), the above equation determines the evolution of the field in the space z>0.

The main advantage [91] of the BPM technique is that the second derivative term in z is eliminated which renders the second-order boundary value problem to a first order initial value problem which is obtained by integration of the above equation along the direction of propagation, z. This is significant in the efficiency of BPM technique because of the reduction in time in solving the above equation over z, when compared to the full numerical solution to the Helmholtz equation.

However, there is an inherent problem associated with the elimination of this second derivative along the z- axis because the backward traveling wave solutions are not modeled which could be important for modeling some devices which operate on the principle of reflection. These drawbacks are taken care of by the wide angle and bidirectional approach to BPM. Other factors which have to be taken into consideration are the neglect of polarization effects and simplification of material properties which are otherwise not specific to the BPM approach. But in the present work, the beam propagation is carried out along the straight waveguide and hence the results of the BPM analysis can be assumed to hold good.

2.3.3.1 BPM using R-Soft

Beam propagation for the waveguides was carried out with R-Soft [94] BeamPROP 6.0 module. A method of finite differences is used to solve the scalar wave equations for the tapered rib waveguides. The geometry of the waveguides used for simulation is the same as the structures used for simulation with the FD and FEM techniques. The length of propagation was taken as 500 μm. Since the light input is with a fiber, a separate simulation was carried out for the light propagation through the fiber and the output of the fiber was used as the input field for the anisotropic waveguides.

Figure 2.14 shows the different profiles of R-Soft simulations obtained for a tapered waveguide. The beam propagation simulation results for different waveguide tapers are give in Figure 2.15.

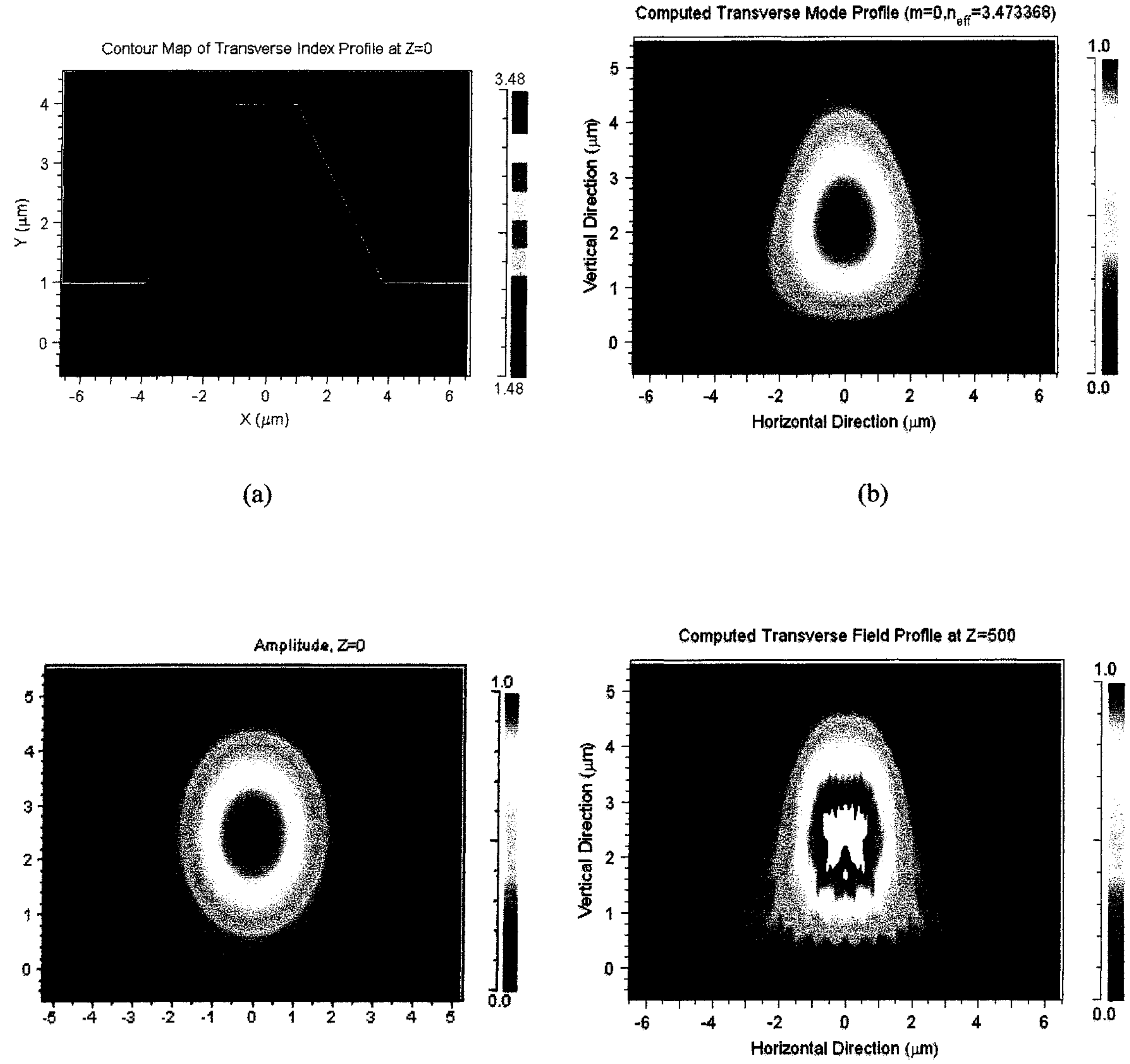

(a)

(b)

(c)

Figure 2.14: (a) Index profile and (b) Mode profile of a waveguide of taper angle 35.26° modeled with R-Soft (c) Input field and the field output simulated with the BPM for 500 μm tapered waveguide

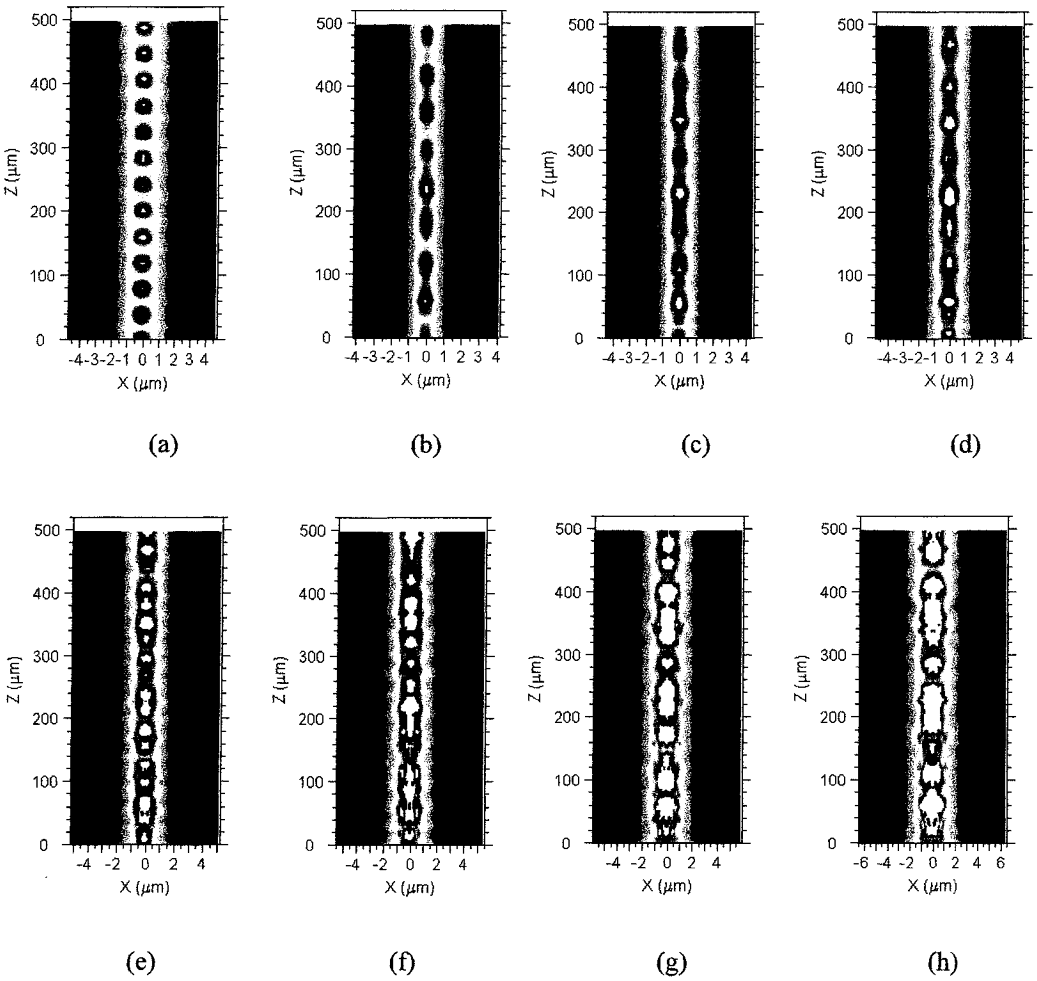

(a) (b) (c) (d)

(e) (f) (g) (h)

Figure 2.15: BPM simulations of waveguides with different taper angles
(a) 0° (b) 5° (c) 10° (d) 15° (e) 20° (f) 25° (g) 30° (h) 35.26°

The effective indices of propagation were computed from R-Soft simulations for different waveguide tapers and were compared with the values obtained from the FD technique and the FEM analysis. Using the BPM technique, the optical power loss due to evanescence could be computed by assigning different monitors along the different optical paths.

2.4 Comparison of results

It is essential to compare the results of a proposed mode solving method with existing and already established methods. The FD technique used in this work to study the modes of propagation in tapered waveguides has been adopted by extending the previous work on straight waveguides by Delage [92] and therefore, in order to authenticate the validity of this method for mode solving, the results of the FD modelling were compared with the standard simulation methods using commercial softwares such as the FEMLAB and the R-Soft. The following tables give the comparison of the effective propagation constant values obtained from the FD, FEM and from R-Soft.

Table 2.4: Propagation constants for first mode obtained from FD Method, FEM and BPM.

Taper Angle α	**Propagation constants for I mode**		
	β_{FD}	β_{FEM}	β_{RS}
0	3.4658	3.4693	3.4700
10	3.4706	3.4674	3.4674
15	3.4723	3.4687	3.4695
20	3.4729	3.4703	3.4709
25	3.4732	3.4714	3.4719
30	3.4734	3.4723	3.4727
35.26	3.4735	3.4734	3.4733

Table 2.5: Propagation constants for second mode obtained from FD Method, FEM and BPM.

Taper Angle α	**Propagation constants for II mode**		
	β_{FD}	β_{FEM}	β_{RS}
0	3.4503	3.4534	3.4551
10	3.3523	3.4401	3.4568
15	3.4157	3.4492	3.4587
20	3.4439	3.4551	3.4601
25	3.4559	3.4592	3.4612
30	3.4612	3.4624	3.4621
35.26	3.4646	3.4648	3.4629

The accuracy of the results depends on different factors, given the different approaches of each of the methods. In FD method, the choice of the grid size plays a huge role in the convergence of the value of effective index because the grid size for the tapered segment of the waveguide was calculated from its geometry. The accuracy of FEM depends upon the meshing and the refinement of the mesh size. The results from R-Soft are also governed by the step size and the grid size of computation. However, the results of the above simulation are more or less equal and the discrepancies arise only due to the meshing and the grid size taken for computation which can be optimized for obtaining more accurate results from the three methods of simulation.

2.5 Study of surface roughness in optical microsystems

It is very important to study the effect of roughness induced from microfabrication procedures in order to characterize the optical performance of the microsystems, so that, one can quantify the allowed roughness suitable for a particular optical environment. An analytical method is applied in order to quantify the impact of roughness on the scattering loss of both waveguide-based and non-waveguide based MOEMS. Herein, two different analytical approaches have been adopted in the estimation of scattering loss. Figure 2.16 shows the scattering phenomenon in the two different kinds of optical microsystem environments.

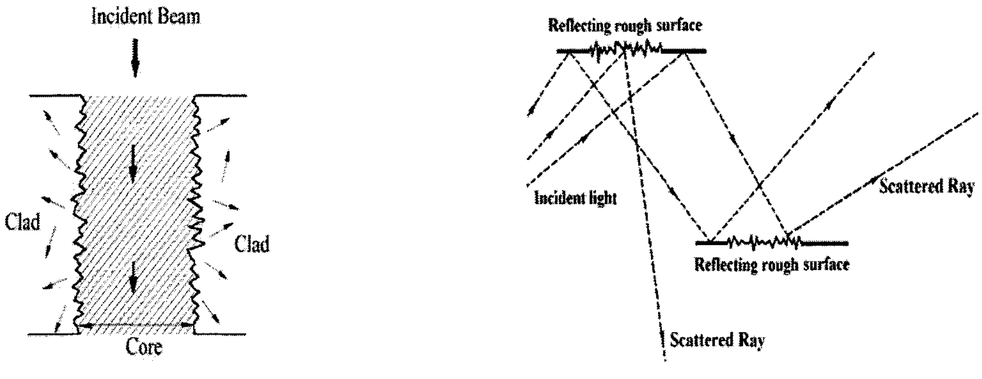

(a) (b)

Figure 2.16: Roughness induced scattering phenomenon in (a) waveguide based and (b) free space and non-waveguide based optical microsystems.

2.5.1 Roughness induced scattering in waveguide based MOEMS

For waveguide based optical microsystems, propagation loss due to roughness induced scattering of the guided wave is considered under the assumption that the loss of light due to material absorption is negligible. The light in a waveguide undergoes a series of total internal reflections before emerging out. The roughness along the sidewalls on the waveguides causes radiative scattering loss of light and random scattering in waveguides disrupts the single mode propagation of the light. In cases where the output intensity of light needs to be sufficient, the loss of light due to scattering leads to very poor sensitivity of the devices, for example the optical micro-gyroscopes in which the waveguides are designed to support two counter rotating guided waves [107] and in the present case, the biosensors that work on evanescent mode principle.

In this approach, the attenuation factor or the scattering loss coefficient α_{sc} for planar waveguides [108] with real roughness function $f(x_s,\gamma)$ on the side walls can be expressed as

$$\alpha_{sc}=\frac{\sigma^2}{k_0 d^4 n_1\sqrt{2}}.g(V).f(x_s,\gamma) \tag{2.33}$$

where

$$g(V)=\frac{U^2V^2}{1+W_s},\ f(x_s,\gamma)=\frac{x_s\{[(1+x_s{}^2)^2+2x_s{}^2\gamma^2]^{1/2}+1-x_s{}^2\}^{1/2}}{[(1+x_s{}^2)^2+2x_s{}^2\gamma^2]^{1/2}},$$

$$U=d\sqrt{n_1^2k_0^2-\beta^2}\ ,\ V\ =\ k_0\,d\sqrt{n_1^2\ -n_2^2}\ ,\ W_s=d\sqrt{\beta^2-n_2^2k_0^2}$$

$$\gamma=\frac{dn_2k_0\sqrt{2}}{W_s},\ x_s=\frac{W_sL_c}{d}$$

Here, σ is the standard deviation of surface roughness variation, n_1 and n_2 are the refractive indices of the core and clad respectively and d is taken as the half-width of the waveguide. The autocorrelation length, L_c, is to be determined from the autocorrelation function that fits the real roughness variation. In general, the exponential type autocorrelation fits the real roughness variation produced by the fabrication and hence the exponential type of autocorrelation as below is assumed for computation. It takes into account the variations in the effective index due to sidewall roughness and it measures the average correlation between one position along the waveguide and another rough position at a distance $\bar{u}$ along the waveguide [109]. The autocorrelation function is assumed as

$$C(\bar{u})=\sigma^2 e^{(\frac{-|\bar{u}|}{L_c})} \tag{2.34}$$

L_c is the autocorrelation length that is to be estimated from the measured roughness variation. The loss of light due to scattering β_{sw} in dB/cm [109] is given by

$$\beta_{sw}=-\alpha_{sw}*10\log_{10}(e) \tag{2.35}$$

2.5.2 Scattering in free space and non-waveguide based systems

Another study involving scattering due to surface roughness is by considering the light reflected off the surface in free space and non-waveguide based systems such as optical micromirrors as shown in Figure 2.16(b). In this method, the estimation of the amount of scattered light from the surfaces for a given value of roughness is estimated by a scattering coefficient [110]. The scattering coefficient is the ratio between the flux of light scattered away from the specular direction to the total reflected flux. The relationship between the scattering coefficient β_{sf} and the rms surface roughness ρ is given by

$$\beta_{sf} = 1 - e^{-\left(\frac{4\pi\rho\cos\theta_i}{\lambda}\right)^2} \tag{2.36}$$

It is essential to study the scattering losses in both the optical microsystem environments in order to study the effect of surface roughness due to hybrid micromachining on both types of optical devices.

2.6 Summary

In this chapter, the modeling of waveguide based biosensor operating on the principle of evanescence was explained. The theory of evanescence due to modified waveguide cladding was studied. The phenomenon of evanescence was further explained through Maxwell's equations. Modeling of the anisotropic waveguides has been carried out using Finite Difference technique, Finite Element Method using FEMLAB and Beam Propagation Method using R-Soft. The results of propagation constants obtained from FD computation were compared with the simulation results of FEMLAB and R-Soft. The results for birefringence calculation using FEMLAB for tapered waveguides with different refractive indices of the cladding and beam propagation simulations with R-Soft were also presented. The influence of surface roughness on scattering loss for waveguide based and non-waveguide based systems was studied.

Chapter 3

Fabrication of SOI Waveguide based MOEMS

3.1 Introduction

In this chapter, the microfabrication feasibilities of the waveguide based biosensor system are discussed. The microfabrications of SOI waveguides have been carried out by two methods, namely, the SOI MicraGeM process technology [15], an industry based technology available through the CMC (Canadian Microelectronics Corporation), and the in-house technique of anisotropic wet etching with TMAH. Herein, the design considerations made for MicraGeM chip fabrication and the post-processing techniques implemented on the MicraGeM loose dies in order to utilize the chips for testing have been detailed. The complete process overview of the anisotropic etching is explained and the fabrication results of both micromachining techniques are presented.

3.2 SOI MicraGeM process technology

MicraGeM is an acronym for Micralyne Generalized MEMS [15]. This technique is a MEMS prototyping process under development at Micralyne Inc. affordably available to the universities through the CMC. Fully suspended MEMS devices with metal electrodes on top rather than silicon can be developed using this technology. MicraGeM differs from traditional MEMS technologies by its variable geometry and the materials used in the process.

3.2.1 MicraGeM design

The MicraGeM process technology allows the design of SOI structures on Pyrex material. It is possible to design an etch in the Pyrex substrate, to form a gap between the SOI and the substrate, and metal electrodes can be designed on both the etched cavity of Pyrex and also on top of the SOI. Thus, through the design regulations, the MicraGeM process technology provides an ideal platform for designing SOI based waveguides with the incorporation of microfluidics to the photonic devices.

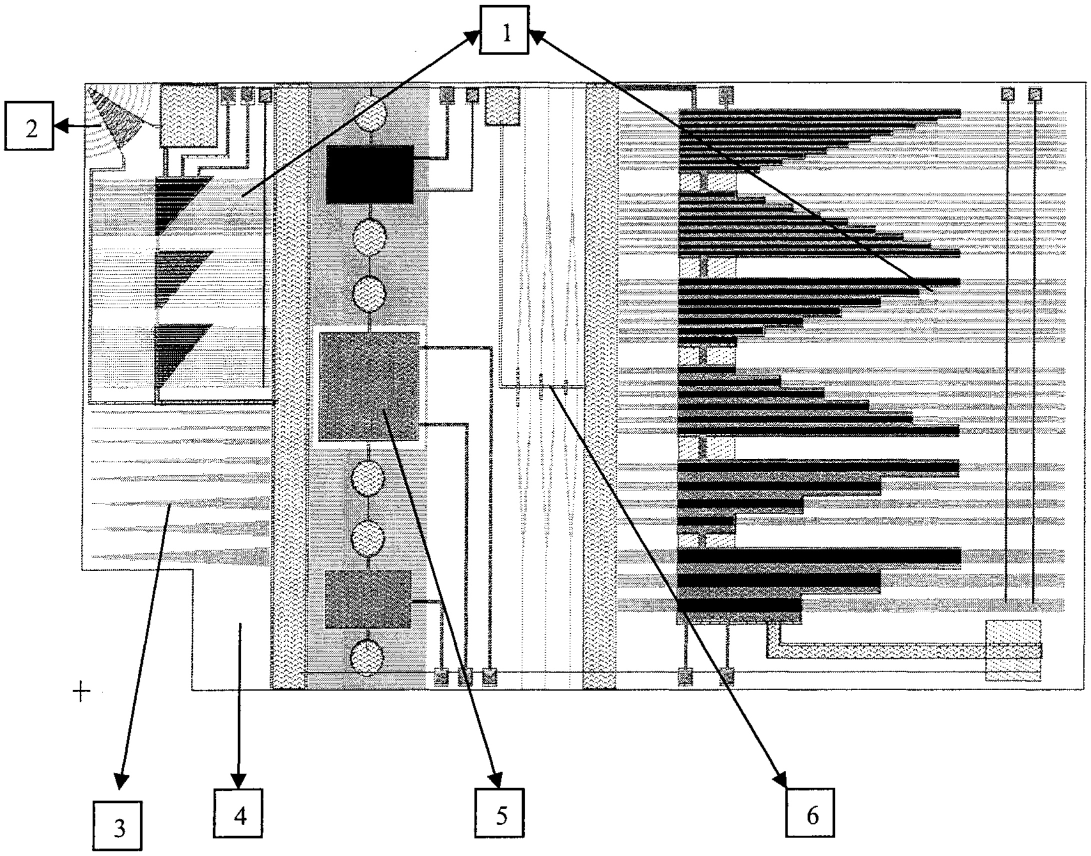

Figure 3.1: The MicraGeM design - 1. Cantilever waveguides 2. Curved waveguides 3. Tapered waveguides 4. Photonic crystals 5. Microfluidic pump 6. Mach-Zehnder Interferometers

The designs were drafted using MEMS Pro v3.1 [111], as shown in Figure 3.1. The different designs submitted to the MicraGeM test run included cantilever type rectangular waveguides of different overhangs, curved waveguides with different radii of curvature, linearly tapering waveguides with the taper ratio varying from 2 to 12, photonic crystals, Mach-Zehnder Interferometers and microfluidic pump. The dimensions of the different structures in the design were based on the design rules laid down in the process technology. The minimum feature size of the Single Crystal Silicon (SCSi) was 2 μm, which was the diameter of the photonic crystals. The specification of the length to width ratio of SOI layer determined the minimal width of the cantilever waveguides as the least wide waveguide was designed to 8 μm width running over a length of 800 μm.

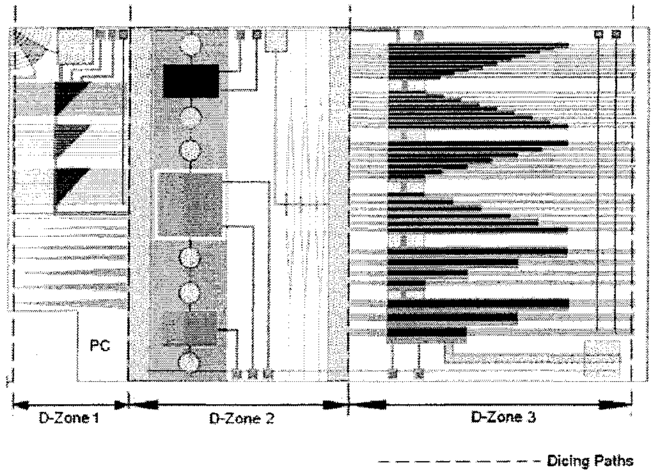

Figure 3.2: Segmentation of the MicraGeM chip design into different D-Zones.

The space available for the design was 9 x 5 mm^2. Thus, the design was planned in such a way that all the devices could be utilized for testing. Most of the designed structures formed waveguides, which meant that these structures should have both the ends of the devices accessible. Hence, clustered MEMS approach was used. Devices with similar purpose were clustered into different zones. The design space was divided into three Design zones or D-zones, namely, D-zone 1, D-Zone 2 and D-Zone 3 as shown in Figure 2.4, such that, the functionality of each of the segments remained independent. Therefore, D-Zone 1 was dedicated to waveguides of widths lesser than 20 mm with different overhangs, circular waveguides, tapered waveguides and photonic crystals. D-Zone 2, which necessitated more working space, was dedicated for microfluidic pump and Mach-Zehnder interferometers and D-Zone 3 was dedicated for waveguides with greater lengths and widths. It can also be seen in Figure 3.2 that the electrical connects and the bond pads for each of the D-Zones remained independent as well. SEM pictures of the different devices fabricated through the MicraGEM process are as shown from Figures 3.3 to 3.8.

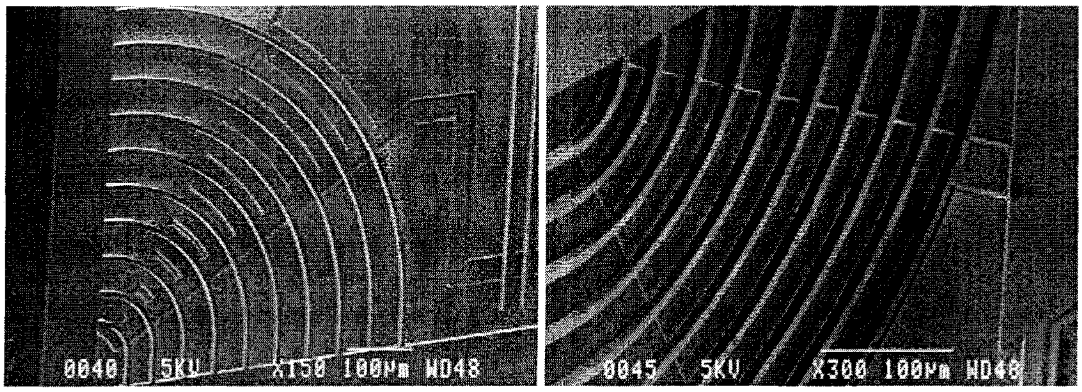

(a) Circular waveguides

(b) Side view of circular waveguides

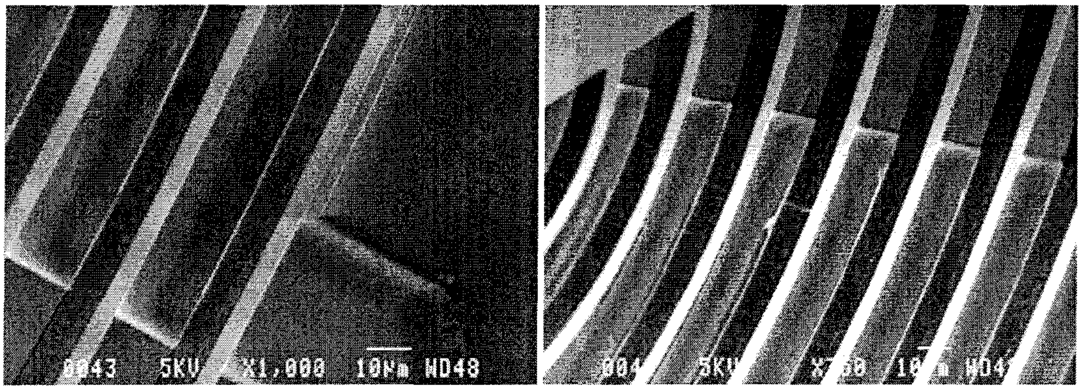

(c) Etched microfluidic channels

(d) Close up of circular waveguides

Figure 3.3: SEM picture of the circular waveguides designed in D-Zone 1 fabricated with MicraGeM process technology

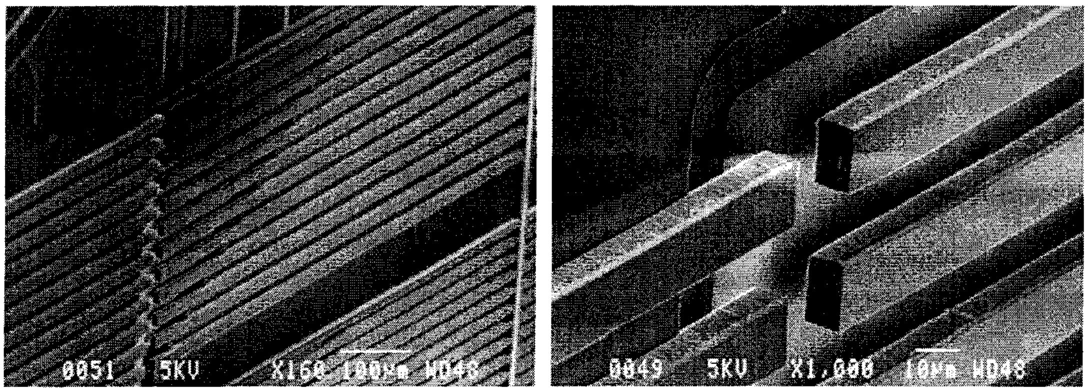

(a)
Arrayed 10 µm wide cantilever waveguides

(b)
Close up of 10 µm wide cantilever waveguides

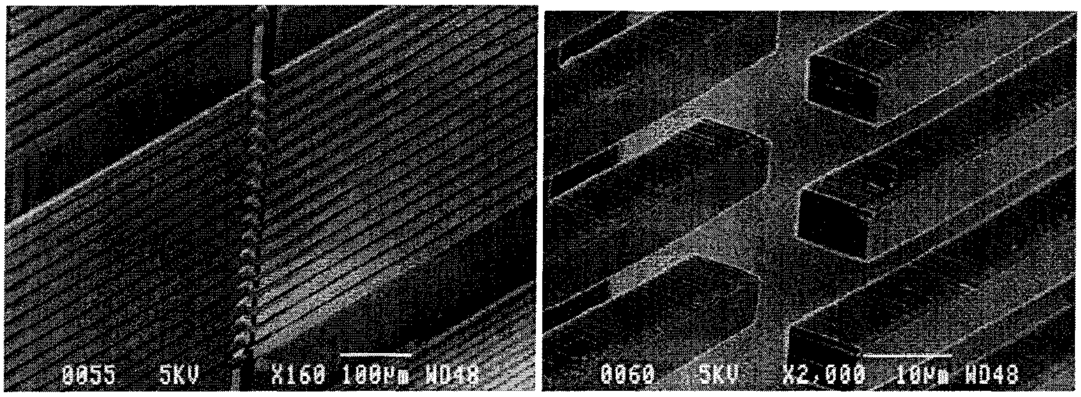

(c)
Arrayed 5 µm wide cantilever waveguides

(d)
5 µm wide cantilever waveguides

Figure 3.4: SEM of the cantilever waveguides (D-Zone 1) of the MicraGeM chip layout

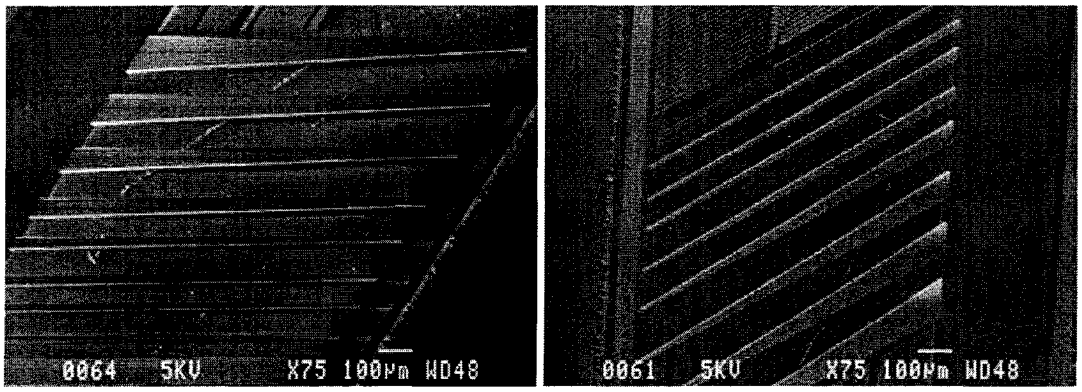

(a) Multimode tapered waveguides

(b) Multimode tapered waveguides

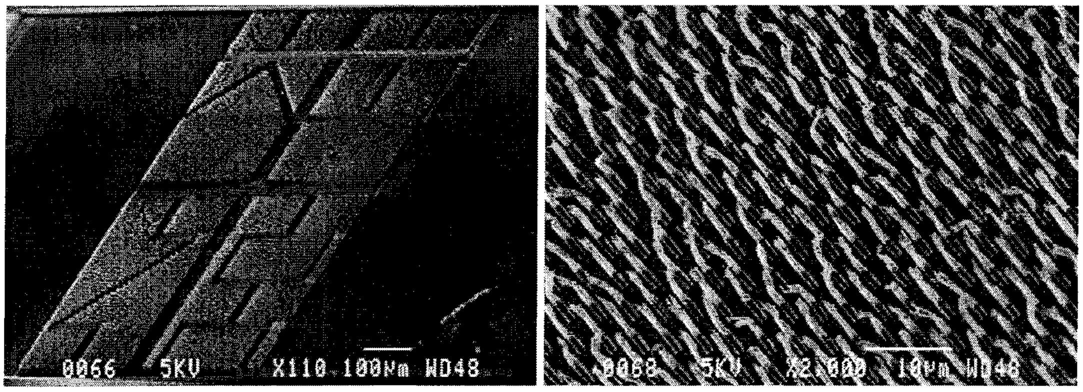

(c) Photonic crystals

(d) Photonic crystals close up

Figure 3.5: (a) SEM of Photonic crystal waveguides designed in D-Zone 1

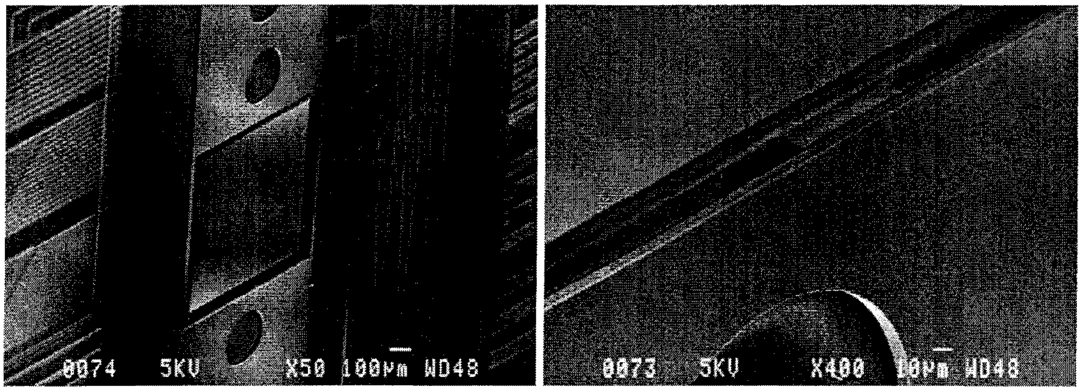

(a) Microfluidic pump cavity (b) Inlet port of the microfluidic channel

Figure 3.6: SEM of the Microfluidic pump designed in D-zone 2 in the MicraGeM chip layout

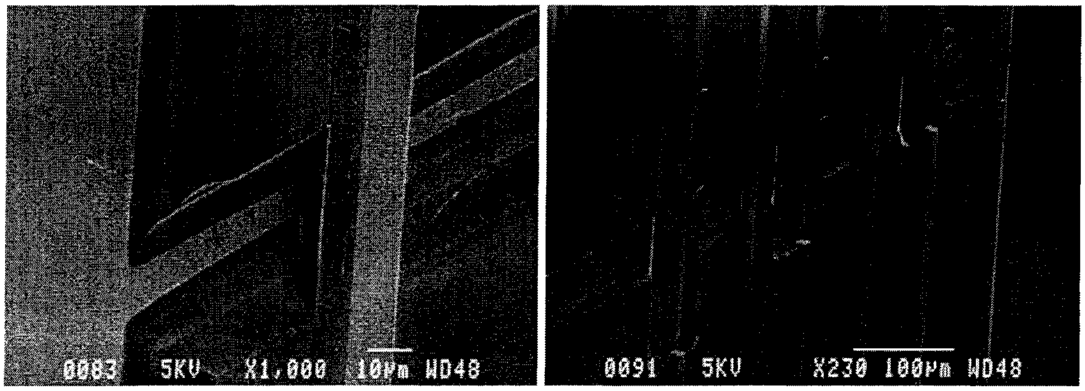

(a) Metal 1 layer on Pyrex etch (b) Mach-Zehnder interferometer

Figure 3.7: SEM of (a) Electrical interconnects (b) Mach-Zehnder Interferometer designed in D-Zone 2.

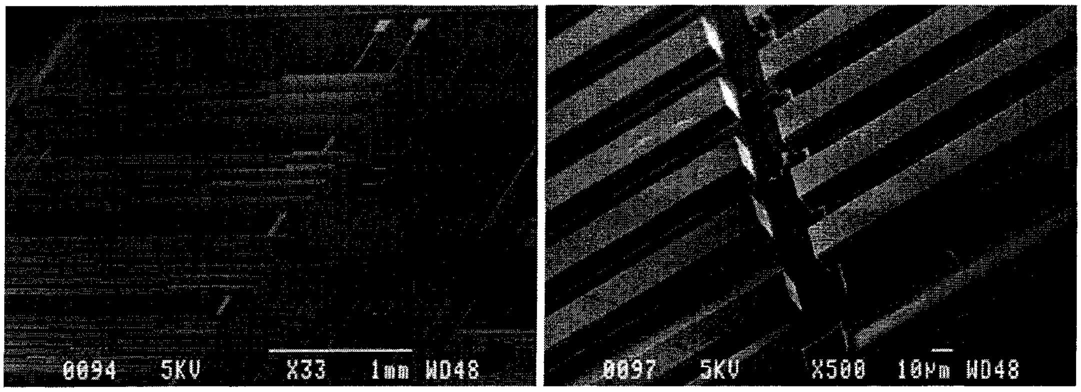

(a) D-Zone 3

(b) 25μm wide cantilever waveguides

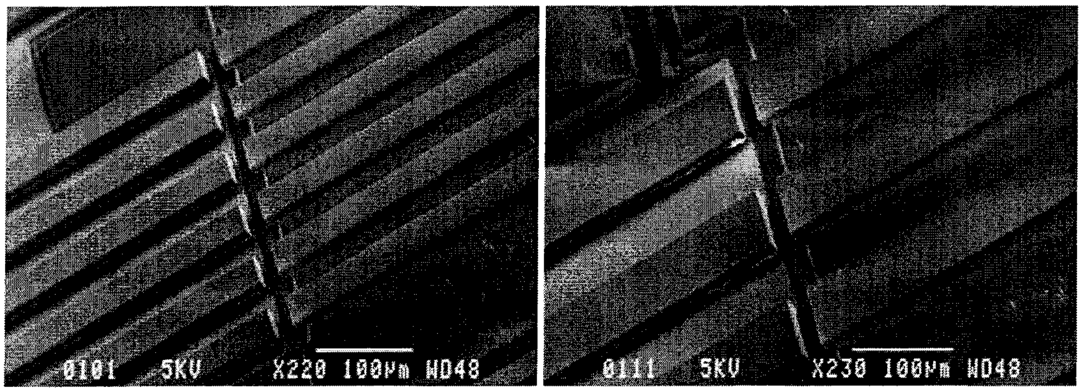

(c) 50 μm wide cantilever waveguides

(d) 100 μm wide cantilever waveguides

Figure: 3.8: SEM of the multimode waveguides designed in D-Zone 3 of the MicraGeM chip layout.

3.2.2 MicraGEM Fabrication results

Though the use of SOI is to obtain a highly smooth surface which would be ideal for optical transmission, there have been certain irregularities in the fabrication and hence an ideal waveguiding surface may not have been obtained. A certain amount of roughness has been identified along the sidewalls in some of the waveguides as a result of which there may be scattering loss of the light traveling through the waveguides. Figure 3.9

shows the rough surfaces formed along the sidewalls of the waveguide due to fabrication imperfections.

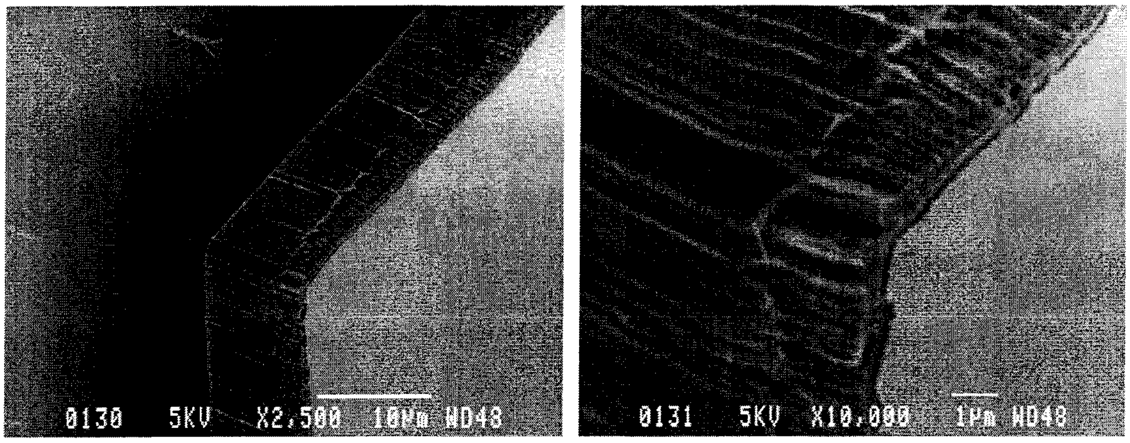

Figure 3.9: Fabrication imperfections in SOI MicraGEM device along the sidewalls of the waveguide.

Apart from the sidewall roughness, the MicraGeM devices are not readily usable for waveguiding applications because the ends of the waveguide devices are not accessible to the input light. The design of the different structures necessarily mean that the different D-zones needed to be separated into individual segments through a cost effective method before carrying out any further analysis. Therefore, a wafer dicing technique with the diamond saw was proposed in order to carry out the post processing operations. Though there are other methods like the high voltage electron beam machining technique which would render smoother machining of the device with better surface finish, those methods are highly energy consuming and lengthy processes. However, it was necessary that the wafer dicing process does not destroy the functionality of any of the sections of the device. Therefore, an optimized post processing wafer dicing method was carried out in order to divide the wafers into different segments

3.2.3 Wafer dicing

The wafer dicing operation was carried out in the Nanofab laboratory at the McGill University, Montreal, Canada. The set up for the wafer dicing post processing operation consisted of a vacuum chuck and a dicing saw with joysticks controlling the lateral and the rotational alignment of the saw with respect to the sample. The position of the blade with respect to the wafer was viewed through a camera and the fine adjustments were carried out whenever necessary. Due to the smaller size of the device, handling was also a major problem during the post processing operations. A single side adhesive tape of around 70 μm thickness was placed on the chuck and held firm onto it vacuum. The sample is then placed on the tape and is aligned accurately with respect to the blade position. There was a problem over the sufficiency for the adhesion of the tape. But since dicing had to be carried out near the edges of the wafer as well, a double-sided stronger adhesive tape was used so as to hold the sample firmly onto the chuck thereby preventing wobbling of any sort during the machining. Considering the fragility of the device, it was highly important to mount and remove the device with extreme care. It was also essential that the operation be carried out without the coolant because the influx of the coolant could cause severe damage to the dynamic structures on the sample. The wafer dicing operation was carried out under the following specifications:

Depth of dicing: 700 μm.

Thickness of the dicing blade: 5 mil.

Rotational speed of the blade: 16000 RPM.

Feed rate: 2 mm/sec.

Figure 3.10 shows the SEM pictures of the diced wafers. It can be observed that some of the devices were damaged, as shown in Figure 3.11, due to distorted machining caused by over heating of the blade during the process. Since the coolant was not used in this operation, the dust collected from the machining process was also accumulated and hence the device needed to be cleaned with Isopropyl Alcohol (IPA) and Acetone. The rough surfaces of the waveguide ends were polished before carrying out further testing and post processing with the device.

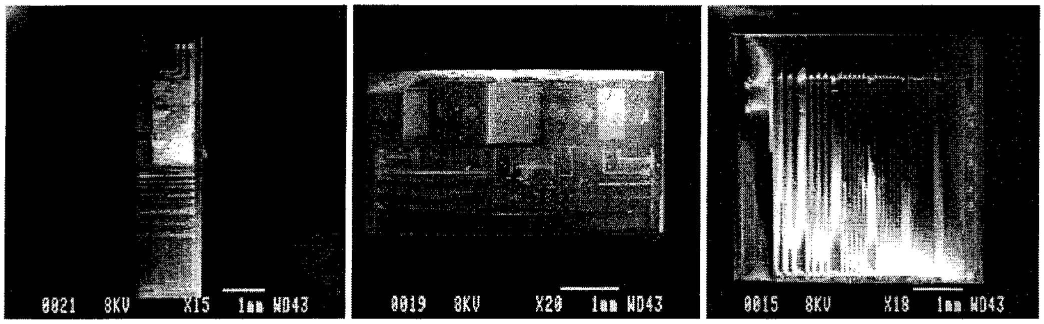

(a) D-Zone 1 (b) D-Zone 2 (c) D-Zone 3

Figure 3.10: SEM pictures of the MicraGEM devices after dicing with diamond saw (a) D-Zone 1 (b) D-Zone 2 and (c) D-Zone 3

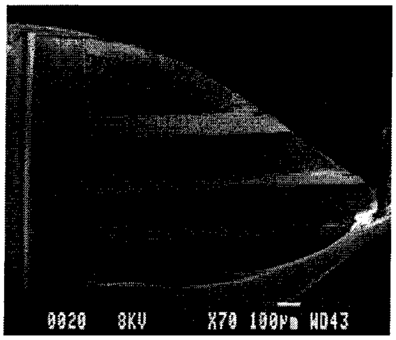

Figure 3.11: SEM picture of a broken segment of D-Zone 1 as a result of over heating of the blade during the dicing operation resulting in a distorted machining.

3.3 Anisotropic etching with Tetra Methyl Ammonium Hydroxide

Anisotropic chemical etching on Silicon have been used for the fabrication of various 3D microstructures for micro-optics , microelectronics and micromechanical systems, such as, sensors, actuators, diaphragms, microfluidic channels, cantilevers etc. [112]. There have been many etchants like Potassium Hydroxide (KOH), Ethylenediamine Pyrocatechol (EDP) and Hydrazine, which have been used for etching Silicon. However, the use of TMAH has gained popularity for silicon etching because of its non-toxicity, non-flammability, etch selectivity and hence its compatibility with the CMOS technology [113]. Though KOH has been widely used for anisotropic etching, the fact that it etches the oxide layer as well prevents the usage of KOH and renders TMAH as the ideal choice for the present application. A brief introduction to the anisotropic etching methods using TMAH was detailed in Chapter 1. In this chapter, the complete microfabrication procedure using TMAH will be discussed ab initio.

Unlike isotropic etching, the anisotropic etching of silicon depends on various factors of the microfabrication process, which must be taken into consideration when designing the silicon based waveguides. Primarily, the etching of silicon with TMAH depends upon the orientation of the crystallographic planes. The commercially available SOI wafers are <100>, <110> and <111>.

Before going into the details of anisotropic etching, it would be useful to introduce a couple of etch design, namely, deviation angle and the inclination angle. The deviation angle is the angle made by the mask opening with respect to the wafer flat and inclination angle is the angle made by the slope formed during the anisotropic etching, with respect to the vertical. Figure 3.12 shows the different etch rates and the under-etch rates of Silicon with respect to the deviation angle and the inclination angle for anisotropic etching on <100> wafers [114]. It is thus known that the maximum inclination angle for the anisotropically etched waveguides is 35.26°.

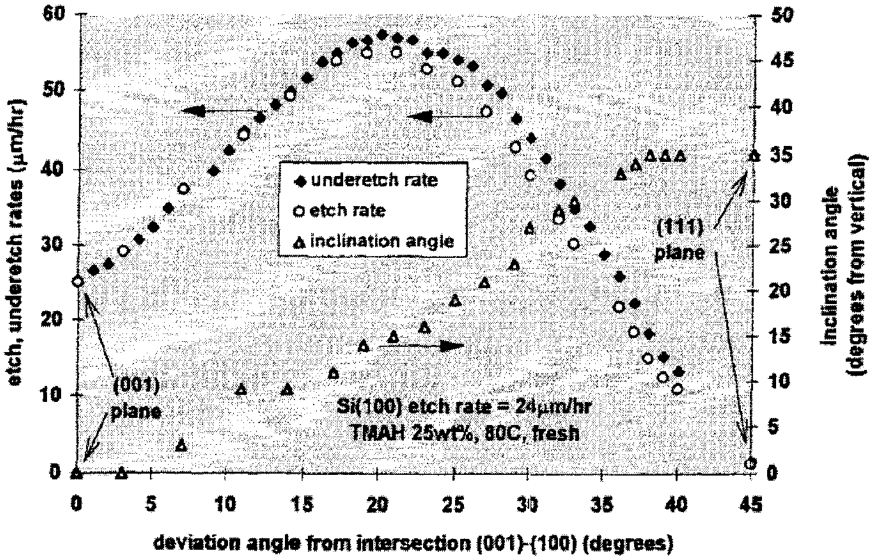

Figure 3.12: Variation of the etch rates and the under-etch rates for <100> Si wafer when etched with TMAH [114]

For the anisotropic waveguides fabricated with TMAH etching any variation in the taper angle for the rib waveguides is between 0 and 35.26. The different tapers on the waveguide are achieved by changing the angle of the mask orientation with respect to the wafer flat of {100} plane of the wafer during photolithography. The masking with respect to the wafer flat is as shown in Figure 3.13. Here, α_m is the angle made by the mask with respect to the wafer flat. When this angle is varied between 0 and 45 with respect to the wafer flat, different inclination angles of etching are obtained. The etching is stopped by the slow etching <111> planes which form an angle of 35.26° with respect to the <100> plane when α_m = 0 or 90°.

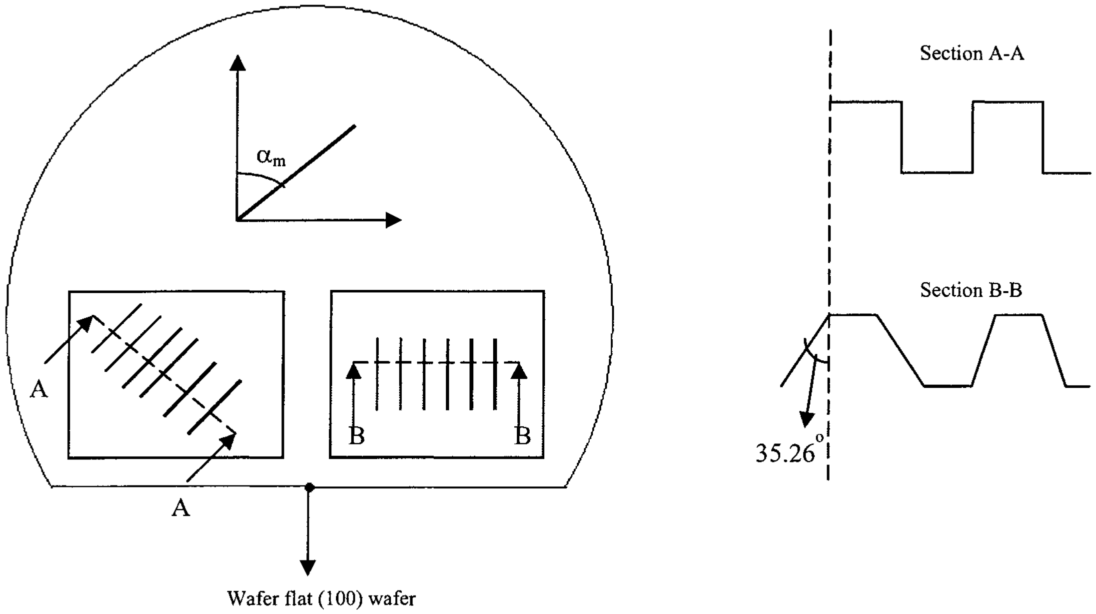

Figure 3.13: Mask aligning with respect to the wafer flat for different tapers of the waveguide.

Thus, the maximum angle of taper of the waveguide which can be obtained through the TMAH anisotropic etching process on <100> wafer is 35.26°. For section A-A, when the mask is at an angle of 45° with respect to the wafer flat, the subsequent etching results in vertical walls of the waveguides. For section B-B, wherein the mask orientation with respect to the wafer flat is 0°, the etched waveguides have a sidewall taper angle of 35.26°. Thus, the etch rates and the under-etch rates of the etchant along the different crystallographic planes of the substrate determine the shape of the structure during the subsequent anisotropic etching.

Apart from the crystallographic parameters of the microstructure, another factor which governs the design drafts is the etching at the waveguide corners. When the anisotropic etching solution attacks the fast etch corners, the corners are etched as shown in Figure 2.7. The fast etch planes form an angle of 22.5^{o} with respect to the (100) and (110) intersection and the etch rate is 55 μm /hr along the fast etch planes.

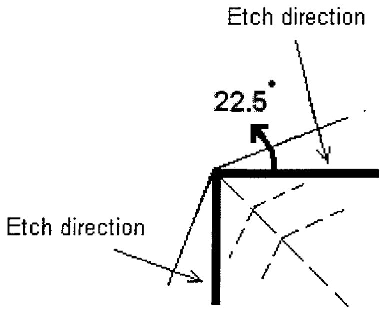

Figure 3.14: Etching of the corners in anisotropic etching process.

The etching of waveguide corners not only affects the length of the waveguide, yet another geometric parameter to be taken into consideration for beam propagation and waveguide design, but also it leads to the requirement of further post-processing techniques like the end polishing and wafer dicing.

3.3.1 Mask design

Every step in the microfabrication is very important for the accuracy of the end product. The first step to microfabrication involves the generation of patterns suited to particular applications, which are intended to be transferred onto the substrate. This calls for the preparation of the photo masks in accordance with the geometry and the dimensions of the required microstructure.

Thus, for the present work, the masks were made after carefully studying the various anisotropic parameters as described. The initially prepared masks, shown in Figure 3.15 (a), were designed in order to study and characterize the etching and the under-etching rates of TMAH, before the masks for the intended microstructure waveguide designs were drafted.

The mask designs for the waveguide structure are as shown in the Figure 3.15 (b). The minimum feature size of the waveguide structure is 2 μm, after taking into consideration the limitation in the conversion of the AutoCAD drawing into the postscript format before the pattern transfer onto the thin film through photolithography.

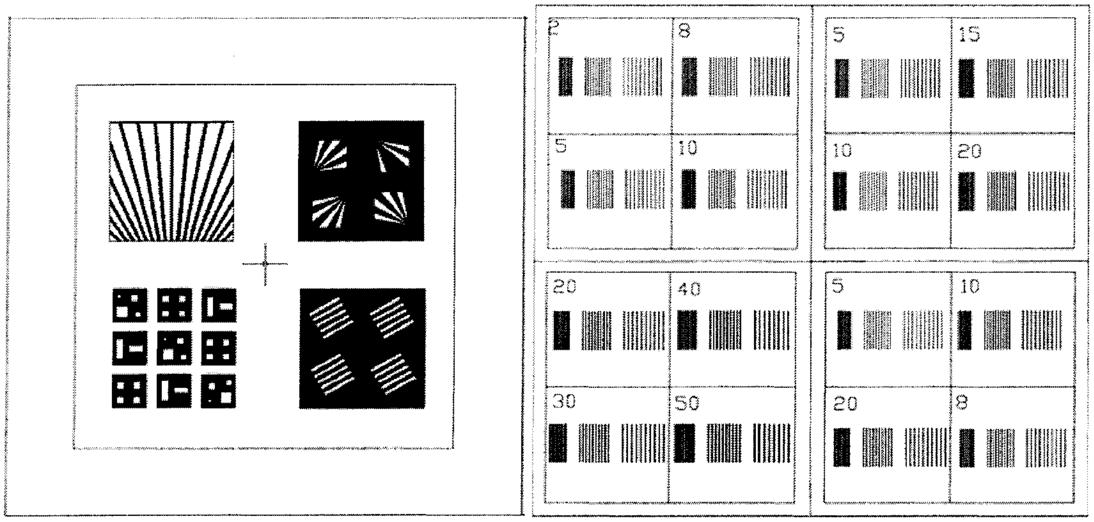

(a) (b)

Figure 3.15: (a) Sample masks prepared to characterize the etching and under-etching rates of TMAH (b) Mask design for anisotropic waveguides.

3.3.2 Process flow

The process flow for the microfabrication process is shown in Figure 3.15. Oxidized Silicon wafers are coated with the photoresist and upon selective exposure to UV and subsequent developing, the required portions of photoresist are removed. Thereafter, the oxide layer is removed from the developed areas and etched with TMAH.

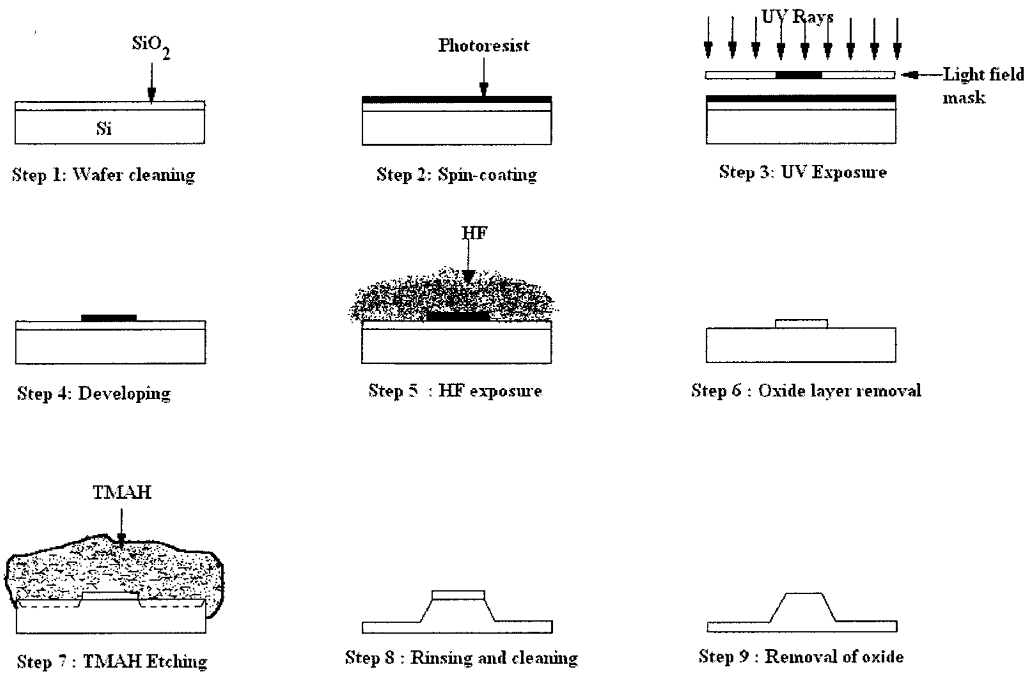

Figure 3.16: Microfabrication process flow

3.3.2.1 Wafer Oxidation

The first step towards the beginning of waveguide fabrication on SOI wafers by anisotropic etching is wafer oxidation. Since the commercially available SOI wafers were not oxidized, it was necessary that the wafer is oxidized in order to carry out the subsequent anisotropic etching on the wafers. The wafer oxidation process was carried out at the Micro-fabrication laboratory at the Ecole Polytechnique, Montreal. The SOI wafers (Ultrasil Corp., USA), were initially cleaned carefully with Acetone and Isopropyl Alcohol so as to prevent any deposition of dust on it. The thickness of the different layers of the SOI wafer were as follows: Device layer 5 μm, the oxide layer 1 μm and the handle layer 500 μm. It was then rinsed with deionized water and the moisture was removed. The procedure for wafer oxidation is described below.

The oxidation process is a three stage process which involved dry oxidation, followed by wet oxidation at 1100 °C and then dry oxidation again. The furnace was initially purged with Nitrogen gas at 2 psi. The furnace is then switched on and the temperature was allowed to increase. The wafers are then loaded on a quartz boat and introduced into the furnace. It was important that the wafers were introduced slowly into the furnace so as to avoid the development of thermal stress in them. At around 500 °C, the nitrogen flux was closed and oxygen flux at 1 psi was introduced, thus initiating the dry oxidation process.

A solution of Hydrochloric Acid and DI water in the volumetric ratio of 1:20 was heated to around 80 °C. When the temperature of the furnace reached around 1000 °C, the oxygen flux to the furnace was removed and was purged into the HCl- H_2O solution, such that the vapors of the solution were fluxed into the furnace. This process is known as the wet oxidation. It is essential to use the solution of HCl and water so as to accelerate the oxidation process. The amount of HCl - water solution was monitored so as to prevent excess evaporation. After 3 hours of wet oxidation, the dry oxidation process was started again by unplugging the oxygen flux from the solution and re-introducing it directly into the furnace. After 30 minutes of dry oxidation, the oxygen was shut and the nitrogen gas at 2 psi was allowed to purge the furnace. The quartz boat was slowly removed at the rate of approximately 5 cm for every minute in order to keep the wafers away from thermal stress introduced by sudden change in temperature. Under the above mentioned conditions, a thickness of about 513 nm of oxide thickness was obtained.

3.3.2.2 Photolithography

Photolithography is the process of transferring the designed patterns from the photomasks onto the silicon wafer. In this process, the wafers are exposed to UV rays through the mask after the photoresist is coated. Photoresist is a chemical which coagulates upon exposure to light except at the wavelength of yellow light. When exposed to UV rays and rinsed with a photoresist developer, the photoresist can be removed only in the exposed regions. There are two kinds of photoresists which are available, the positive and the negative photoresists. The difference between the two kinds of photoresists lies in the fact that when exposed to UV rays and subsequently the developer, the positive photoresist is removed only in the exposed regions whereas the non exposed regions are removed with the negative photoresist. This principle is illustrated schematically in Figure 3.17.

The mask types which are generally used for photolithography process are photographic emulsion on soda lime glass (cheapest), Ferrous Oxide (Fe_2O_3) on soda lime glass, Chromium on soda lime glass, Chromium on quartz glass. But these masks are expensive and are used with deep UV lithography.

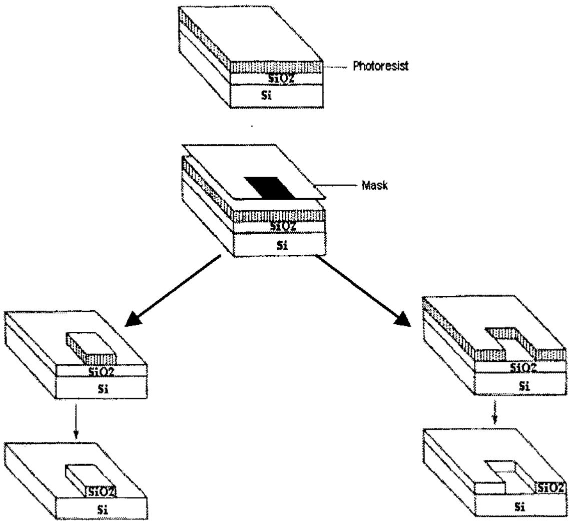

With positive photoresist With negative photoresist

Figure 3.17: Lithography results using positive and negative photoresists [115]

Herein, light field masks were used in this process, where the opaque portion on the thin film forms the structure retained on the wafer after subsequent photolithography and etching. The photomasks were prepared with a resolution of 5080 dpi at Centre Typo [116], Montreal and Typo Express [117], Montreal. Chrome-glass mask was prepared with a resolution of as high as 40600 dpi at Fine-line Imaging, Colorado [118] for high resolution and reduced feature size.

The photolithography with S1818 photoresist and the process description is as given below:

1. The wafer was cleaned initially by introducing the chip firstly into Acetone, held with a pair of metal tweezers, and then rinsed in distilled water. It is extremely important to avoid contact of Acetone with any forms of plastic.

2. After the chip was manually dried off moisture, it was placed on the hot plate and pre-baked for 45 seconds. The temperature on the hotplate is set to 90° C.
3. The chip was then placed inside the spin-coater (WS-400, Laurell Technologies). After proper alignment, the vacuum is switched on so that the wafer holds its position during the process. The photoresist (Shipley Microposit S1818 positive photoresist) was introduced on to the wafer from the top using the dropper and the wafer was spin coated with the photoresist in two cycles, for 5 seconds at 500 rpm and immediately for 45 seconds at 3500 rpm respectively. The thickness of the photoresist obtained under these conditions is in the order of 2 ~ 4 μm.
4. After spin coating, the wafer was soft baked by placing it on the hot plate for 30 seconds at the same temperature scale.
5. The wafer was then aligned properly with respect to the mask design in the UV illuminator. The mask design has been made such that the mask would be appropriately aligned on the frame. This frame should be rigid on to the UV setup and should not be disturbed once the mask is aligned so that the UV rays are well directed through the mask onto the photoresist.
6. The illuminator was switched on and after lamp power reaches 300W, the shutter is opened and the UV rays are exposed onto the silicon wafers for 90 seconds.
7. After the UV exposure, the wafer is taken out and introduced in the developer solution. The patterns can now be seen on the wafer and it is then rinsed again with distilled water. In case the patterns are not clearly seen on the wafer, the procedure is repeated again by first removing the photoresist off the wafer using

the remover solution and repeating the above mentioned steps till a clear pattern is visible on the wafer.

8. The wafer is then post baked for 120 seconds by placing it on the hot plate at the same temperature, so as to remove the excess moisture present and improve the adhesion between the photoresist and the wafer surface.

The photolithography operations were also carried out at the Nanofab laboratories, McGill University. In the lithographic setup used there, S1813 photoresist was used. The lithographic parameters are listed in Table 3.1.

Table 3.1 : Photolithography parameters followed at Nanofab laboratory, McGill University.

Operation	**Specifications**
Pre-baking	100 °C for 60 s
Spin Coating	3900 rpm , 90 s
Soft baking	115 °C , 90s
UV exposure	Lamp power 165 mJ/cm^2 , 4 s
Developing and rinsing	120 s
Post baking	100 °C , 900 s (with oven)

A sample of an oxidized silicon wafer after photolithography is shown in the Figure 3.18.

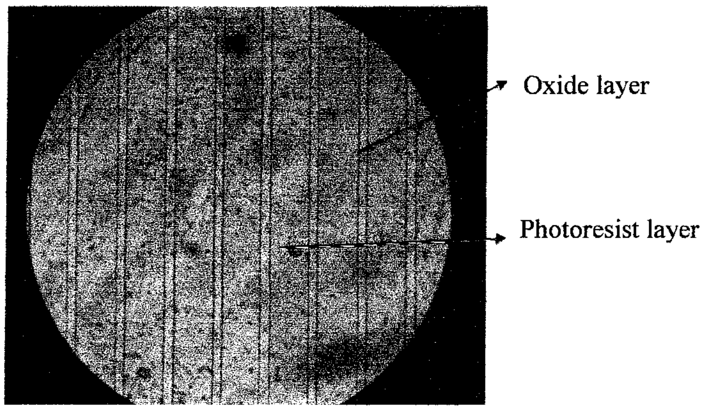

Figure 3.18: View of a sample after photolithography before oxide layer removal under the microscope.

3.3.2.3 Removal of oxide layer

It is essential that the oxide layer be removed so as to enable TMAH attack on the areas exposed after photolithography. 48 % Hydrofluoric acid is mixed with deionized water in the ratio 1:4 HF to H_2O. The wafer is introduced into the solution for 13 minutes and then rinsed in DI water. The characterization of the HF: H_2O concentration was done after sets of repeated trials for different acid-exposure times. Now, the layer of oxide removed in this process is only in the regions where the photoresist was developed, as shown in the process flow diagram.

3.3.2.4 Anisotropic wet etching

After the oxide layer is removed, the wafers were then etched anisotropically with TMAH. The TMAH etch setup is as shown in Figure 3.19.

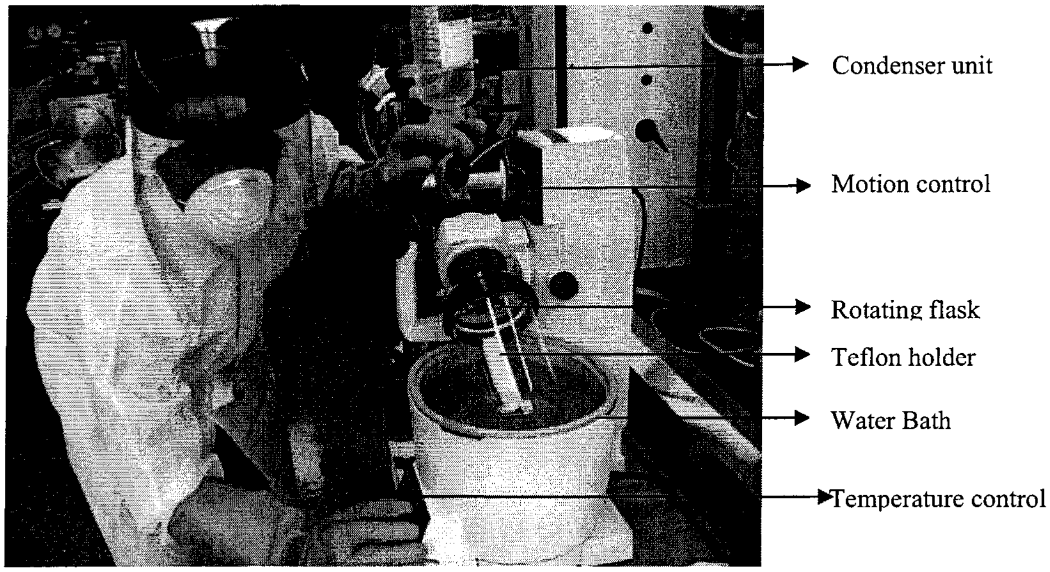

Figure 3.19: TMAH etch setup.

The setup consists of a rotating flask with RPM controller unit, a water-bath with temperature controller and TMAH re-circulating unit. 25% TMAH solution is filled in the rotating flask. The water bath is filled with de-ionized water and is heated till the temperature reaches around 85 °C. The wafers were aligned on a Teflon holder and are introduced into the TMAH. The flask was then immersed partially into the water bath and the etchant is allowed to reach a temperature of 80 °C. The characterization of the etchant temperature and the water-bath temperature is previously carried out and the time taken by the etchant to reach 80 °C when the temperature of the water bath is 92°C is 5 minutes. The flask was rotated, once the temperature is reached as a mild agitation is required for the etchant to continuously etch the silicon. The time of etching was calculated and etch rate was estimated using the etch depth and etch time.

Since the setup is a closed circuit, the TMAH which evaporates is condensed and circulated back so that it can be reused in order to maintain the concentration of the bath. The etched silicon is deposited at the bottom of the flask itself and hence, the etch rate of TMAH decreases when the concentration of silicon increases. The TMAH is then replaced or the deposited silicon is filtered and the TMAH is used again. The etch rate under the above prevalent conditions was found to be 22.5 μm/hr.

3.3.3 Fabrication results

Figure 3.20 shows the SEM pictures of some of the structures etched with TMAH as a part of characterization process for estimating the etch rates and the under etch rates of the etchant under the prevalent conditions.

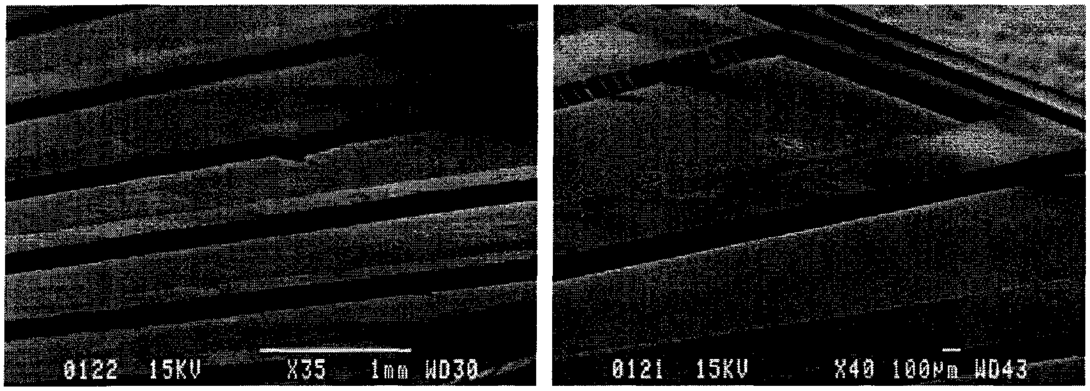

(a) Anisotropic slabs

(b) Anisotropic slabs

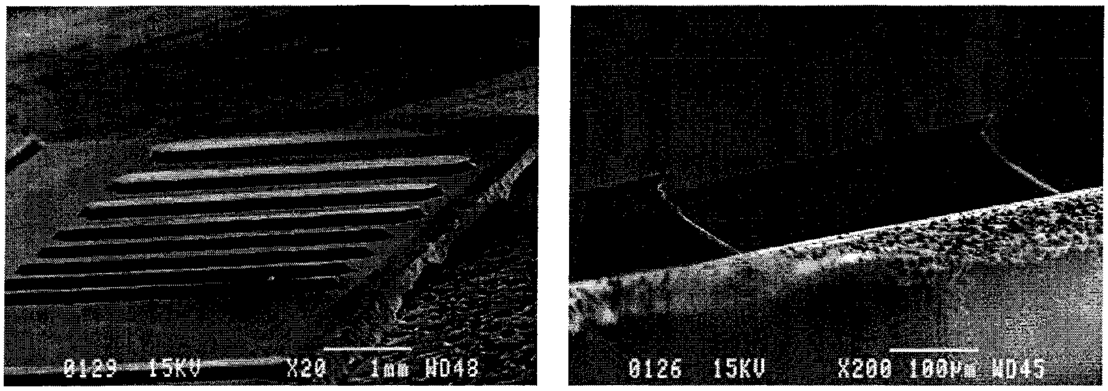

(c) Fast-etched corners

(d) Under-etched samples

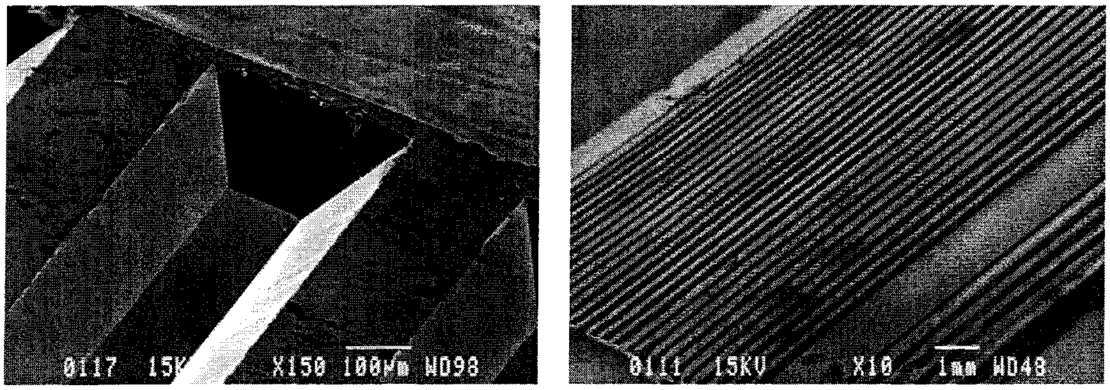

(e) V-Trench

(f) V-grooves

Figure 3.20: SEM of some of the structures microfabricated using anisotropic etching with TMAH

The SEM pictures of the etched waveguide samples are given in Figure 3.21. The maximum etch depth that could be obtained was the thickness of the device layer of the SOI wafer which was 5 μm. But, it was essential that the complete etching of the device layer be avoided so as to create the wings of the rib waveguide. Therefore, the samples were etched for a very short time of 15 minutes. The Teflon holder containing the samples was removed quickly after the rotary flask was stopped, so that the silicon etching at lower temperatures could also be prevented.

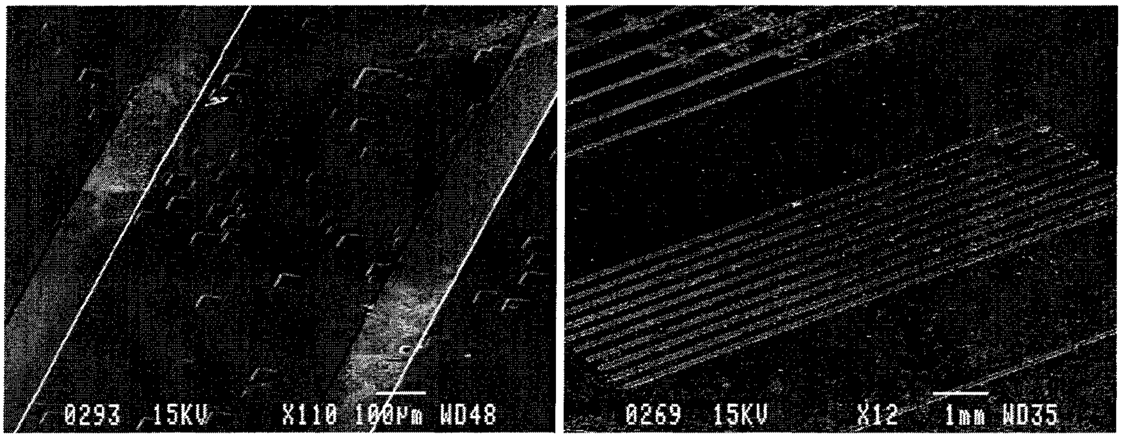

(a) Anisotropic waveguides

(b) Anisotropic waveguide

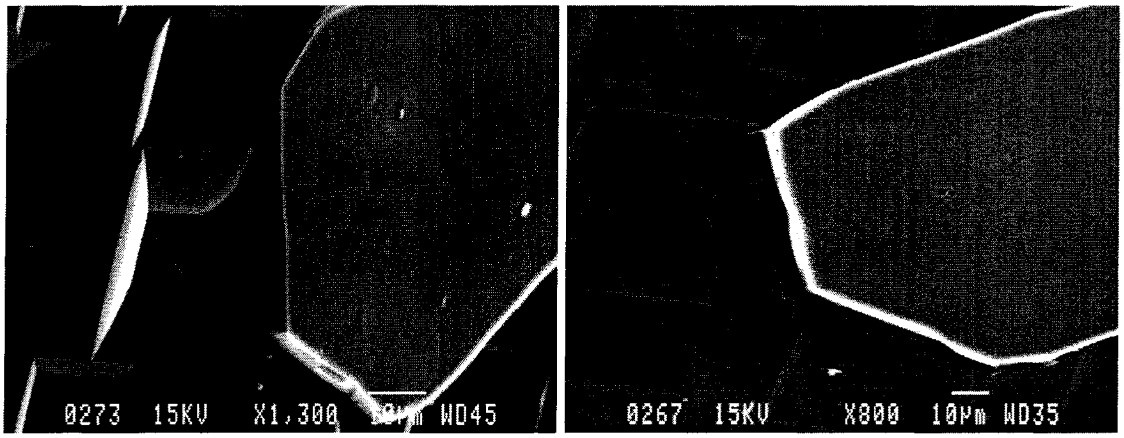

(c) Waveguide corners before dicing

(d) Fast etch corner before dicing

Figure 3.21: SEM pictures of some of the etched waveguides before dicing the fast etch corners

The minimum width of the rib waveguide obtained was 20 μm. As seen in the figures 3.21 (c) and (d), the fast etch corners were formed during the etching and hence, these corners had to be removed in order to use the etched structures for waveguiding. Therefore, the corners were diced using diamond saw dicing technique at McGill university. The feed rate was 2 mm/s at a cutting speed of 16000 rpm. Coolant was used in order to prevent over heating of the blade. The SEM pictures of the SOI waveguides after dicing are shown in Figure 3.22. The formation of the tapered walls of the waveguides can be seen in Figure 3.23 (a) and (b).

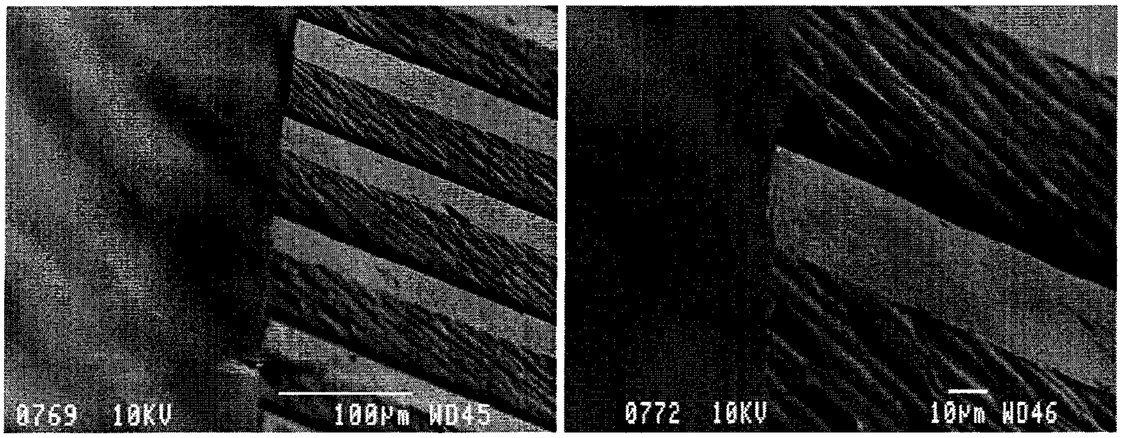

(a) Rectangular rib waveguides width 20 μm

(b) Diced corner of rectangular waveguide

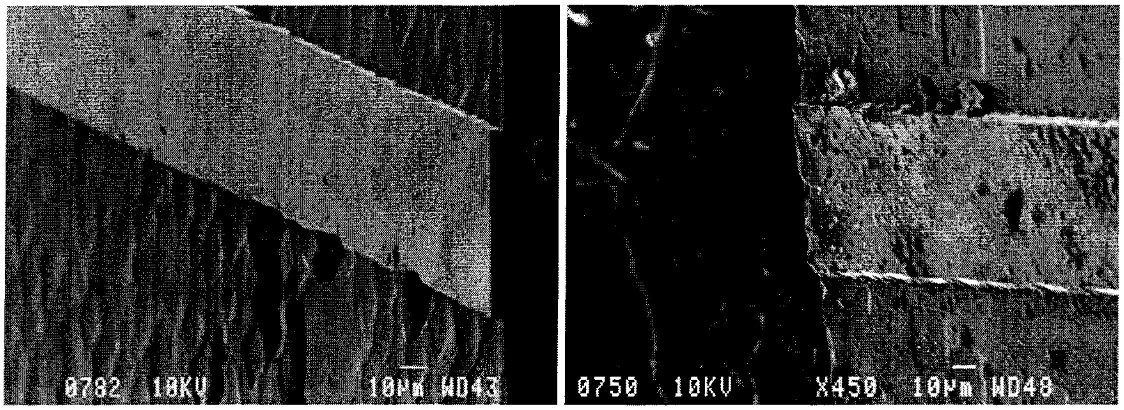

(c) Rectangular rib waveguide, width 50 μm

(d) oxide layer removal

Figure 3.22: SEM pictures of TMAH etched rectangular waveguides before oxide layer removal.

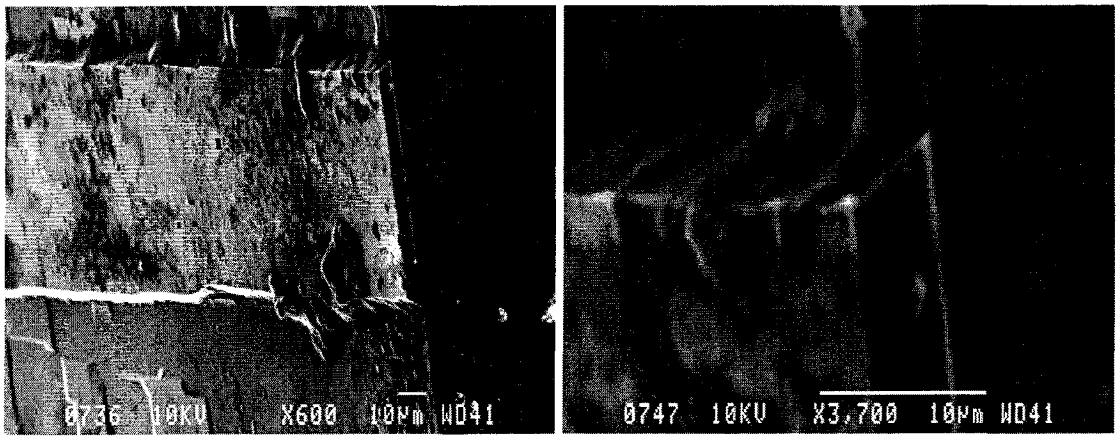

(a) Anisotropic waveguide (before oxide removal)

(b) Diced corner of anisotropic waveguide

Figure 3.23: SEM pictures of tapered waveguide structures after dicing and before oxide layer removal

There are some important factors which have affected the microfabrication process as seen from the SEM pictures. Firstly, the patterns on the photomasks which were used for photolithography were transferred from thin film onto a glass mask for performing the photolithography at McGill Nanofab laboratories. Consequently, due to resolution differences, the lines formed on the glass masks were not devoid of ridges, which have been subsequently transferred on to the substrate during the etching. This has resulted in the sidewall roughness and unevenness. Low dimensions could not be obtained with thin film masks. However, when photolithography was carried out with fine resolution glass masks, the patterns were washed off soon during the oxide removal using HF. This could have possibly been the problem with post-baking or the concentration of the oxide etchant. There have been certain irregularities in the fabrication which are mainly due to lithographic imperfections, as shown in Figure 3.24(a), and non-uniform oxide layer removal thereby resulting in uneven etching of the surface as shown in Figure 3.24(b).

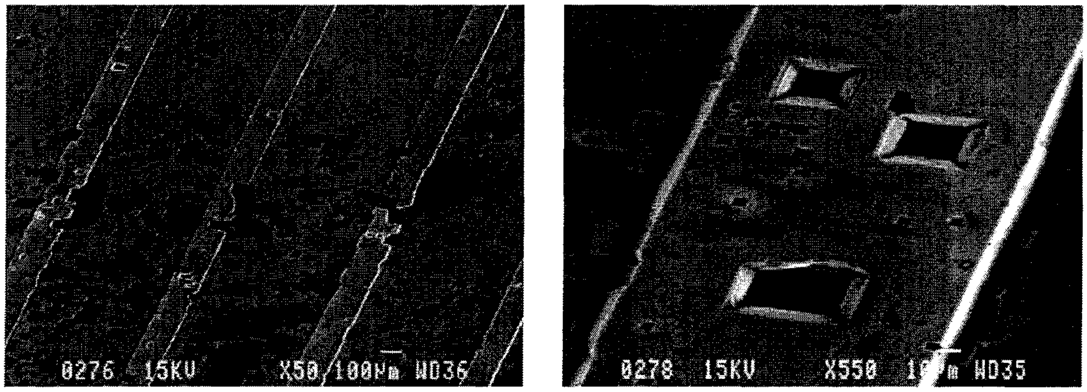

(a) Improper oxide etching (b) Non-uniform oxide etching

Figure 3.24: SEM pictures of fabrication irregularities due to lithographic imperfections and non-uniform oxide layer removal.

The SOI samples were then dipped in 48 % concentrated HF for 1 second to remove the oxide layer on top and were used for biophotonic testing.

3.4 Summary

In this chapter, the fabrication feasibilities of waveguide based SOI devices through SOI MicraGeM process technology and anisotropic micromachining with TMAH. The design of clustered MEMS devices with the MicraGeM process was explained along with the strategic wafer dicing technique employed as post-processing method for MicraGeM devices. The detailed process flow for anisotropic micromachining was explained along and the fabrication results of both MicraGeM process and TMAH etching were presented.

Chapter 4

Hybrid Micromachining Technique

4.1 Introduction

In the previous chapter, the feasibilities of microfabrication of waveguide based biosensors through the SOI MicraGeM technology and also the anisotropic etching with TMAH were discussed. But, the application of these two technologies are limited especially for fabricating cost effective non-straight or tapered waveguides. However, this limitation can be overcome with isotropic fabrication technique with XeF_2, through which unconstrained geometry of micromachining is realised, as seen in Figure 1.6. But apparently, there exists a problem with surface roughness in XeF_2 micromachined devices. This problem is not good and cannot be overlooked for optical microsystem devices, as surface roughness could cause a lot of optical scattering and propagation losses. Thus, the problem of surface roughness phenomenon renders the micromachining techniques such as isotropic gas phase etching, DRIE etc. ineffective for the fabrication of optical MEMS devices.

Hence, in order to overcome the problem of surface roughness identified during bulk micromachining processes, a hybrid micromachining technique is proposed for the microfabrication of both the kind of optical microsystems, namely, the waveguide based and non-waveguide based devices. This method consists of carefully combining the bulk microfabrication process along with controlled anisotropic wet etching to reduce the surface roughness. The purpose of anisotropic etching is to smoothen the rough surface of the etched sample utilizing the selectivity property of anisotropic etchant for different crystallographic planes. It is important to carry out the anisotropic etching at controlled temperature with appropriate etchant concentration as surface roughness of the etched sample is affected by the concentration of the etchant and also the temperature of anisotropic etching operation [119]. In the present work, in order to demonstrate the feasibility of the proposed hybrid micromachining process, Tetra Methyl Ammonium Hydroxide (TMAH) has been used as the wet anisotropic etchant. The procedure of hybrid micromachining technique which includes dry isotropic etching combined with controlled anisotropic wet etching to improve surface roughness is described below.

4.2 Hybrid Micromachining process

As mentioned before, the hybrid micromachining technique involves controlled wet anisotropic etching over previously etched rough surface. Herein, to demonstrate the feasibility of hybrid micromachining process, silicon samples were etched isotropically with XeF_2 and anisotropic etching was carried out on those samples. Isotropic etching with XeF_2 was already discussed briefly in Chapter 1 and the schematic of the XeF_2 setup is as shown in Figure 1.5. The procedure of isotropic etching with XeF_2 [120] for each pulse is discussed below:

1. The samples were loaded into the etch chamber, after the supply and the purge valves were closed the chamber was pumped down to vacuum of around 1 mTorr.

2. At this pressure, the supply valve was opened so as to sublimate the white XeF_2 crystals and fill up the chamber. The supply valve was closed when the pressure inside the chamber reached 2 Torr.

3. Under these conditions, the etching of silicon was carried out with the XeF_2 gas inside the chamber for a duration of approximately 60 seconds. After that time, the purge valve was opened to fill the chamber with Nitrogen gas at a pressure of 5 psig.

5. The gas mixture in the chamber was pumped back to 1 mTorr to begin the next pulse of etching. This procedure was repeated for the required number of pulses. The surface roughness increased with increased pulses of etching.

In order to demonstrate the improvement of surface roughness with anisotropic etching, silicon wafers previously etched with XeF_2 for 13 pulses were introduced in TMAH. After isotropic etching, the samples were initially dipped in 48% Hydrofluoric acid for 3 seconds in order to remove any native oxide that could have been present on the surface after the previous etching, and were rinsed with deionized water. The cleaning of the silicon surface is very important prior to TMAH etching not only for oxide removal but also to prevent the saturation of silicon surfaces with other chemicals and impurities of metals which have higher reduction potential than silicon [121]. In this regard, an addition of HCl to HF could reduce pitting and surface roughening [122].

The etch setup for TMAH was an open system placed under the fume hood wherein TMAH is heated to the required temperature in a water bath. It is preferential to use a closed etch system for TMAH etching in which the etchant is circulated back into the apparatus. However, it must be taken into consideration that in the present work, the time of etching with TMAH was very less, and therefore sample handling was a problem when etching was carried out under the closed system. The samples are aligned in a specially machined Teflon holder and were introduced into undoped 25% TMAH solution at 80^0 C. The solution was mildly agitated manually during the etching process. Under such conditions, the etch rate with TMAH was estimated to be 20.2 µm/hr. The samples were etched for different time counts of 5, 10, 20, 30, 60, 90, 120, 180, 240 and 300 seconds. After etching, the samples were rinsed with deionized water in order to remove any traces of TMAH before further analysis.

4.3 Results of hybrid micromachining

The roughness of the sample after etching for a definite time period were determined and characterized by Atomic Force Microscopy (AFM) and Scanning Electron Microscopy (SEM) methods. Figures 4.1 to 4.9 show the SEM and the AFM micrographs for the etched samples with progressive hybrid micromachining.

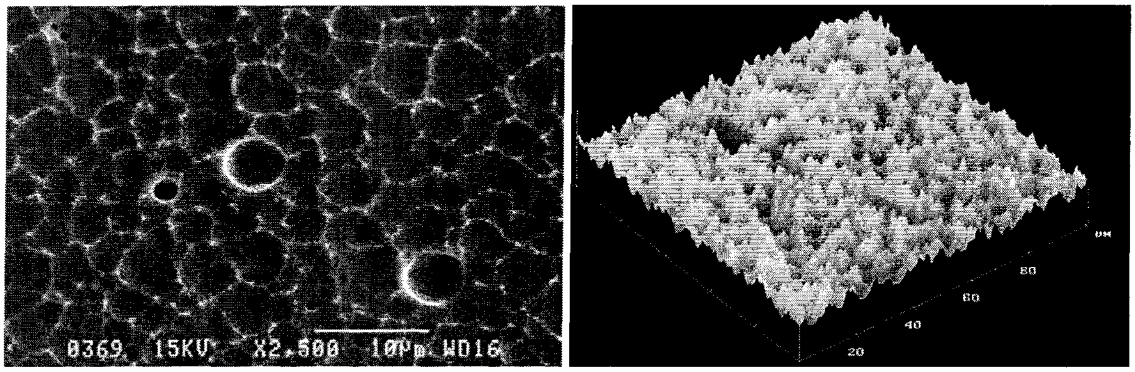

(a) (b)

Figure 4.1: (a) SEM and (b) AFM micrograph of the sample after etching with XeF_2 for 13 pulses and before etching with TMAH.

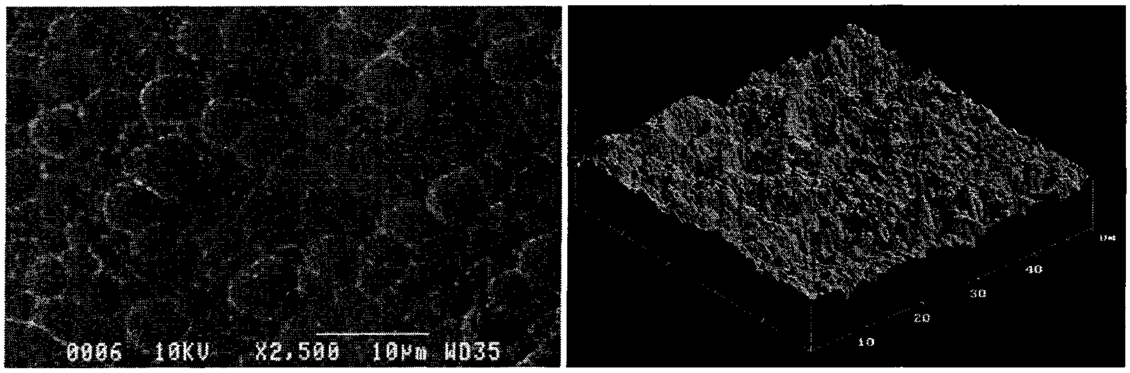

(a) (b)

Figure 4.2: (a) SEM and (b) AFM micrograph of the sample after etching with TMAH for 5 seconds.

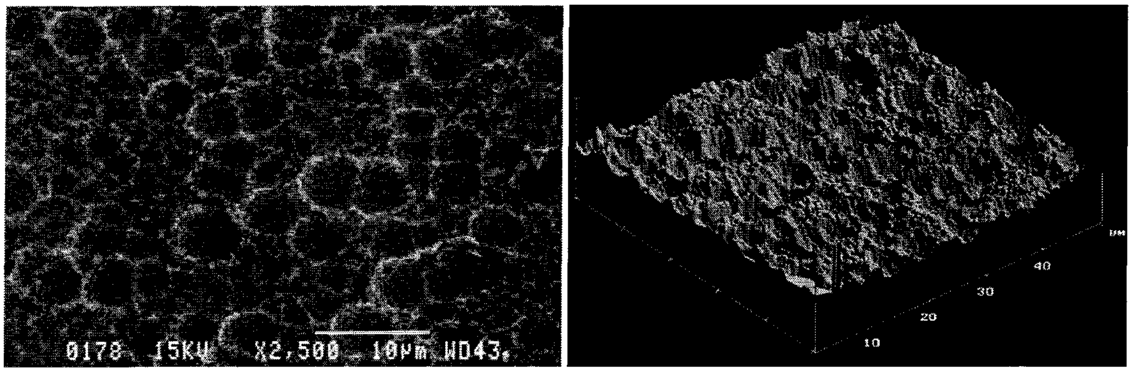

(a) (b)

Figure 4.3 (a) SEM and (b) AFM micrograph of the sample after etching with TMAH for 10 seconds.

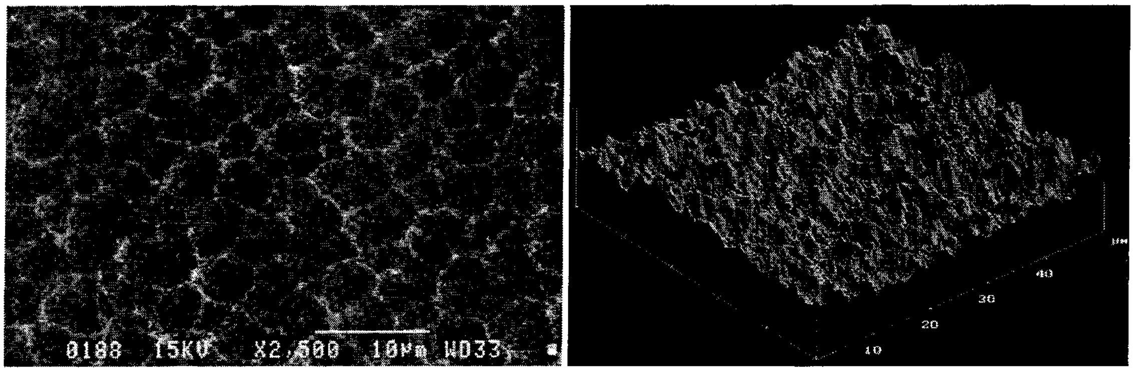

(a) (b)

Figure 4.4: (a) SEM and (b) AFM micrograph of the sample after etching with TMAH for 20 seconds.

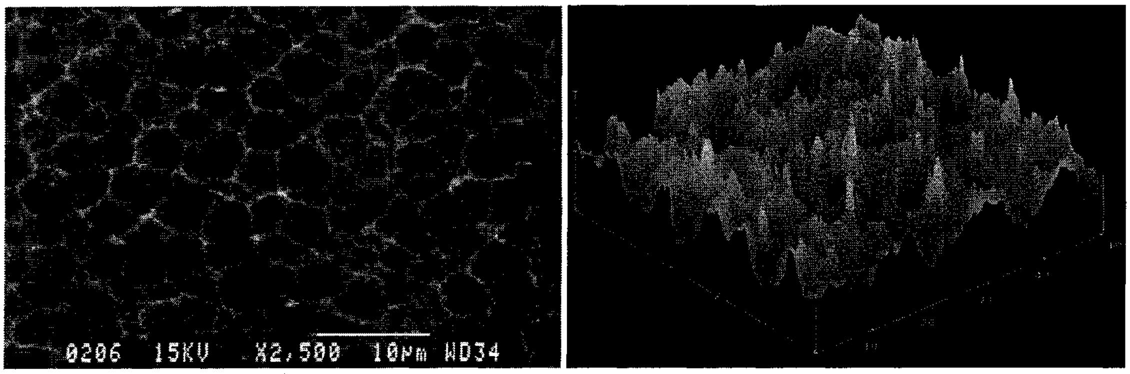

(a) (b)

Figure 4.5: (a) SEM and (b) AFM micrograph of the sample after etching with TMAH for 30 seconds

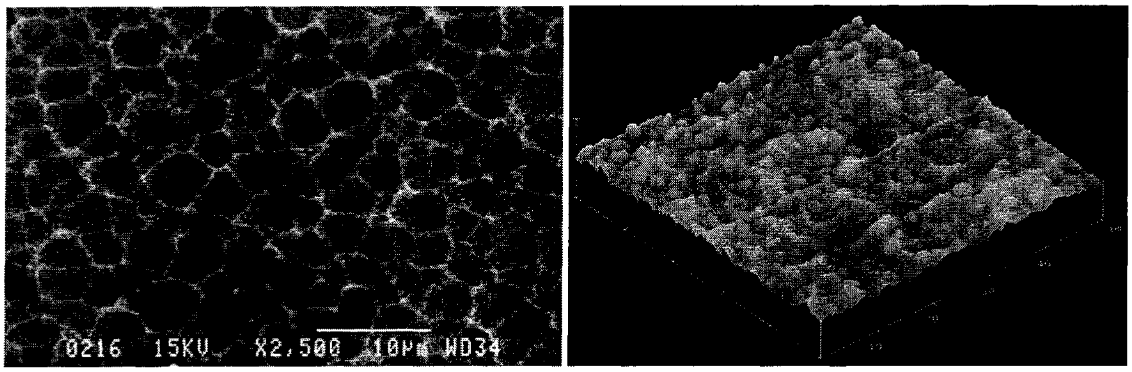

(a) (b)

Figure 4.6: (a) SEM and (b) AFM micrograph of the sample after etching with TMAH for 60 seconds

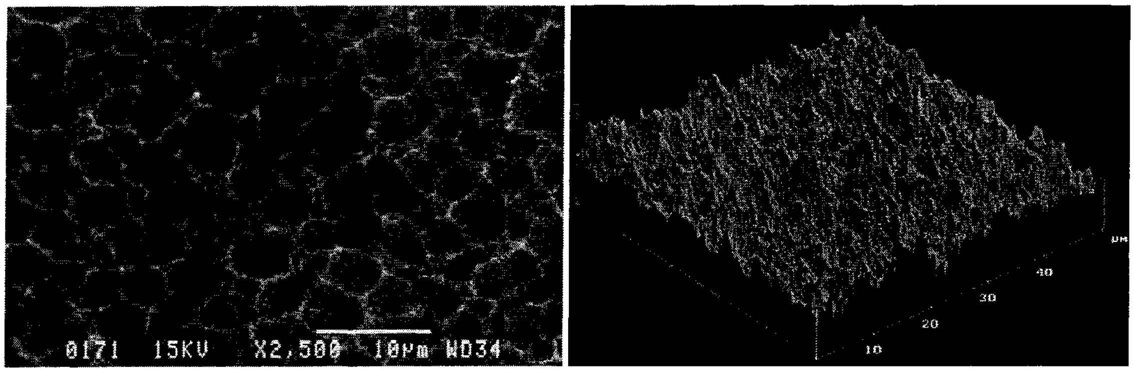

(a) (b)

Figure 4.7: (a) SEM and (b) AFM micrograph of the sample after etching with TMAH for 120 seconds.

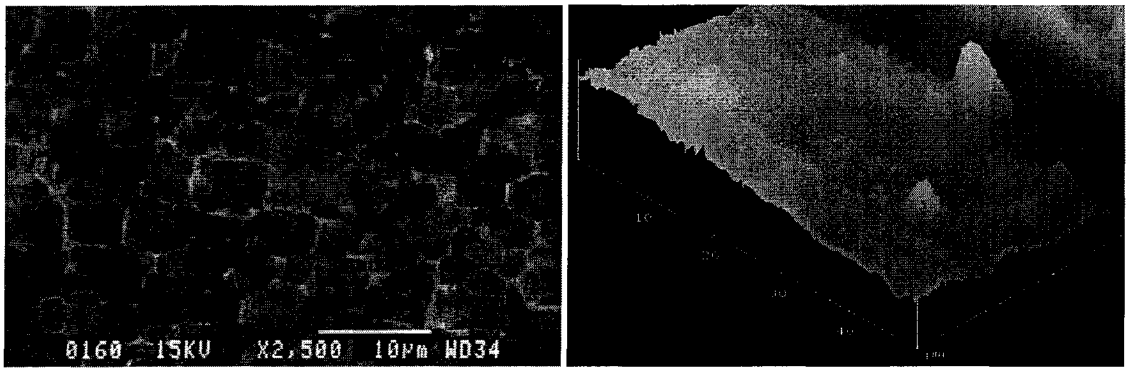

(a) (b)

Figure 4.8: (a) SEM and (b) AFM micrograph of the sample after etching with TMAH for 240 seconds.

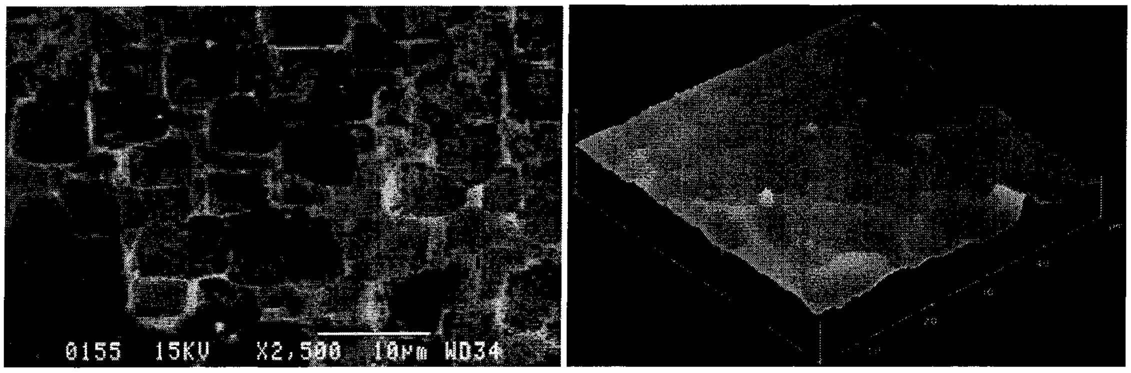

(a) (b)

Figure 4.9: (a) SEM and (b) AFM micrograph of the sample after etching with TMAH for 300 seconds.

The quantitative measurement of surface roughness was carried out using an Atomic Force Microscope at the Material Sciences Laboratory, Concordia University. Figure 4.10 shows the variation of root-mean-square (R_{rms}) and the average surface roughness (R_a) with progressive TMAH etching. The initial rms value of the surface roughness of the substrate is 213.4 nm with 13 pulses of XeF_2 etching.

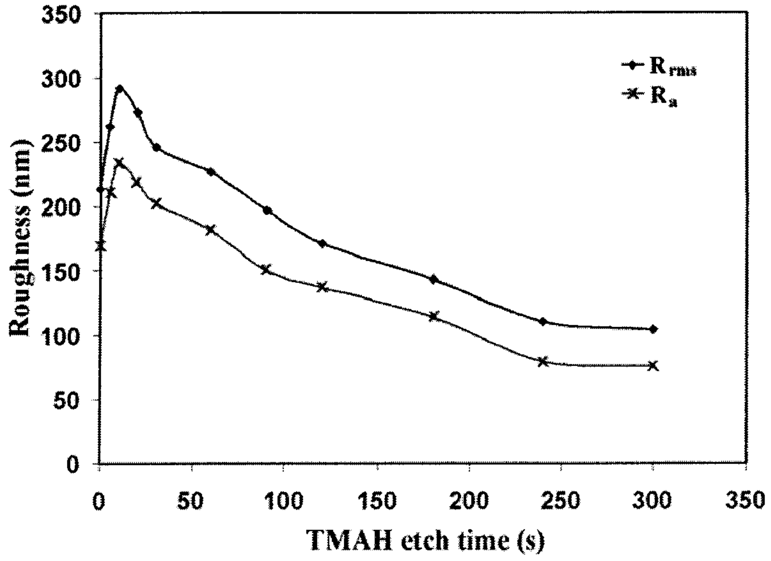

Figure 4.10: Variation of root-mean-square and average surface roughness with respect to the TMAH etch time.

It can be observed that the surface roughness increases initially when subjected to hybrid micromachining with TMAH etching. This phenomenon of initial increase in surface roughness is due to the random removal of atoms from the crystals over a previously etched uneven surface, which is known as microscopic roughness phenomenon [123]. However, with increased etch time, the macroscopic roughness effects due to the bulk etching with the anisotropic etchant dominate the microscopic roughness phenomenon and the surface roughness decreases with progressive hybrid micromachining.

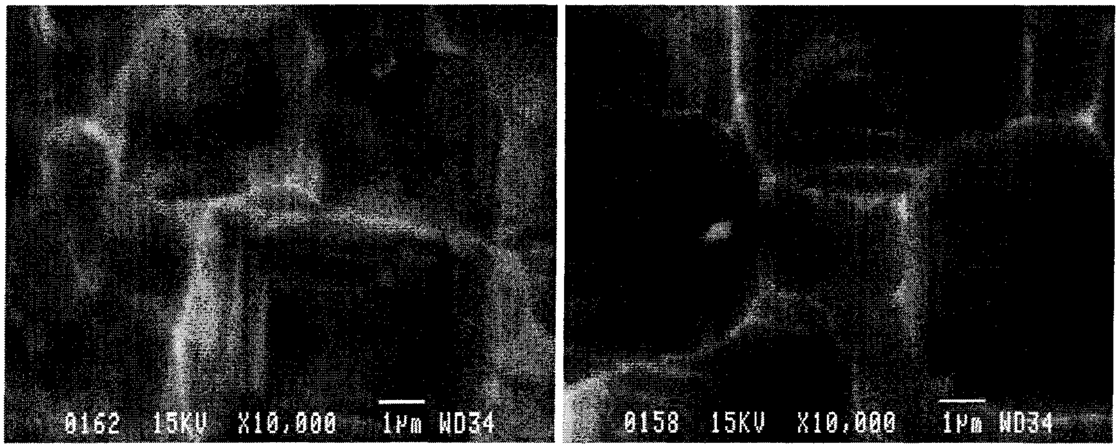

(a) (b)

Figure 4.11: SEM of samples subjected to hybrid micromachining for (a) 240 s and (b) 300 s under 10000x magnification

From Figure 4.11(a), it can be seen that at 240 seconds of etching with TMAH, slow etch slopes have started forming on the etched surface. Figure 4.11(b) indicates the development of the consequent slow etch planes after 300 seconds of etching. At this stage, the rms value of roughness is found to be 104.26 nm. Hence, a significant reduction of surface roughness has been achieved through the hybrid micromachining technique.

4.4 Improved scattering loss

The hybrid micromachining experiments were carried out in order to study the effect of surface roughness on optical microsystems. Scattering loss has been predicted for both the waveguide based and free space optical microsystems for various hybrid micromachined conditions. In order to demonstrate the improvement of scattering loss due to hybrid micromachining, the following example is presented.

A Finite Element Modeling of a standard SOI rib waveguide [124] as shown in Figure 4.12 has been carried out using FEMLAB for the following parameters:

n_1 (Refractive index of Silicon core) = 3.48

n_2 (Refractive index of bottom Silica glass cladding) = 1.46

H_w =0.5 μm

W_w = 0.5 μm.

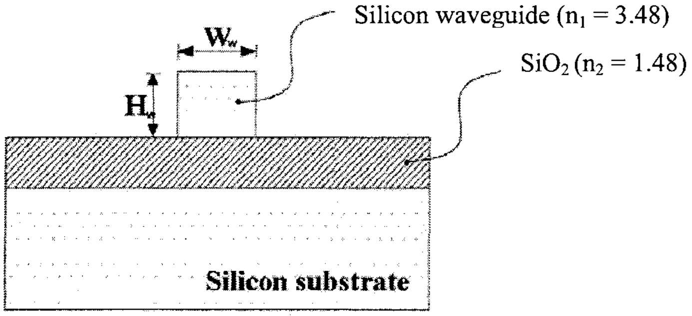

Figure 4.12: A schematic diagram of SOI rectangular waveguide used for finite element modeling with FEMLAB.

For a wavelength of 1.55 μm, the effective refractive index n_{eff} was found to be 3.3969. The standard deviation of the roughness variation along the sample and the autocorrelation length for the specimen is calculated from the data obtained through the AFM. These values were used for the computation of attenuation constant and optical loss (dB/cm) using Equations (2.32) to (2.34) for waveguide based systems. The results are tabulated in Table 4.1 and the variation of scattering loss with respect to the TMAH etch time is presented in Figure 4.13 (a).

Table 4.1: Variation of measured standard deviation and the Auto-correlation length of the rough surface with the time duration of hybrid micromachining.

Duration of Hybrid micromachining (s)	**Standard deviation (μm)**	**Auto-correlation length (μm)**
0	0.38	2.27
5	0.84	3.97
10	1.03	7.96
20	0.59	7.95
30	0.77	4.48
60	0.71	1.20
90	0.34	2.65
120	0.55	7.96
180	0.15	1.99
240	0.25	3.36
300	0.18	3.18

For non-waveguide based free space systems, the scattering coefficient is computed using the formula given in Equation (2.35) and for an angle of incident light $\theta_i = \pi/4$, the variation of scattering loss against the duration of hybrid micromachining is shown in Figure 4.13(b). The roughness induced scattering decreases with progressive hybrid micromachining for all angles of incidence of the light. The scattering loss is greater in case of smaller angles of incidence of the light and it decreases with increase in the angle of incidence. For light just grazing the surface of the micromirror, the scattering loss is minimal.

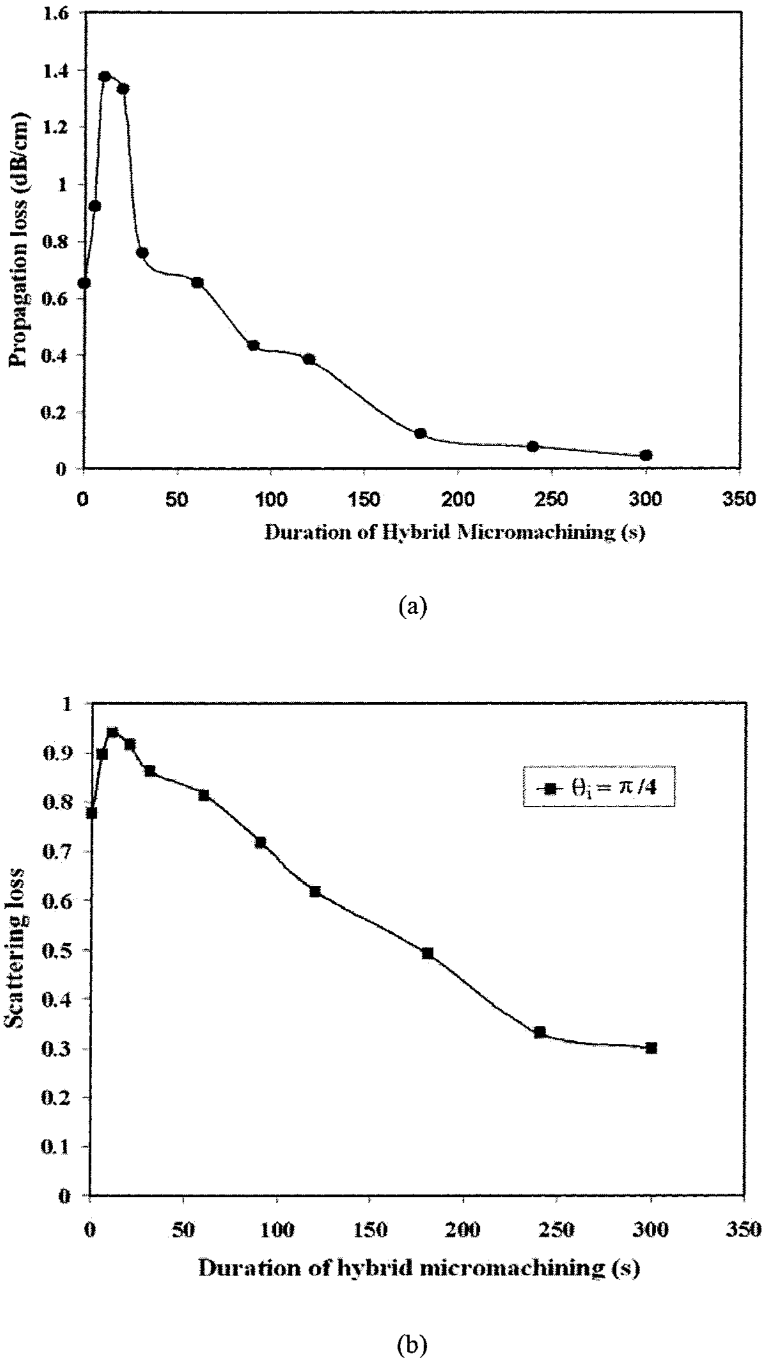

Figure 4.13: Effect of progressive hybrid micromachining on the roughness induced propagation loss in (a) waveguide based optical microsystems (b) in free spaced and non-waveguide based systems for an angle of incidence at $\pi/4$.

4.5 Summary

The effect of scattering loss is very important for the design of MOEMS devices. It is essential to optimize the optical loss due to surface roughness in MOEMS devices fabricated by different micromachining techniques. Hence, the study on the effect of surface roughness on scattering loss was carried out for waveguide based and non-waveguide based devices. The proposed hybrid micromachining technique is suitable for both waveguide and non-waveguide based optical microsystems. The effect of improved surface roughness through hybrid micromachining has been demonstrated by modeling a standard SOI waveguide and propagation losses. An improved optical performance has been observed due to the proposed hybrid micromachining technique.

Chapter 5

Biophotonic Enzymatic Detection

5.1 Introduction

In order to validate the authenticity of the proposed SOI based biosensor system and to corroborate the results obtained from simulation for its performance characterization, it is essential to carry out the testing of the waveguide based biosensor devices. The testing of the biosensors is important for determining the suitability of the proposed device for real-time applications. The biophotonic testing involves coupling the light from the source onto the waveguide, on which the enzymes are added, and collecting the light emerging out of the waveguide at the other end for analysis. Therefore, three independent modules, namely, the input light emitter, the biosensor and the collector detector are used in an ensemble. Since some of the light is lost during evanescence due to the presence of the enzyme and its reaction with the antibody, the study of the light at the waveguide output is an indicator of the amount of light evanesced and this principle is used for biosensing.

In this work, waveguide based devices fabricated by the SOI MicraGeM process and also by the anisotropic etching technique with TMAH have been tested for biosensing through principle of evanescence coupling of light.

5.2 Selection of enzyme

In Chapter one, a brief list of enzymes which have been used in optical testing was tabulated. However, the reaction time between the enzyme and the antibody varies depending upon the chemical properties. Since the volume of enzyme used in evanescence testing is less, the reaction time between the enzyme and the antibody should be sufficiently fast enough under room conditions so that the problem with the evaporation of the enzyme before the reaction occurs is avoided.

Horse Radish Peroxidase (HRP) is a redox enzyme (biochemical catalyst) with approximately molecular weight of approximately 40 kDa (1 Da = 1.660540×10^{-27} kg). It structurally resembles glycoprotein with one mole of protohaemin. These enzymes exhibit different isotropic forms and are generally isolated from the roots of horseradish [125].

When HRP comes into contact with selected substrate H_2O_2, it basically reduces the substrate. This reaction is spontaneous, within around 200μs [126]. When the enzyme is added on the antibody, it produces superoxide or the ROS (Reactive Oxygen Species) by the reduction of Hydrogen Peroxide. Due to this phenomenon, H_2O_2 clings on to HRP and forms like a "cotton structure" [127]. The main advantage of using HRP for testing is that its optical activity can be easily monitored and the activity is fairly stable in organic or inorganic solvents [128]. Figure 5.1 shows the molecular structure of HRP and the change in structure upon reaction with H_2O_2.

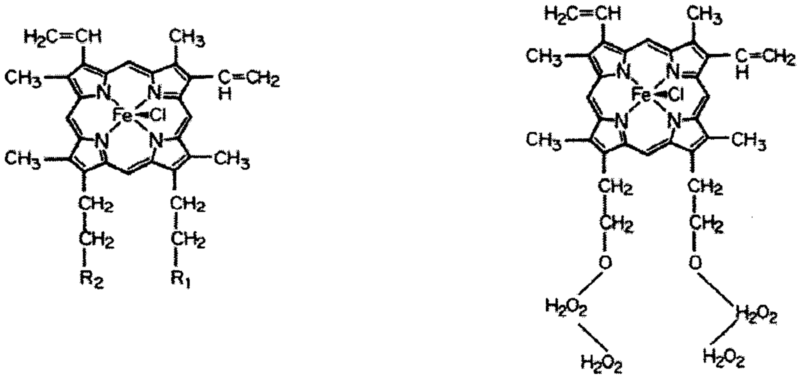

(c) HRP structure (b) HRP - H2O2 after reaction

Figure 5.1: Molecular structure of (a) HRP and (b) HRP-H_2O_2 after reaction [128]

HRP used in the experiments is a commercial grade 9003-99-0 bought from Sigma, St. Louis, USA and the hydrogen peroxide is the standard grade bought from Sigma, USA. The concentration of the enzyme used was 1% to the active ingredient in aqueous solution while the substrate H_2O_2 used was 30% by weight solution.

5.3 Absorption characteristics of enzymatic reaction

In order to use the antigen HRP for biosensing experiments, it is essential to characterize the optical activity of the specimen upon its reaction with the antibody over wide wavelength spectrum. It is known that the reaction between enzyme HRP and H_2O_2 exhibit optical activity at near UV and visible wavelengths [129,130]. These wavelength ranges are compatible with silica waveguides, however, this would mean the loss of biosensor development on silicon platform. Hence, the behaviour of the enzymes needs to be characterized at near infrared wavelength of 1550 nm.

It is known that the HRP- H_2O_2 reaction causes a small increase in the chain length of the enzyme. The time study of the reaction is important in order to analyze the reaction characteristics. Herein, three different optical spectrums at different wavelengths were used, which are, blue light at 470 nm of near UV wavelength, red light at 635 nm for visible wavelength and near infrared light at 1550nm, in order to study and quantify the wavelength dependant optical absorption characteristics of the enzyme-antibody reaction.

5.3.1 Absorption characteristics near UV wavelength

The first optical absorption experiment was carried out with light of near UV wavelength of 470 nm. The experimental setup for this optical testing is shown in Figure 5.2. It consisted of blue light emitted through a fiber optic bundle from pulsed xenon lamp source at 470 nm. The light was coupled onto a spectrometer (Ocean optics Inc.) The enzyme is taken in a micro pipette and is added to the substrate on a glass slide and the slide is introduced in the slot available with the light source.

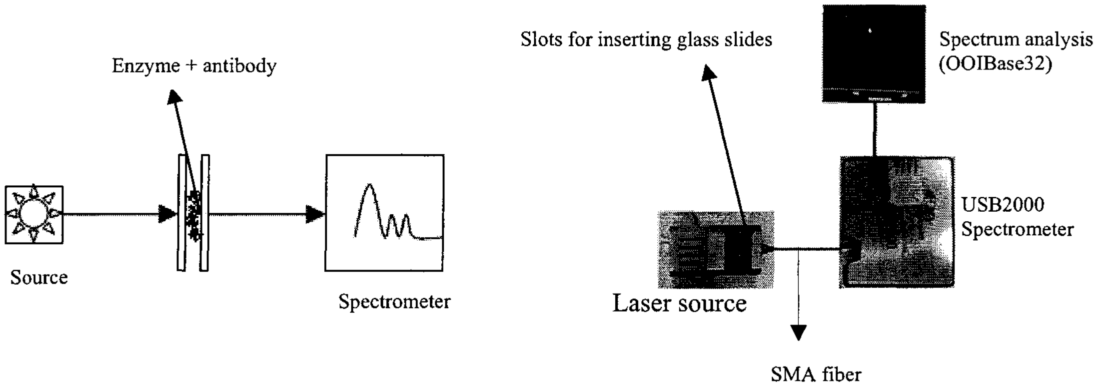

(a) Test scheme

(b) Test setup

Figure 5.2: (a) Schematic of the optical absorption experimental setup for near UV wavelength

The absorbance measured by the spectrometer is given by the formula

$$A_\lambda = -\log_{10}\left(\frac{S_\lambda - D_\lambda}{R_\lambda - D_\lambda}\right) \tag{5.1}$$

Where

λ - Wavelength of light used

A_λ - Absorbance

S_λ - Intensity of light passing through the sample

D_λ - Dark Intensity

R_λ - Intensity of light passing through a reference medium.

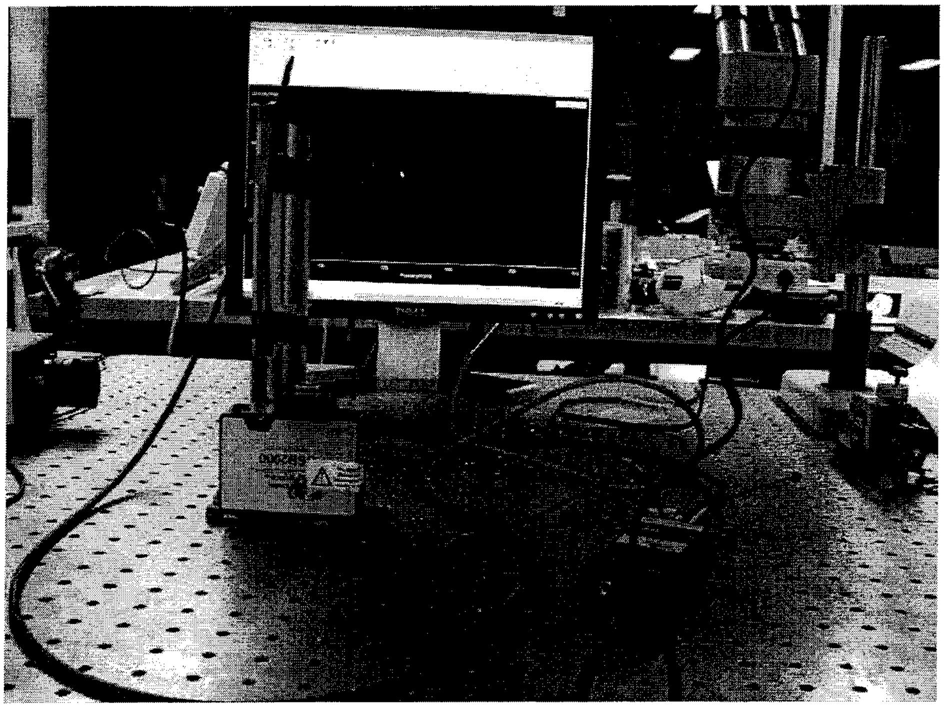

Figure 5.3: Optical absorption experiment setup with blue light at 470 nm.

Herein, the glass slides were taken as the reference and when the light was passed through plain glass samples, the reference intensity was noted. Dark intensity is measured when there is no light sensed by the spectrometer. However, in order to nullify the effects of the ambient conditions, the dark intensity was taken in the situation where the light source was switched off but the ambient light still was sensed by the spectrometer.

Figure 5.4 shows the plot of intensity against the wavelength for the different samples. The variation of light intensity transmitted through HRP- H_2O_2 at different volumetric concentrations is as shown from Figures 5.5 and 5.6. The plot of absorbance variation with time for different volumetric ratios of enzyme reactions is given in Figure 5.7.

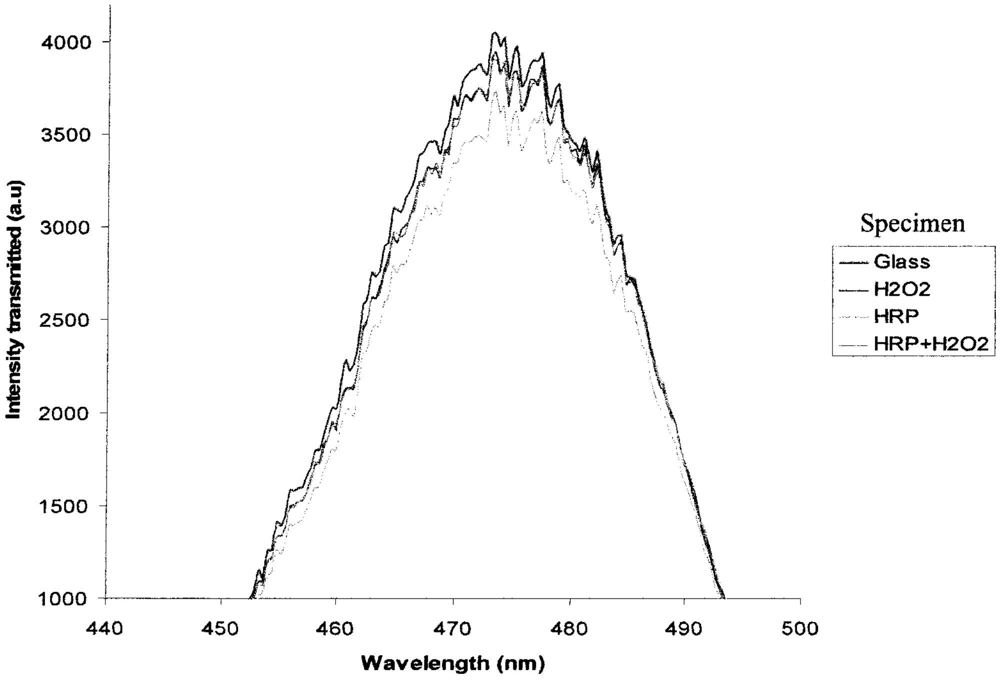

Figure 5.4: Intensity of light transmitted at 470 nm through different specimen, namely, glass, HRP, H_2O_2 and their reaction at 1:1 concentration respectively

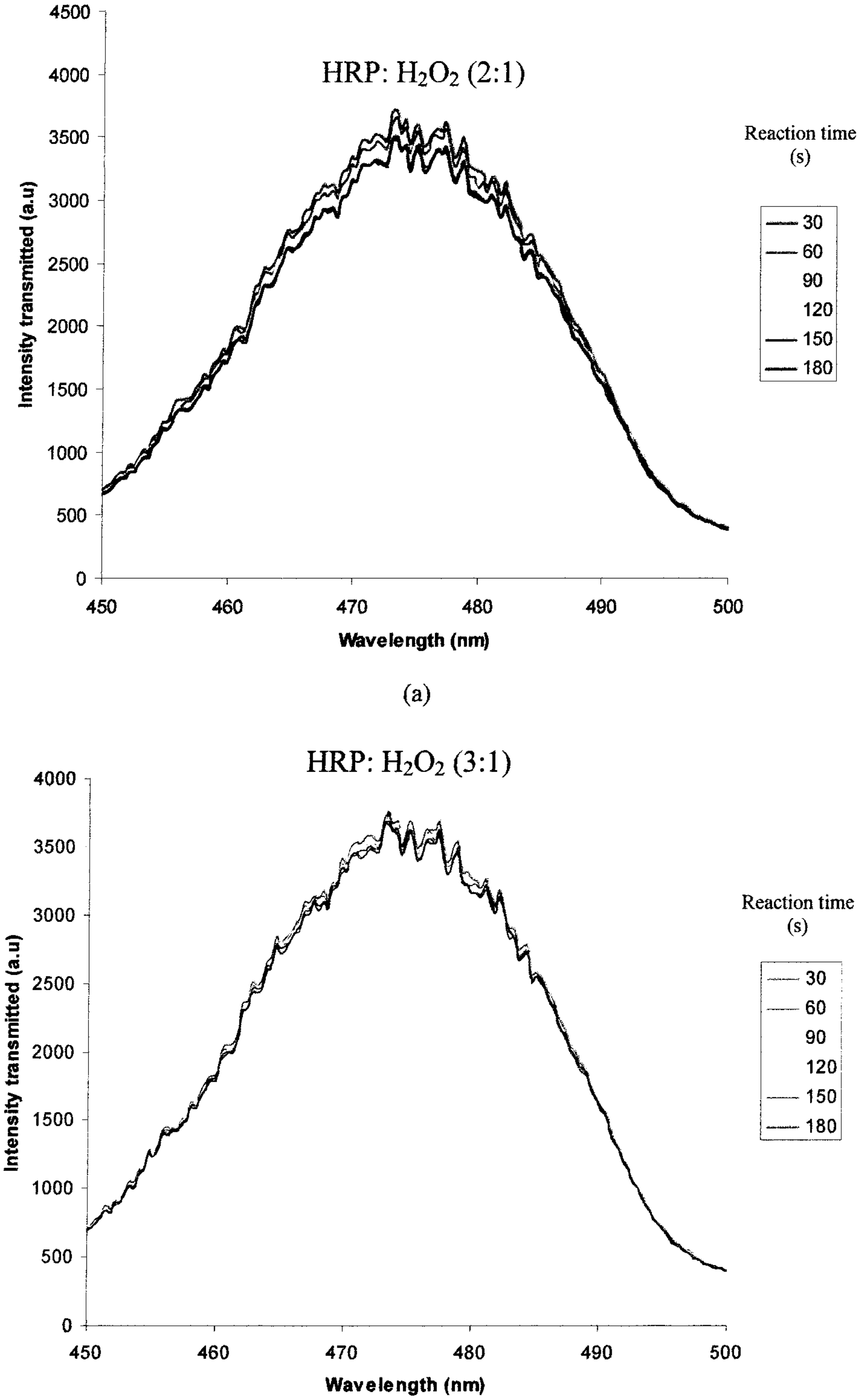

(a)

(b)

Figure 5.5: Plots of light transmitted at 470 nm through HRP- H_2O_2 taken at volumetric concentrations (a) 2:1 and (b) 3:1

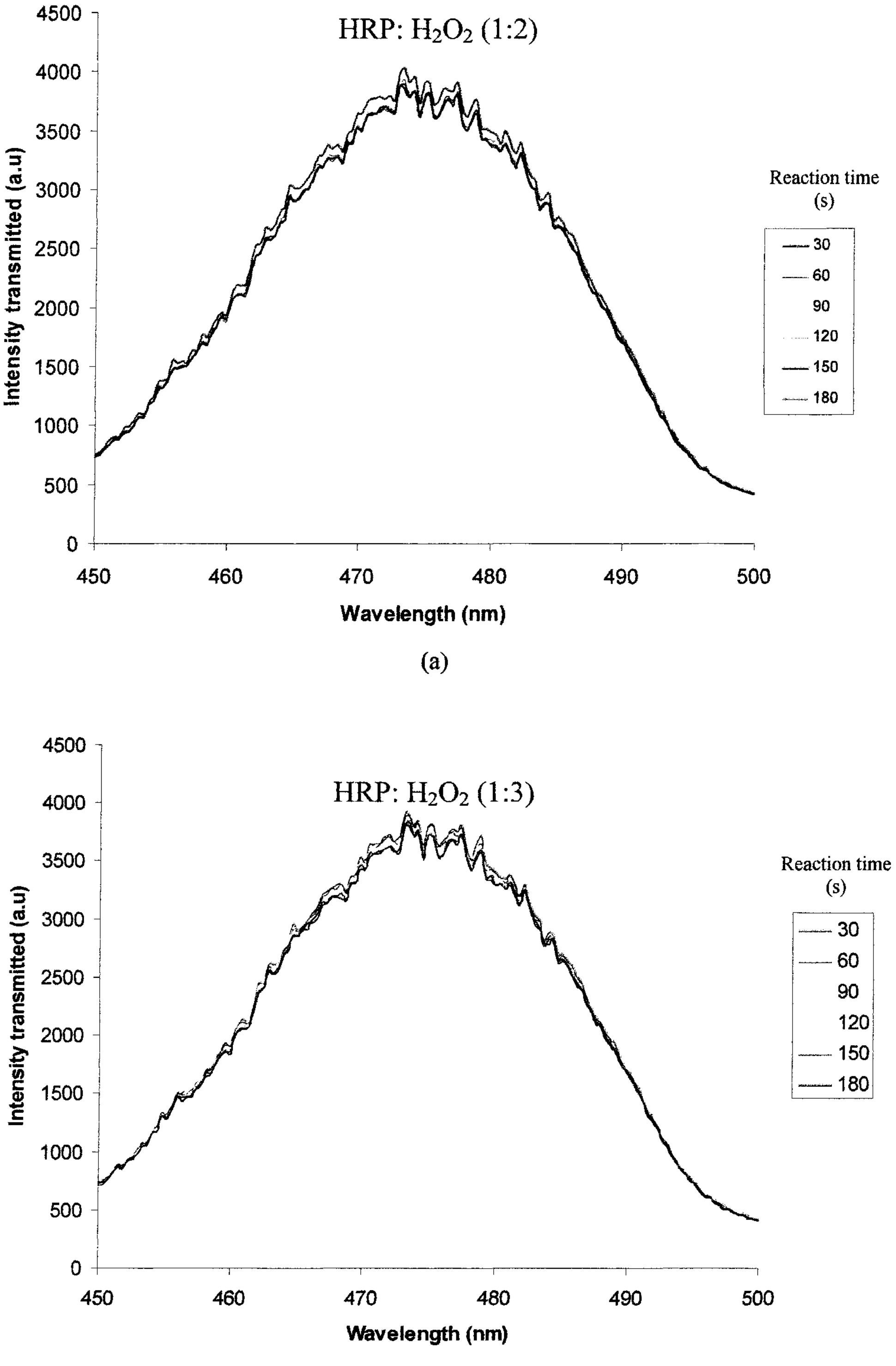

(a)

(b)

Figure 5.6: Plots of light transmitted at 470 nm through HRP-H_2O_2 taken at volumetric concentrations (a) 1:2 and (b) 1:3

It can be seen that the absorbance is maximum when the enzyme is reacted with the antibody in the same volumetric concentration. When taken alone, the enzyme HRP exhibits a slightly higher absorption than the antibody for the same volume of 1 µl. As the volumetric concentration of any one of the specimen is increased during reaction, the absorption behaves similar. Any further increase in concentration of either of the specimen moves the absorbance value closer to the value of HRP or H_2O_2 taken alone.

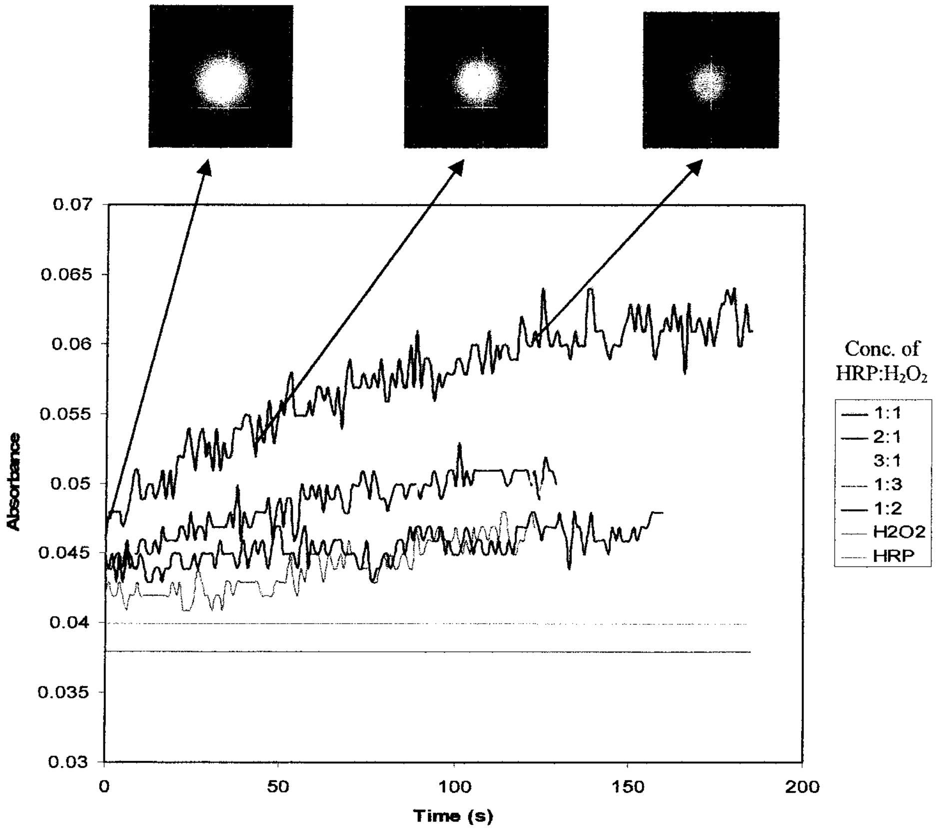

Figure 5.7: Plot of time-varying absorbance at 470 nm for different volumetric ratios of HRP- H_2O_2

5.3.2 Absorption characteristics with visible spectrum

The next absorption measurement experiment was carried out with red light at 635 nm wavelength. This is the wavelength range which is closer to the wavelength of the visible light. Therefore, the spectrometer setup was not used because of interference between the signal from the laser source and the stray light in the room conditions. The schematic of the experimental setup with the red light of 635 nm wavelength is as shown in Figure 5.8. Figure 5.9 shows the test setup for this experiment. Since the spectrometer sensitivity was high for visible light spectrum, a photodetector was used in this experiment. Pulsed light at 270 kHz was used and the output from the photodetector was studied using a standard oscilloscope (Agilent Technologies). A laser diode source (OZ Optics, ON) was used as the input of light through a fiber optic cable (Thor labs).

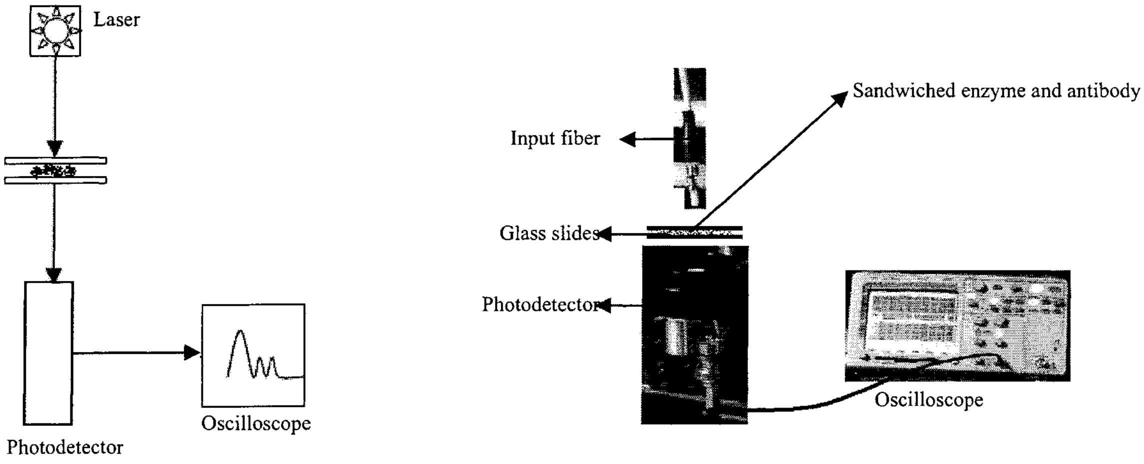

(a) Schematic setup

(b) Test setup

Figure 5.8: (a) Schematic diagram and (b) Test setup for absorption detection with light at 635 nm

The procedure adopted for absorption measurement was as follows. The fiber from the laser source was initially aligned with respect to the photodetector and the respective positions are maintained steady. Glass slide was placed on top of the photodetector and was coated with antibody H_2O_2. Enzyme HRP was then added to the antibody and another glass slide was used to cover the assembly.

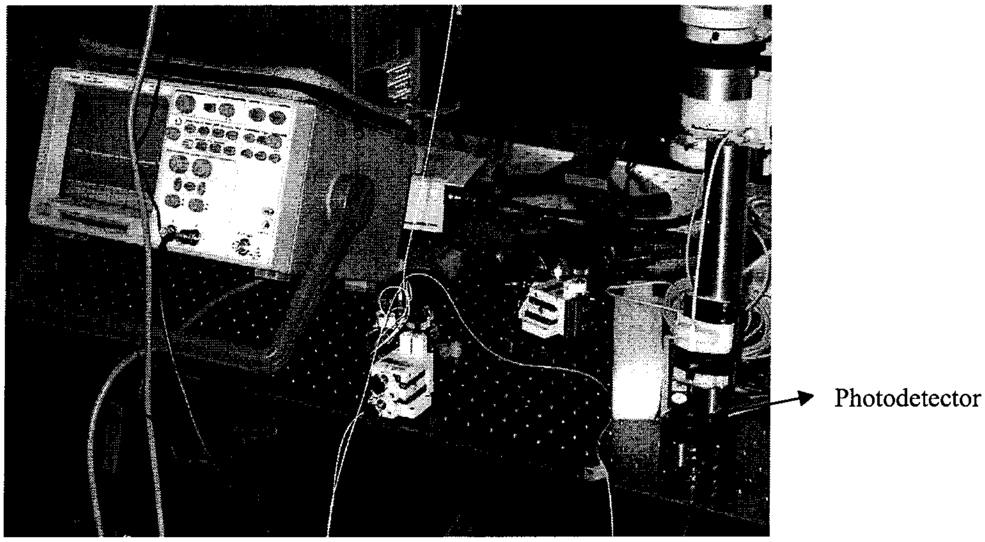

Figure 5.9: Experimental setup for absorption detection with red light at 635 nm

The output is obtained in terms of voltage given by the formula

$$V_0 = P_{pd} \times \Re_\lambda \times R_L \tag{5.2}$$

where

V_0 - the measured output voltage

P_{pd}- Power of input light in Watts

$\Re_\lambda$ - Resistivity of the photodetector measured in A/W.

R_L- Load resistance in the photodetector.

In order to convert the photocurrent into voltage, a load resistance of 50 Ω was added and the voltage reading was measured on the oscilloscope.

The optical propagation loss with time for different enzyme ratios is as given in Figure 5.10. It can be seen that equal volumetric ratio of HRP- H_2O_2 reaction produced the maximum absorption loss. However, H_2O_2 independently produced a slightly higher absorbance than enzyme HRP in this wavelength range and thus, the reaction between the two species produced more absorbance if the volumetric ratio of the antibody was higher.

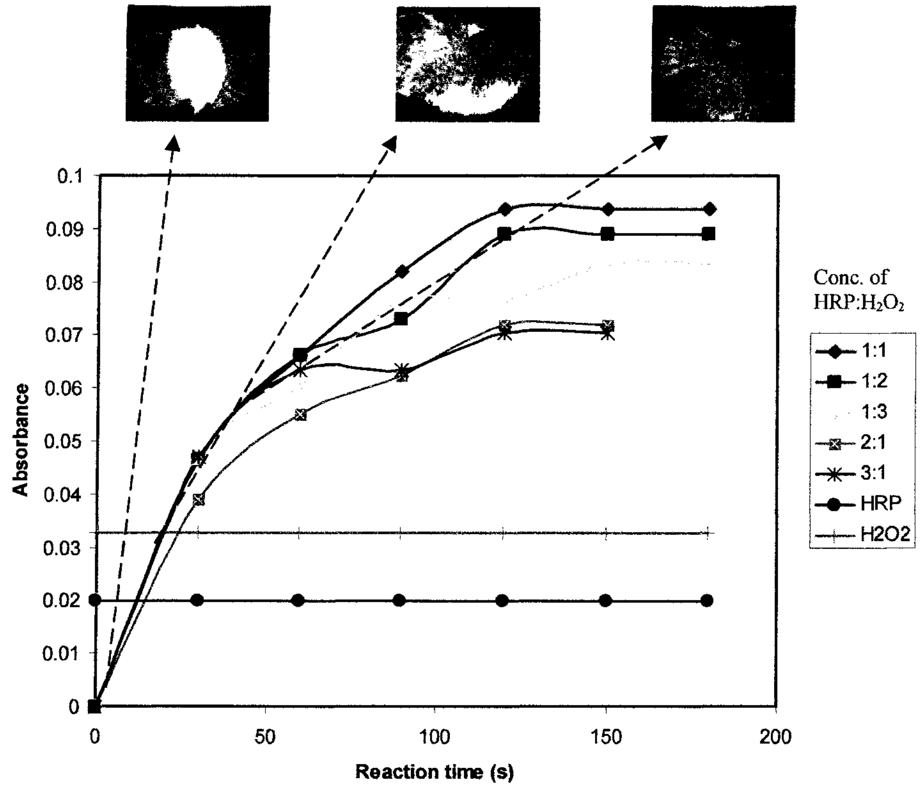

Figure 5.10: Plot of absorbance variation with time measured with a photodetector for the reaction between HRP and H_2O_2 taken in different volumetric ratios.

5.3.3 Absorbance measurements at infrared wavelength

All the experiments carried out so far were with visible light. Having characterized the enzyme behaviour with the visible light, it was important to study the reaction characteristics with infrared light, which would be compatible for evanescence measurements with SOI waveguides. The experimental setup for the absorption measurement using infrared source is as shown in Figure 5.12, the schematic for which is shown in Figure 5.11. The input fiber and the output fiber were fixed vertically on a clamping arm which was mounted on two independent xyz micropositioners. This setup enabled placing the glass slide directly on top of the clamping arm holding the GRIN lens and addition of the bio samples directly on top of the glass slide to measure instantaneous output readings.

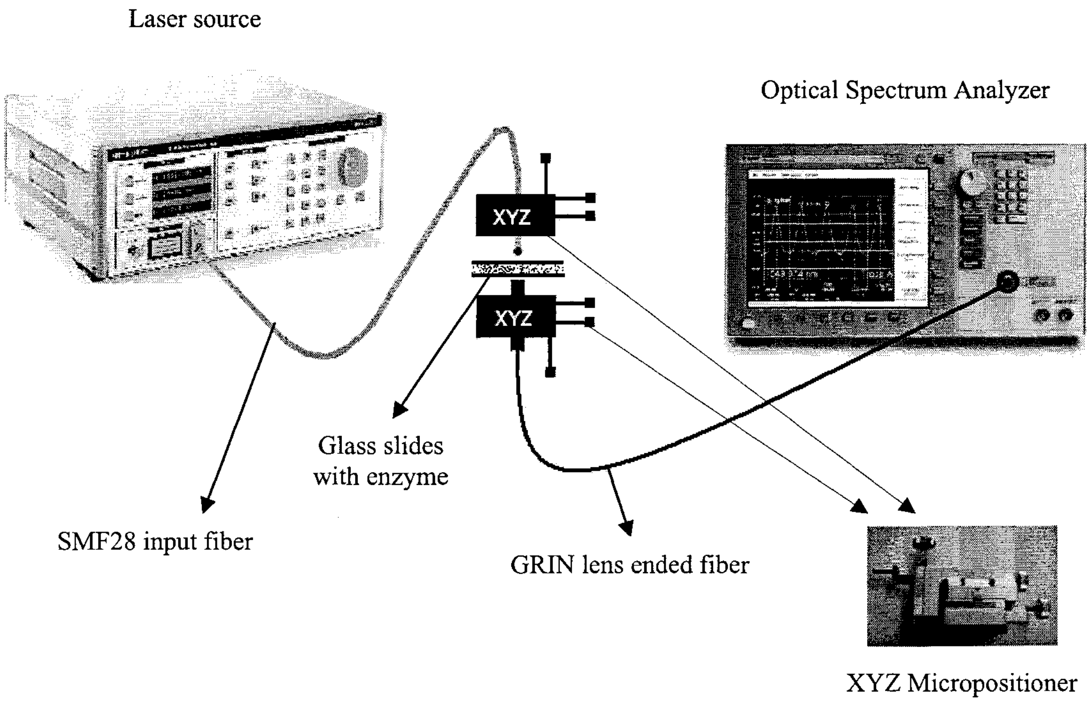

Figure 5.11: Schematic of the experimental setup for absorption measurement at 1550 nm

An Optical Spectrum Analyzer (OSA) (Agilent Technologies) was used to detect the light signals collected with the GRIN lens ended fiber. A standard SMF28 fiber (Thorlabs, USA) was used as an input fiber and the laser source (Photonetics Tunics BT external cavity laser) was tuned to a wavelength of 1550 nm with 7.01 dBm input power. The initial calibration of the OSA was done with reference to the laser source.

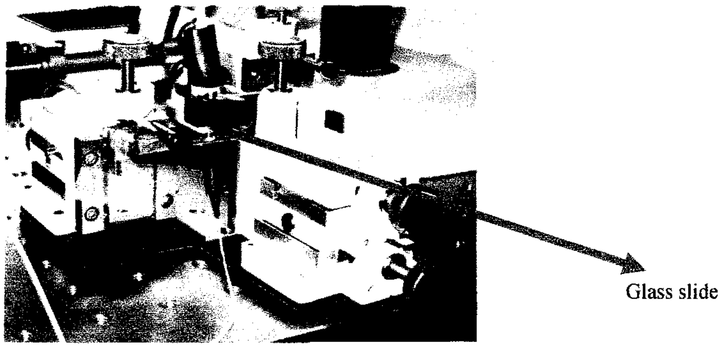

Figure 5.12: Experimental setup for optical absorption characterization of HRP-H_2O_2 using 1550 nm Infrared light.

The plot of optical loss with time is given in Figure 5.13. Herein, the absorbance is defined as $A_\lambda = -\log\left(\frac{P_t}{P_0}\right)$ where P_t is the power of light transmitted through the glass slides and P_0 is the power of input light. The reference value of optical power was taken as the amount of light passing through glass slides without enzymes.

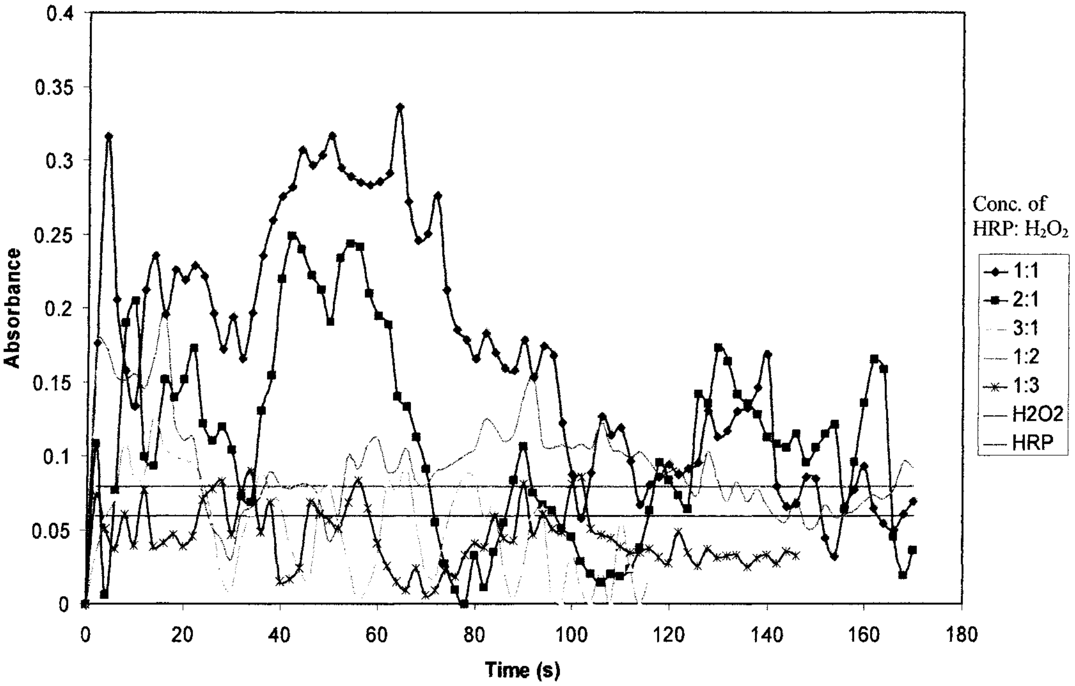

Figure 5.13: Optical propagation loss with time at 1550 nm for different volumetric ratios of enzyme HRP and antibody H_2O_2.

It can be observed that the loss is maximum when the reactants are added in the same volumetric concentration. Here, with the infrared light, the HRP exhibits more absorption than H_2O_2. At around 40 s, the absorption can be seen increasing and then after some time, the absorption decreases again. This sudden increase in absorption could be because of the formation of intermediate compounds during the reaction, as reported by Baek and Van wart [129]. After around 200 seconds after the reaction, the absorption trend irrespective of the concentration tends to be similar, which might signify the end of the reaction. Jeetender et al. [125] has reported the mechanical behaviour of cantilever with HRP-H_2O_2 reaction in which the time taken is around 220 s. Therefore, the results obtained with the optical absorption measurements are comparable with the values predicted for the HRP-H_2O_2 reaction time by mechanical methods.

From the absorption measurement experiments in the three different wavelength ranges, it is clear that the maximum absorption occurs during the reaction between HRP and H_2O_2, as taken in the given molar concentration. The reaction is reduced when the volume of either of the reactant is increased.

There are some other inferences which can be drawn from the absorbance experiments. Firstly, the reaction time of the enzyme-antibody is clear from the above experiments. As the chains form during the reaction, the absorbance of light in the sample of enzyme-antibody increases. The absorbance reaches a certain peak after around 100 s when the reaction is believed to have completed. After 180 s, the ensuing absorption is due to the remnants of the samples and not the absorption exhibited during reaction. When the experiment is continued for a longer time, it can be observed that the absorption slowly starts decreasing. This phenomenon is due to the evaporation of the specimen.

5.3.4 Calculation of absorption coefficients

The absorption coefficient was computed for the optical loss due to the enzyme reaction at each of the wavelength. From the maximum optical loss measured in dB the absorption coefficient was calculated as follows. The expression for absorbance loss is given as

$$\ln(P_{output}/P_{input}) = -\alpha_{ab}L_{ab} \tag{5.3}$$

where α_{ab} is the absorbance coefficient and L_{ab} is the absorbance length, which is the distance between the glass slides with the enzyme-antibody, measured to be 10 μm. The ratio P_{output}/P_{input} is calculated from the loss in dB, β_{ab}, obtained from the experimental results by the expression given as

$$\beta_{ab} = -10 \log(P_{output}/P_{input}) \tag{5.4}$$

Therefore, the expression relating the absorption coefficient and the propagation loss is given as

$$\beta_{ab} = -10 * \alpha_{ab} l_{ab} * \log (e). \tag{5.5}$$

From the absorption experiments for different wavelengths of light, the absorption coefficient was computed for the maximum optical loss. The values are tabulated in Table 5.1. The results obtained from the absorbance measurements obtained from the experiments were compared with the previously published results [129,130]. In the published results, the concentration of the enzyme-antibody was not the same as the ones used in the present experiments. For example, Haesun et al. [129] have used 1 μM HRP with 1 mM H_2O_2 in 50% methanol and have obtained absorbance value of ~0.03 which is close to the value of 0.035 obtained for absorbance measurements with H_2O_2 alone, as seen from Figure 5.7. Similarly, the absorbance value of ~0.02, as reported by Akita et al.[130], is the nearly the same value obtained when absorbance measurement experiments were carried out for H_2O_2 taken independently at 635 nm wavelength. Therefore, it is evident that absorbance is maximum when specimens are taken in 1:1 volumetric concentration for the given enzyme activity.

Table 5.1: Absorption coefficients for the HRP- H_2O_2 reaction.

Wavelength of light (nm)	**Maximum absorbance for HRP- H_2O_2 (1:1) reaction**	**Previous results obtained**	**Loss in dB**	**Absorption coefficient (cm^{-1})**
470	0.06	~ 0.03 [129]	0.6	138.155
635	0.09	~ 0.02 [130]	0.9	207.37
1550	0.3	N/A*	3	690.77

*** Not Available**

It can be seen that the absorption is maximum in the infrared region for the enzyme sets. Therefore, absorbance method is not ideal for biosensing using infrared light. However, in order to develop a biosensor on SOI platform, it is essential to use the light at 1550nm wavelength for which the silicon is transparent. Therefore, it is essential to develop a suitable technique of biosensing which can be compatible at the infrared wavelength of optical spectrum.

5.4 Evanescence testing

The study of absorption characterization reveals that, even though absorption property of an enzyme upon reaction with its antibody causes a study of biosensing, it is heavily dependant upon the volume of the reactants used. In real-time applications of a biosensor, one cannot expect the molar concentration of the enzymes to be on similar lines with the samples taken for experiments thus far. In such cases, the absorption measurement may not be a good factor to be considered for biosensing. Hence, it is important to use the principle of evanescent wave coupling for accurate and controlled biosensing.

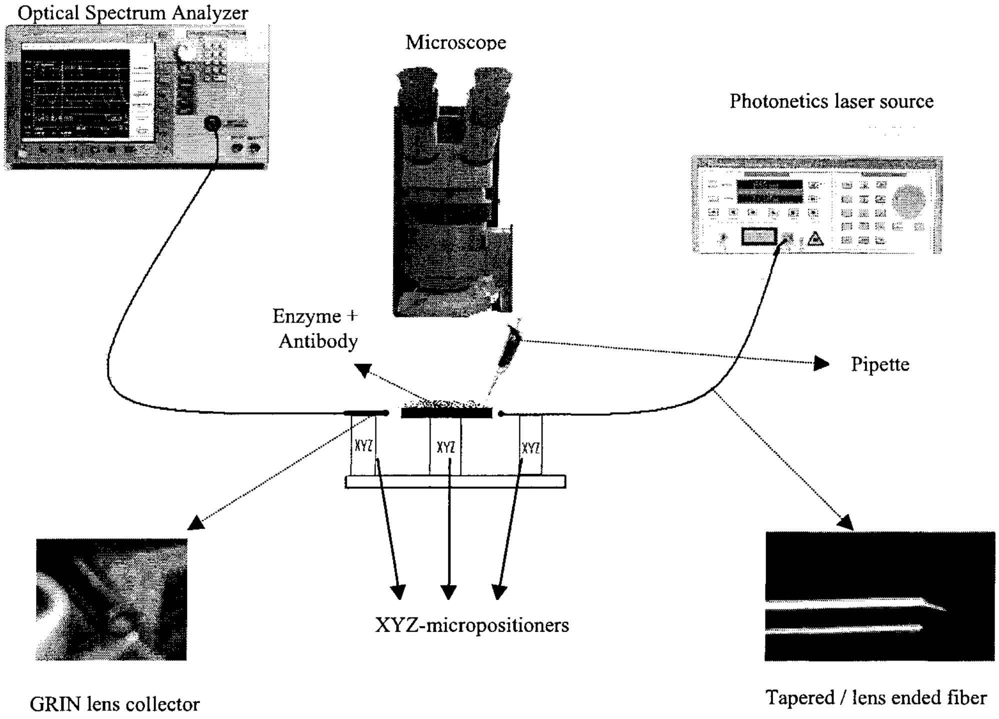

Figure 5.14: Schematic diagram of the evanescence testing setup at λ = 1550 nm.

The schematic diagram of the evanescence testing setup is as shown in Figure 5.14. The biophotonic testing setup for evanescence measurement at the Optical Microsystems laboratory is as shown in Figure 5.15. The input light at 1550 nm was guided through a fiber from a laser source (Photonetics, Tunics BT). A tapered lens ended fiber (OZ optics, ON, Canada), which gives a spot size of 5 μm at a distance of 26 μm, was used as the input fiber. One end of the fiber was an FC-PC connector and the other end was the tapered lens through which light is emitted into the waveguide. Both the tapered lens fiber and also the waveguide device were mounted on individual xyz micropositioners so as to enable separate alignment of each module. The light coming out of the waveguide was collected using the GRIN lens mounted on an adjustable positioner capable of ±1 mm adjustment along the vertical and the lateral axis. The GRIN lens ended fiber was connected to the OSA for the quantification of the power output.

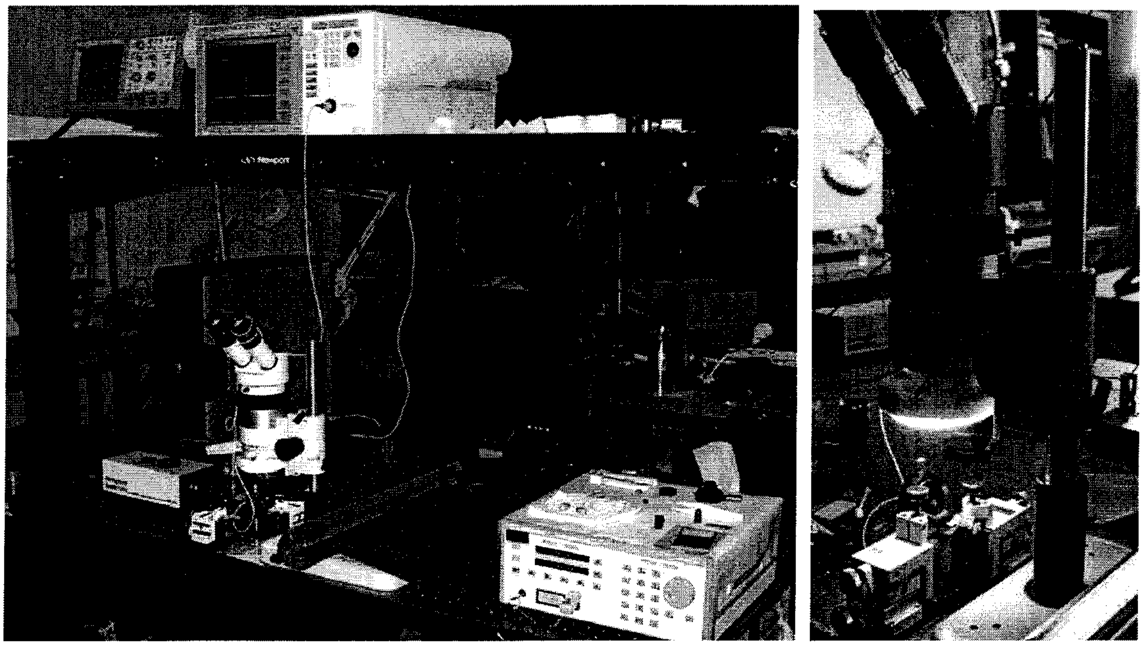

Figure 5.15: Biophotonic testing set-up developed at the Optical Microsystems laboratory

For qualitative analysis, an Infrared Camera (Electrophysics 7290A) was used to capture the beam coming out of the SOI waveguide. The output image was monochrome 8-bit RS-170 output which was compatible with a television monitor with a standard BNC input. But, in order to capture the image, the camera was hooked up with an 8-channel-input-parallel-output cable to the computer through PC2vision frame-grabber (Dalsa-Coreco, Montreal) supported by Sapera software (Coreco Inc.).

5.4.1 Evanescence testing on MicraGeM rectangular rib waveguides

The rib SOI waveguides fabricated with the MicraGeM process were used for testing the biosensibility with HRP-H_2O_2. The waveguide device was mounted on a xyz micropositioners and the tapered lensed input fiber was placed on another positioner. The alignment of the waveguide with respect to the fiber was carried out by observation under the microscope. A MicraGeM waveguide device aligned with the input fiber is shown in Figure 5.16.

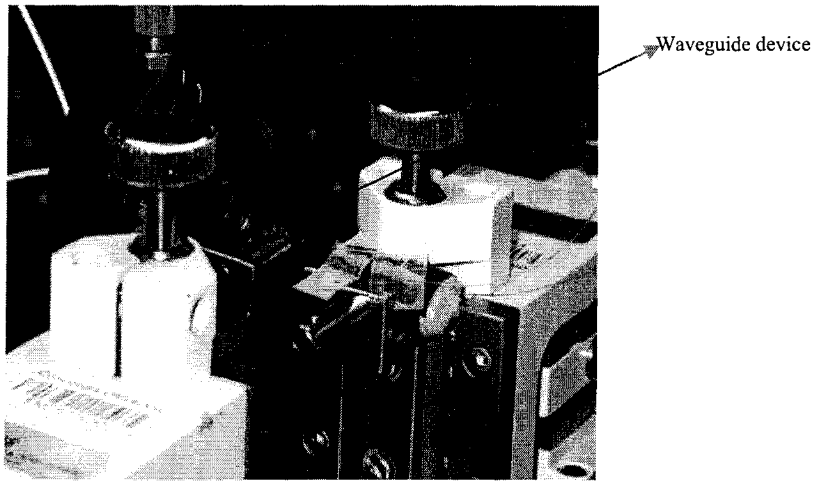

Figure 5.16: Setup of the optical fiber alignment with the MicraGEM waveguides

In this experiment, it was essential that the optical loss be studied under evanescence avoiding the loss due to absorption. Also, there was the need to clean the waveguide after every testing process. Therefore, static waveguides were used. The cantilever waveguides were not suitable for testing in the present case, because, they deflect upon the addition of load leading to optical loss due to absorption and due to the possibility of snapping during cleaning.

Initially, the position of the input fiber with respect to the GRIN lens was adjusted and the reading of the power output from the OSA was noted. The waveguide mounted on the micropositioners was slowly raised and the vertical alignment if the waveguide with the input fiber was carried out. The lateral alignment was carried out by the following procedure. Since there is a series of waveguides fabricated, when the position of the chip was altered to record the power. Hence, it could be known whether the light was being guided through the waveguide or being dispersed in free space – in the gap between the adjacent waveguides. By observation under the microscope, the position of the waveguide and the fiber could be monitored. Once the lateral alignment was perfectly carried out, in order to verify the accuracy of the vertical alignment, a sample of the enzyme was added on a random waveguide away from the waveguide on which evanescence test was intended to be carried out as shown in Figure 5.17.

Figure 5.17: Test method to verify the vertical alignment of the waveguide.

The enzyme and the antibody were added using a precision volume pipette (Gilson) capable of pipetting 0.2-2 μl of fluid. After testing, the waveguide was cleaned using Isopropyl Alcohol (IPA). A cotton swab was soaked with IPA and the remnants of the enzyme were gently scrapped off the surface of the waveguide. The surface was again cleaned with DI water and introduced in a flux of Nitrogen gas so as to dry out the water and prepare the waveguide surface for evanescence testing again.

5.4.1.1. Results

Since the area covered by the waveguides was small, the amount of enzyme and the antibody added had to be as minimal as possible. The minimum volume of liquid that could be added using the pipette was 0.2 μl, which usually engulfed the device, thereby causing a lot of absorption losses. Hence, the procedure of partial fluid addition was adopted, i.e., though the volume taken in the pipette was 0.2 μl, the actual amount of fluid added was less than that. However, this method was not successful in all trials. Therefore, the experiments were repeated for sufficient number of times till the results showed the loss due to possible evanescence, without absorbance. It should be remembered that the optical loss due to material absorption was quite high.

Three successful experiments were conducted isolating the effect of complete light absorption by the enzymes, while studying the evanescence using the MicraGeM waveguides. The results of optical loss due to evanescence are plotted in Figure 5.18 along with the pictures of the corresponding reactions. In the practical application of a biosensor, always the enzyme is added on to the antibody. Therefore, in the tests carried out, H_2O_2 was first immobilized on the surface of the waveguide and HRP was subsequently added to start the instantaneous reaction, thereby enabling the study of evanescence due to the changing optical field around the waveguide.

The trend for evanescence is similar for Tests 1 and 3. However the evanescent field length is different for both these cases as seen from the corresponding reaction pictures. This could be the reason for difference in evanescence loss measured. There is also another possibility here. In case of Test 1, H_2O_2 was added initially and then HRP was added to the antibody. However, in Test 3, H_2O_2 was added subsequently after HRP was added initially, against the usual method, so as to check the evanescence due to HRP alone initially and then due to the reaction. Therefore, there may be a possibility of a slightly different result in the way the reactants are added. From test 2, it can be seen that the enzymes added have engulfed the waveguide surface, therefore the results for Test 2 plotted in Figure 5.18 could be the result of combined absorption and evanescence.

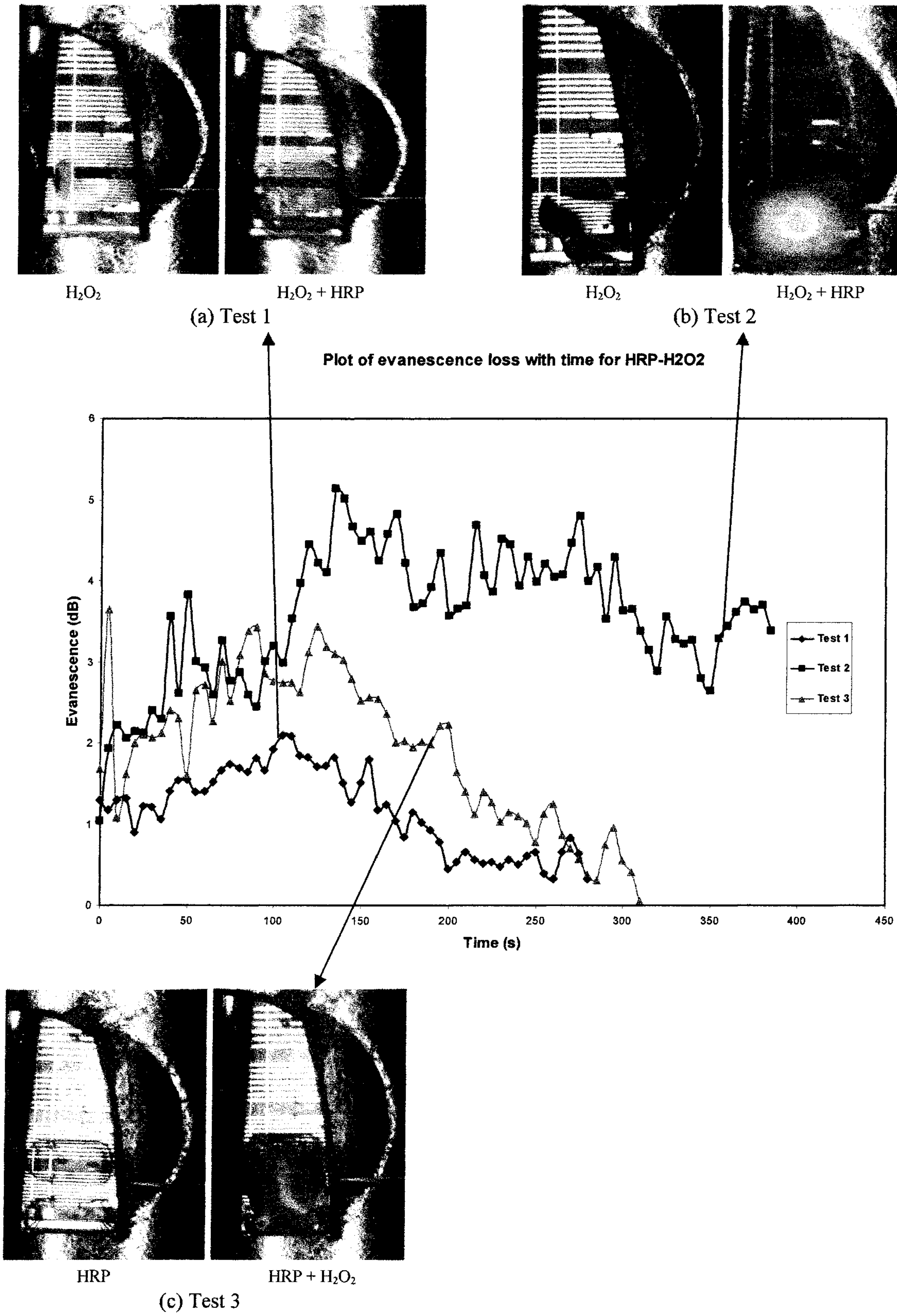

Figure 5.18: Plot of the evanescence loss with time for HRP- H_2O_2 and the enzyme reaction on the waveguide as seen under the microscope for different trials of evanescence study.

5.4.2 Evanescence testing with anisotropically fabricated SOI rib waveguides

The evanescence testing results for the experiments performed on MicraGeM device formed a good platform for carrying out the biophotonic testing on anisotropically etched SOI waveguides. There were some practical advantages of using the TMAH micromachined SOI waveguides in testing than MicraGeM waveguides. Firstly, the waveguides were longer which would allow more evanescence. Secondly, handling of the device was easier given the larger size of the sample. It was easier to align the tapered and lensed input fiber nearer the waveguide face, which was difficult with the MicraGeM waveguides due to the possibility of allowing the enzymes to overflow and cover up the fiber. However, the spot size of the beam was close the height of the waveguide. Hence, it was essential to carry out the testing for evanescence avoiding possible loss due to absorption. Given the irregularities in the microfabrication along with the multimode nature of the waveguide, the loss of light propagating through the waveguide was considerable.

In order to demonstrate the evanescence due to the sidewall taper, waveguides with walls inclined at 35.26^{o} were used for the experiments. The testing setup was the same one as used with the MicraGeM devices. Instead of using the double sided tape for holding the sample, plasticine was used as the support. The alignment of the fiber with respect to the waveguide was carried out as mentioned for the MicraGeM waveguides. After initial vertical alignment, the horizontal alignment was monitored and adjusted under the microscope. Similar to the experiments with the MicraGeM waveguides, the anti-enzyme was immobilized on to the surface of the waveguide and the enzyme was added to it. The volume of both anti-enzyme and enzyme was ~1 μl. Figure 5.19 shows the SEM pictures of the waveguide surface with the different specimen. It is thus known that when the enzyme is added and the antibody is introduced, there is a biological layer which is formed on the surface of the waveguide, as seen in Figure 5.19, which causes evanescence. The results of the evanescence study have been plotted in Figure 5.20, along with the reaction between the enzyme and the antibody which occurred during evanescence.

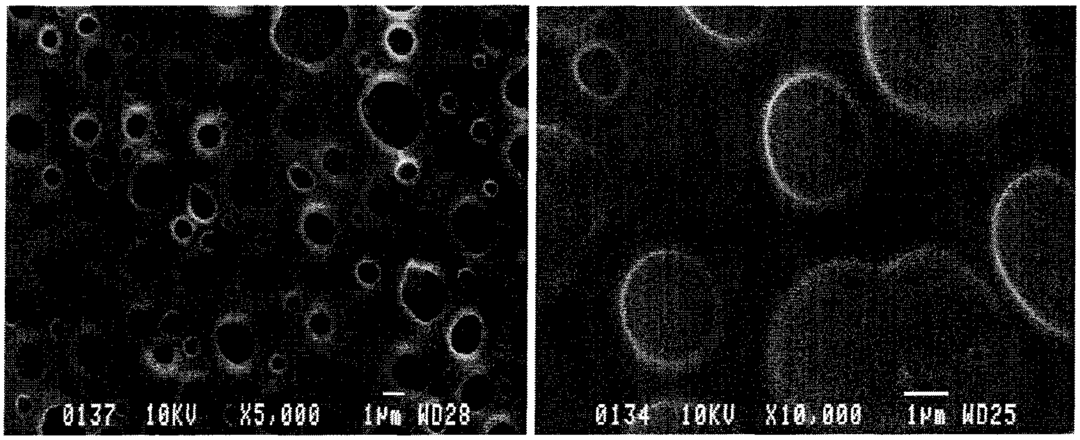

(a) H_2O_2 (b) HRP

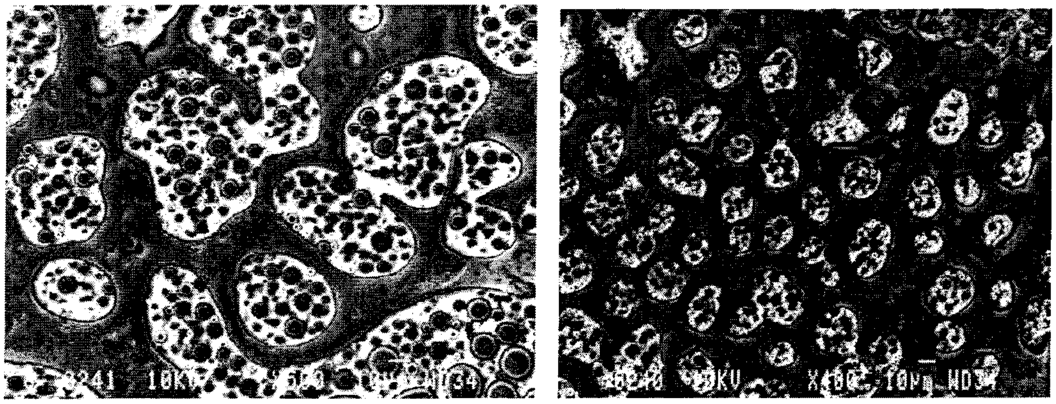

(c) HRP-H_2O_2

Figure 5.19: SEM Picture of the waveguide surface with (a) H_2O_2 (b) HRP (c) HRP- H_2O_2

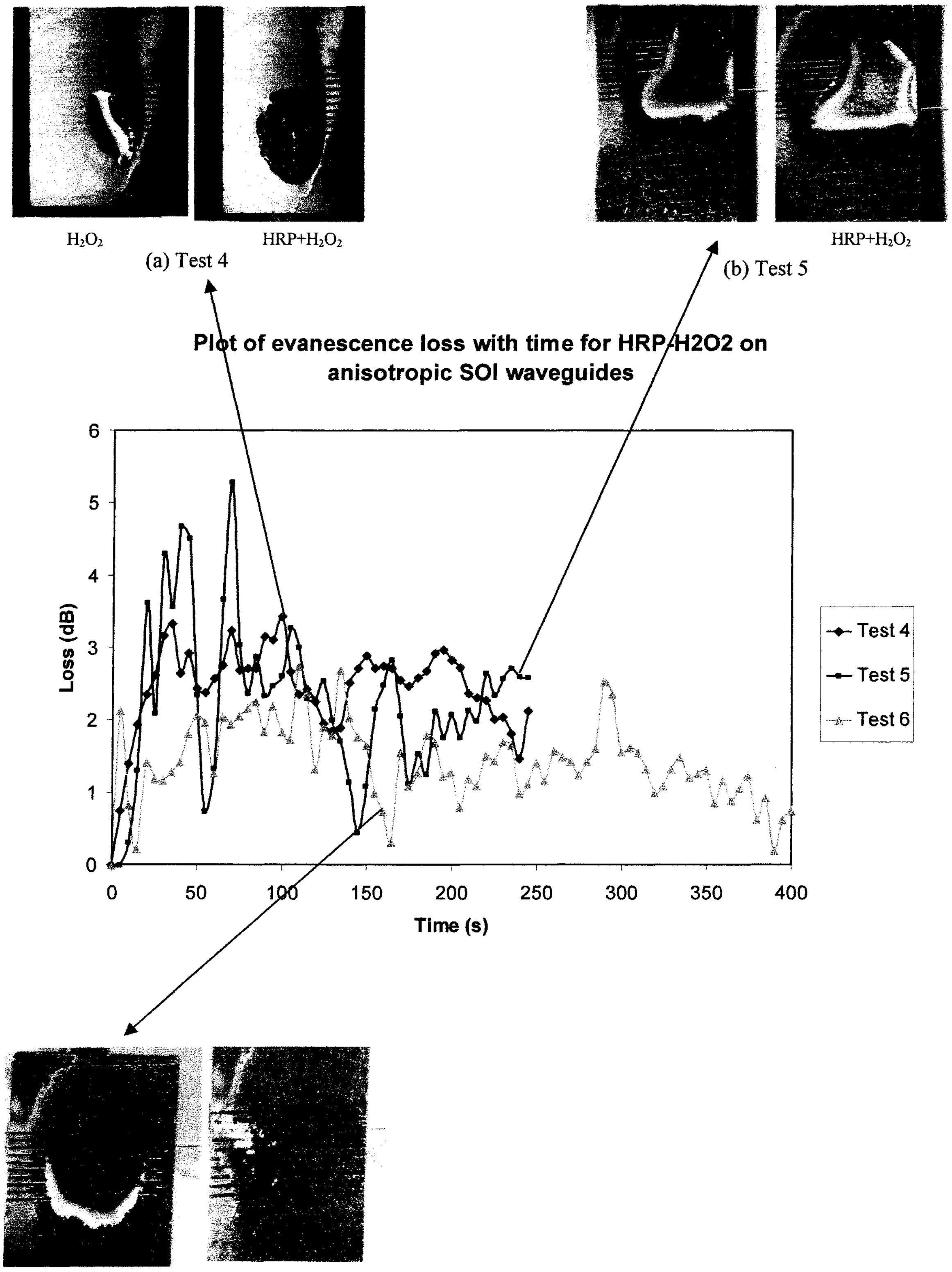
(a) Test 4

(b) Test 5

(c) Test 6

Figure 5.20: Plot of evanescence loss with time for the reaction between HRP and H_2O_2 on anisotropic silicon waveguide with taper angle 35.26°

5.4.3 Calculation of evanescence coefficient

From the evanescence loss for the waveguides, the evanescence coefficient of the HRP-H_2O_2 reaction was calculated. In this way, all the evanescence measurements recorded thus far in the experiments on the MicraGeM and the SOI waveguides are standardized. The following procedure was adopted in calculating the evanescence loss for the calculation of evanescence coefficient.

From the results of the experiments which were carried out by adding HRP and H_2O_2 individually and measuring the power loss, the evanescent loss coefficient was computed for each of the specimen. The length of the waveguide was measured to be 1320 μm. The individual evanescent field lengths of the enzymes were measured from the corresponding pictures taken under the microscope. Let the length of the waveguide covered by the specimen, in microns, be denoted by L_{sp} (sp = HRP or H_2O_2) and the power loss measured on the OSA after the addition of the specimen be ΔP_{sp}. Therefore, the evanescence loss in dB/cm is given by the relation

$$\beta_{sp}\,(\text{dB/cm}) = (\Delta P_{sp}/ L_{sp}) \times 10^{4} \qquad (5.7)$$

From Test 3, $\Delta P_{HRP} = 0.73$ dB and $L_{HRP} = 720$ μm. Therefore, the value of β_{HRP} was calculated as 10.13 dB/cm. Similarly, the evanescence loss for H_2O_2 was computed as the average of the losses measured in Test 1 (11.18 dB/cm over 715 μm), Test 2 (10 dB/cm over 1200 μm) and Test 4 (5.98 dB/cm over 880 μm). The value β_{HRP} is taken as 9.056 dB/cm.

For the computation of the evanescence coefficient, it is assumed that evanescent field length over which the reaction occurs is the length of the waveguide over which the antibody was immobilized initially. Accordingly, the total loss due to evanescence was computed by the following relations.

Total evanescent loss β_{ev} (dB/cm)= $(\beta_m \text{ x } L_m)+(\beta_{HRP} \text{ x } L_{HRP})$. (5.8)

Here, β_m and are taken as the evanescence due to enzyme reaction. The length covered by the reacting enzymes, L_m, is assumed to be the same length of the waveguide covered by the antibody added initially. From the above relation, the evanescent coefficient was calculated from the relation

$$\beta_{ev} = 10*\alpha_{ev}*\log_{10}(e),\ \therefore\ \alpha_{ev} = \beta_{ev} / [10*\log_{10}(e)] \quad (5.9)$$

The evanescent loss is taken as the maximum power loss observed during the reaction. The values of the evanescence coefficient obtained from the different experiments are tabulated in Table 5.2.

Table 5.2 : Evanescent coefficient for the different tests carried out on the MicraGeM waveguides for the HRP-H_2O_2 reaction.

Experiment with MicraGeM waveguides	Maximum evanescent loss (dB)	Average evanescent loss (dB)	Evanescent length due to enzyme reaction (μm)	Evanescent loss (dB/cm)	Evanescent coefficient of the enzyme reaction (cm^{-1})
Test 1	2.108	1.519	720	12.655	2.91
Test 2	5.148	4.231	1320	32.05	7.37
Test 3	3.656	2.75	1200	22.01	5.067

For the anisotropic waveguides, a similar calculation was carried out and the evanescence coefficient was calculated as given in Table 5.3. A second degree polynomial trend line was added through the data points obtained and the peak of the trend line is taken as the average evanescence value.

Table 5.3 : Evanescent coefficient for the different tests carried out on the TMAH micromachined SOI waveguides for the HRP-H_2O_2 reaction.

Experiment with anisotropic waveguide	Maximum evanescent loss (dB)	Average evanescent loss (dB)	Evanescent length due to enzyme reaction (μm)	Evanescent loss (dB/cm)	Evanescent coefficient of the enzyme reaction (cm^{-1})
Test 4	3.43	2.89	988	8.79	2.02
Test 5	5.289	2.48	3300	7.515	1.73
Test 6	2.65	1.65	2541	6.493	1.49

5.5 Validation of experimental results

In order to verify the authenticity of the proposed biosensor system, it is essential to validate the experimental results obtained with the simulation results. Simulation was carried out by BPM technique using R-Soft and the evanescence was computed.

A model of MicraGeM waveguide with the parameters as shown in Figure 5.21 (a) was designed and the BPM was carried out. The evanescent loss was computed using two inbuilt function of the R-Soft, namely the *Total power (TP)* function and the *Waveguide power (WP)* function. The total power function computes the total power in the computed optical field at the relevant z-position and the waveguide power function computes the integral power in the calculated field at the relevant z-position over the waveguide cross-section. Therefore, the evanescent loss was calculated as

$$\text{Evanescent power loss EP (dB)} = WP_{sp}\text{ (dB)} - WP_{air}\text{ (dB)}. \tag{5.10}$$

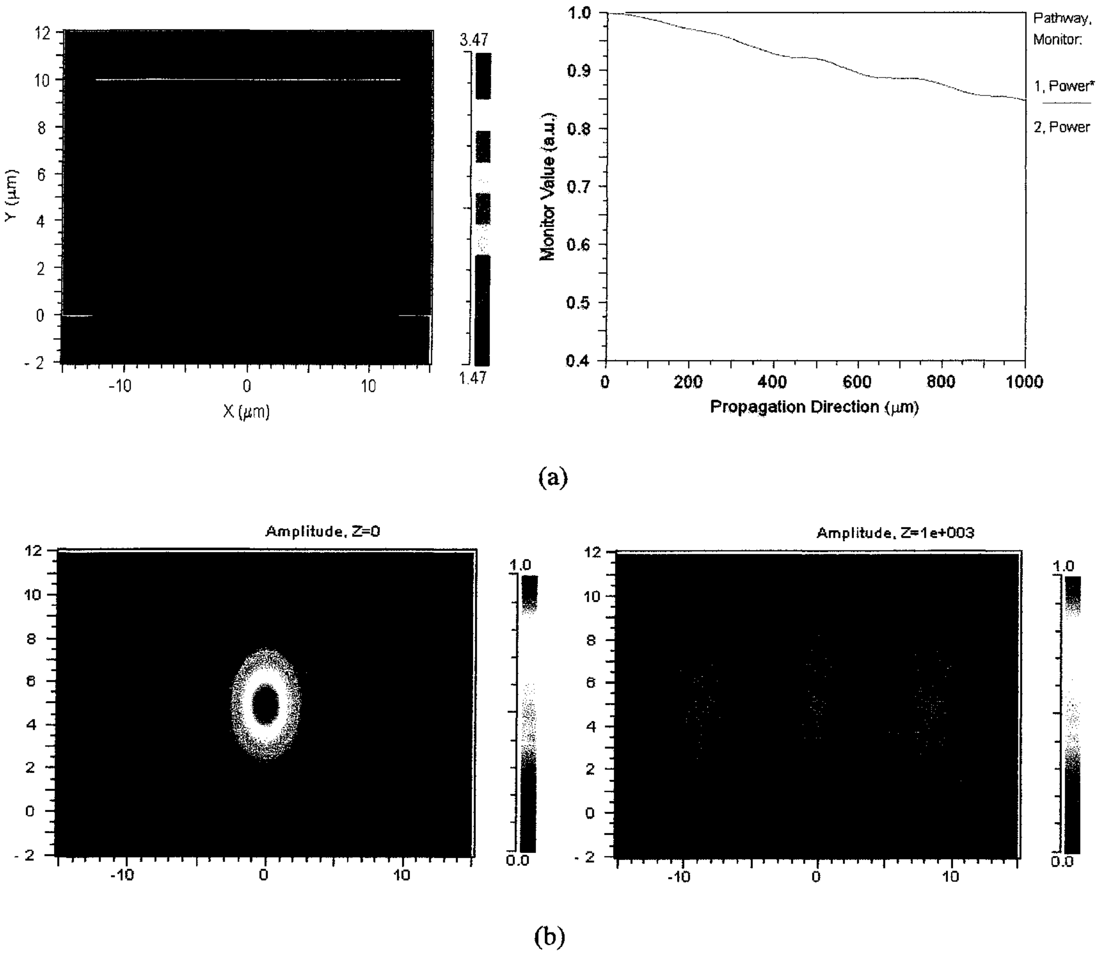

(a)

(b)

Figure 5.21: (a) Refractive index profile of the modeled waveguide and monitor value of the total power and the waveguide power obtained from the BPM of MicraGeM waveguides N_{clad} = 4+2i (b) Field amplitude at the input and the waveguide output

WP_{sp} is the waveguide power due to the specimen cladding and WP_{air} is the waveguide power with air cladding. The simulations were carried out by varying the refractive index of the covering medium of the waveguide and the evanescent power loss was determined for each condition. The length of the waveguide was taken as 1000 μm. The value of the waveguide power at z = 0 gives the optical coupling loss between the fiber and the waveguide. From the results obtained, the loss in dB/cm was obtained and the coefficient of evanescence was calculated for the different conditions, as presented in Table 5.4.

A model of anisotropic SOI waveguide was drafted as shown in Figure 5.22(a) and the BPM was carried out for various refractive indices of the medium. The evanescent loss was computed as tabulated in Table 5.5. The relative evanescent loss shown in Table 5.4 and 5.5 show the increase in evanescent loss with increase in refractive index of the cladding. This phenomenon demonstrates that evanescent loss occurs due to the change in the optical properties of the cladding.

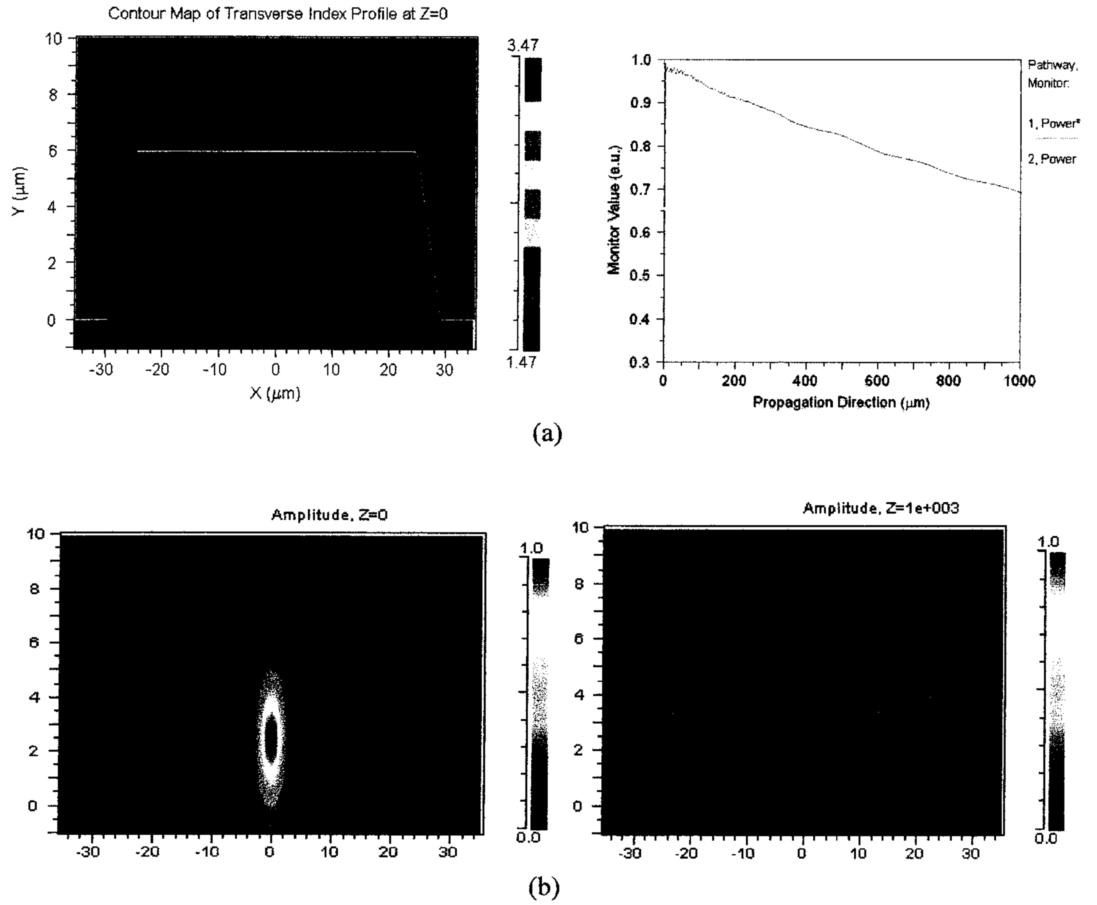

Figure 5.22 : (a) Index profile and monitor value of anisotropically micromachined SOI waveguide with taper angle 35.26° with N_{clad} = 4+2i (b) Field amplitude at the input and the waveguide output

Table 5.4: Evanescent loss measured with BPM on MicraGeM waveguides.

Refractive index of covering medium	Evanescence per 1000 μm (dB)	Evanescent loss (dB/cm)	Relative evanescent loss (dB/cm)
1	3.01	30.1	0
2 + 2i	3.32	33.2	3.1
3 + 2i	3.56	35.6	5.5
4 + 2i	3.73	37.3	7.2

Table 5.5: Evanescent loss measured with BPM on anisotropic SOI waveguides.

Refractive index of covering medium	Evanescence per 1000 μm (dB)	Evanescent loss (dB/cm)	Relative evanescent loss (dB/cm)
1	3.29	32.9	0
2 + 2i	3.64	36.4	3.5
3 + 2i	4.02	40.2	7.3
4 + 2i	4.32	43.2	10.3

There are certain issues which have to be noted in drawing a comparison between the simulation results and the experimental values of evanescence obtained. One must note that, it is practically impossible to create a simulation system with the real-time conditions because of several physical and biological factors. Secondly, all the theoretical evanescence calculations have been approximated in measurements of the evanescent field lengths. In case of computation of the evanescence coefficient using the MicraGeM waveguides, the evanescent field was assumed to be along the top of the waveguide and and the sides. The experiment suffers from certain limitations like the scattering of light due to sidewall roughness, minor misalignment losses and calculation of the exact refractive index of the cladding material. Incorporating these factors involve an independent study in that direction which is not being taken up now. Therefore, the results presented so far have demonstrated the phenomenon of evanescence with change in the refractive index of the cladding material.

5.6 Summary

In this chapter, the biophotonic testing procedures and the results have been presented. The enzyme HRP was chosen for the demonstration of the evanescence based testing, and the detection was carried out through the reaction of HRP with its antibody Hydrogen Peroxide. Optical activity of the enzymes in different wavelength ranges was characterized by absorption measurements. Experiments were then carried out on the MicraGeM waveguides and the anisotropically etched SOI waveguides for biosensing using evanescence principle. In order to compare the experimental results obtained, BPM simulations were carried out for the evanescence on MicraGeM rectangular rib waveguides and the TMAH micromachined anisotropic waveguides using R-Soft, and the phenomenon of evanescence in the waveguides due to the increase in the refractive index of the cladding has been demonstrated.

Chapter 6

Conclusions and future works

6.1 Conclusion

In this thesis, waveguide based devices on SOI platform have been designed, modeled and tested for biophotonic enzymatic detection using the method of evanescence sensing. The fabrications of the SOI waveguides were carried out using the SOI MicraGeM process technology and the in-house technique of anisotropic etching using TMAH. The feasibility of biosensing has been demonstrated using the enzyme set of HRP and the corresponding antibody H_2O_2.

As discussed in Chapter 1, research has been going on currently to develop evanescence based sensors for the detection of various enzymes. One must remember that in practical applications of a biosensor, the concentration of a particular enzyme present in a sample used for detection is of the order of a few ppm. Therefore, evanescence detection would not be helpful in such cases for large waveguides. But, in order to realize evanescence based sensors for practical applications, it is essential to fabricate a device on a highly miniaturized scale of the order of a few microns to nanons, capable of biosensing even small concentrations of enzymes. It is here that silicon carries with itself some associated advantages in turning out to be the ideal platform for fabricating an effective biosensor. The single mode condition of the silicon waveguide is achieved when the dimensions are of the order of a few nanons to sub microns. The advantages of using SOI for waveguiding have been discussed. However, in order to utilize silicon for waveguiding, it is essential to use infrared light because, material absorption is high for the light in other wavelength ranges. Given the optical activity of the specimen in the infrared wavelength, evanescence is proposed to be a suitable method for biosensing.

The modeling of the waveguides was carried out using three methods, namely, the Finite Difference (FD) method, the Finite Element Method (FEM) and the Beam Propagation Method (BPM). In the FD method, the different modes for the tapered waveguides were solved by extending the previous work on straight waveguide to a tapered waveguide approach. The Maxwell's scalar wave equation was discretized to formulate the finite difference relations and the different boundary conditions were applied in order to compute the amplitude of the field at each point on the grid and to obtain the propagation constant for different conditions of evanescence. The results of propagation constants obtained were compared with the FEM simulated through commercial software FEMLAB. Scalar BPM analysis was carried out on rectangular and the anisotropic tapered waveguides using R-Soft.

The micromachining possibilities of these waveguide based devices have been explored using the SOI MicraGeM process technology and the anisotropic etching using TMAH. While the MicraGeM technology is an industrial technology which has been made available through the CMC, the anisotropic etching is an in-house technique ideal for micromachining tapered waveguides. The limitations of these micromachining processes are that the geometry of the waveguides that are fabricated is limited, which can be overcome by adopting other fabrication techniques such as DRIE and isotropic XeF_2

micromachining. But apparently, there exists a problem of surface roughness which renders these methods ineffective for fabricating waveguide and non-waveguide based optical microsystems.

In order to overcome the problem of surface roughness identified during these micromachining processes, a novel hybrid micromachining technique has been proposed which involves controlled anisotropic etching on the previously etched surfaces so as to produce a smoother surface useful for optical MEMS applications. The validation of the hybrid micromachining process has been demonstrated by carrying out the process on samples previously etched with xenon difluoride and the study reveals a significant reduction in surface roughness due to the proposed hybrid micromachining technique.

The biophotonic testing experiments were carried out on MicraGeM waveguides in order to study the optical loss due to evanescence. However, before studying the evanescence loss, it was essential to calibrate the optical loss due to material absorption on the waveguides. Hence, absorption measurements were carried out for the enzyme-antibody using three spectrum of light which are the blue light at 470 nm, the red light at 635 nm and the infrared light at 1550 nm wavelengths. The test results and the inferences drawn from the results have been detailed in Chapter 5. The study on evanescence was carried out using the MicraGeM waveguides and the SOI anisotropic waveguides. The evanescence losses have been found and the evanescence coefficient for the different waveguide systems have been computed from the results.

BPM simulations were carried out for the waveguides which were tested for evanescence. It is not possible to simulate the exact conditions of evanescence which prevails during a reaction. However, with certain valid approximations, the BPM simulations were carried out for rectangular and anisotropic rib waveguide models and the evanescence phenomenon has been demonstrated by changing the index of the cladding material.

6.2 Future ideas

Through this work, the feasibility of fabricating a waveguide based biosensor on SOI platform for enzymatic detection has been demonstrated successfully. However, there are further improvisations which could be carried out on this work in order to improve upon the obtained results, as listed below:

1. Modeling of the index of bio-cladding has to be studied with the FD, FEM and BPM techniques.
2. Fabrication: There are numerous possibilities of fabricating waveguides based on different geometries through micromachining techniques like XeF_2 isotropic technique and DRIE. With better lithography techniques like the Direct Write Lithography (DWL), one could further miniaturize waveguide dimensions obtained in micromachining.
3. Testing: The biophotonic testing could be carried out on different enzymes and live cells, in order to verify the applicability the proposed biosensor for real-time applications. By incorporating a few modeling parameters, such as coupling loss, incidence angle, surface roughness parameters, etc., it is possible to improve the BPM simulations for computing the overall evanescent loss for the present system.

REFERENCES

[1] Defence Advanced Research Project Agency (DARPA), http://www.darpa.mil/MTO/MEMS.

[2] Arvind, C., and Muthukumaran, P., 2005, "MOEMS based integrated microfluidic fiber optic waveguide for biophotonic applications", *SPIE conference on "Optical Biochips and Biosensors for Nucleic Acids and Proteins*, Toronto, Canada, **5969**, pp 178-185.

[3] Bernard, L., W., and Richard, A. ,S., 1998, "Introduction to the Issue on Silicon-Based Optoelectronics", *IEEE Journal of selected optics in Quantum Electronics*, **4**(6), pp 897-898.

[4] de Dood, M., J., and Polman, A., July 2002, "Amorphous silicon waveguides for microphotonics" *Journal of applied physics*, **92**(2), pp. 649-653.

[5] Lee, K., K., and Lim, D., R., 2000, "Effect of size and roughness on light transmission in Si/SiO$_2$ waveguide: experiments and model" *Applied Physics letters*, **77**(11), pp. 1617-1619.

[6] Muthukumaran, P., Ion, S., and Luis, F., 2005, "Roughness characterisation of gas phase micromachining process suitable for fabrication silicon based microsystems" *International journal of manufacturing technology and management*, **7** (2/3/4), pp. 224-245.

[7] Parvesi, L., 2003, "Will silicon be the photonic material of the third millenium?" *Journal of Physics: Condensed Matter*, **15**, R1169–R1196.

[8] Bestwick, T., 1998, "ASOC- A Silicon-Based Integrated Optical Manufacturing Technology", *48th IEEE Conference on Electronic Components and Technology,* pp 566–571.

[9] Zimmermann, H., 2000, "Integrated Silicon Optoelectronics", *New York: Springer.*

[10] Fischer, U., Zinke, T., and Petermann, K., 1995, "Integrated optical waveguide switches in SOI," *Proceedings of IEEE International SOI Conference*, Tucson, AZ, pp. 141–142.

[11] Trinh, P., D., Yegnanarayanan, S., and Jalali, B., 1995, "Integrated optical directional couplers in silicon-on-insulator," *Electronics Letters*, **31**, pp 2097.

[12] Trinh, P., D., Yegnanarayanan, S., and Jalali, B., 1996, "5 x 9 integrated optical star coupler in silicon-on-insulator technology," *IEEE Photonic Technology Letter*, **8(6)**, pp 794–796.

[13] Pezeshki, B., Agahi, F., Kash, J., A., Welser,J., J., 1996, "Wavelength selective waveguide photodetectors in silicon-on-insulator," *Appied Phyics Letter*, **68** (6), pp. 741–743.

[14] Johnson, S., G., Villeneuve, P., R., Fan, S., Joannopoulos, J., D., 2000, "Linear waveguide in photonic crystal slabs" *Physical Review B (Condensed Matter and Materials Physics)*, **62**(12), pp 8212-8222.

[15] *Micralyne Inc*, 1911- 94 Street, Edmonton, Alberta Canada T6N 1E6, http://www.micralyne.com.

[16] Thevenot, D., R., Toth, K., Durst, R., A., Wilson, G.,S., 1999, "Electrochemical Biosensors: Recommended Definitions and Classification" *Pure and Applied Chemistry*, **71**, pp 2333–2348.

[17] Andrei, B., K., Maya, Z., Amir, L., Eugenii, K., Itamar W., "Enzyme monolayer-functionalized field-effect transistors for biosensor applications", *Sensors and Actuators B*, **70**, pp 222–231.

[18] Taitt, C., R., Anderson, G., P., Ligler, F., S., 2005, "Evanescent wave fluorescence biosensors", *Biosensors and Bioelectronics*, **20**, pp 2470–2487.

[19] Prasad, P., N., 2003, "Introduction to biophotonics", *New York: Wiley-Interscience.*

[20] Lin, C., H., Lee, G., B., Fuc, L., Chend, S., H., 2004, "Integrated optical-fiber capillary electrophoresis microchips with novel spin-on-glass surface modification" *Biosensors and Bioelectronics,* **20**, pp 83–90.

[21] Slavik, R., Homola, J., Ctyroky, J., 1999, "Single-mode optical fiber Surface Plasmon Resonance sensor" *Sensors and Actuators B,* **54**, pp 74-79.

[22] Robert, W., B., and John, E., H., 2001, "Sensitive disk resonator photonic biosensor", *Applied optics*, **40**(37), pp 5782.

[23] Chao, C., Y., and Guo, J., L., 2003, "Biochemical sensors based on polymer rings with sharp asymmetrical resonance", *Applied Physics Letters*, **83**(8), pp 1527-1529.

[24] Hilt, J., Z., Amit, G., Rashid, B., and Nicholas, A., 2003, "Ultra-sensitive biomems sensors based on Microcantilevers patterned with environmentally responsive hydrogels", *Biomedical Microdevices*, **5**(3) pp. 177-184.

[25] Jeetender, A., Muthukumaran, P., Ion, S., Balagopal, G., 2005, "Micro-electro-mechanical systems (MEMS) for enzymatic detection", *Proceedings of SPIE*, **5455**, pp 101-108.

[26] Vo-Dihn, T., Cullum, B., 2000, "Biosensors and biochips: advances in biological and medical diagnostics", *Journal of Analytical Chemistry,* **366**, pp-540–551.

[27] Marazuela, M., D., María, C., M., 2002, "Fiber-optic biosensors – an overview" *Bioanalytical chemistry*, **372**, pp 664–682.

[28] Wang, J., Rivas, G., Cai, X., Palecek, E., Nielsen, P., Shiraishi, H., Dontha, N., Luo, D., Parrado, C., Chicharro, M., Farias, P., Valera, F., S., Grant, D., H., Ozsoz M., Flair M., N., 1997, *Analytica Chimica Acta,* **347,** pp 1–8.

[29] Lechuga, L., M., Sepulveda, B., llobera, A., Calle, A., Dominiguez, C.,2003, "Integrated Optical silicon IC compatible nanodevices for biosensing applications", *Bioiengineered and bioinspired systems: Proceedings of SPIE ,* **5119,** pp 140-145.

[30] Mohammed, Z., and Nicholas, J., G., 2005, "Metal clad leaky waveguides for chemical and biosensing applications" *Biosensors and Bioelectronics*, **20**(9), pp 1718-1727.

[31] Mohammed Z., Stephan M., Bernard J., Treves B., Peter R., F, Martin B., and Nicholas J., G., 2005, "Bacteria detection using disposable optical leaky waveguide sensors" , *Biosensors and Bioelectronics*, **21**(2), pp 293-302.

[32] Jianming, Y., Mahmoud, E., S., 2003, "Fiber optic chemical sensor using polyaniline as modified cladding material", *IEEE sensors journal*, **3**(1), pp 5-12.

[33] Narang, U., Anderson, G., P., Ligler, F., S., Burans, J., 1997, "Fiber-optic based biosensor for ricin", *Biosensors and bioelectronics*, **12** (9-10), pp: 937-945.

[34] Saharudin, H., Alexey, V., N., Asim, K., R., 2003, "Optical biosensing transducer based on silicon waveguide structure coated with polyelectrolyte nano layers" *Bioengineered and bioinspired systems, Proceedings of SPIE*, **5119**, pp 100-107.

[35] Xiangji, Z., Mark, A., 1995, "Internal enzyme fiber-optic biosensors for hydrogen peroxide and glucose", *Analytica Chimica Acta*, **304**, pp 147 – 156.

[36] Hsin, Y., H., Yi, Y., H., 2004, " RCA combined nanoparticle based optical detection technique for protein microarray: a novel approach" *Biosensors and Bioelectronics,* **20**, pp 123-126.

[37] Brynda, E., Houska, M., Brandenburg, A., Wikerstal, A., 2002, "Optical biosensors for real-time measurement of analytes in blood plasma", *Biosensors and Bioelectronics,* **17**, pp 665 – 675.

[38] Kulagina, N., V., Lassman, M., E., Ligler, F., S., Taitt, C., R., 2005, "Antimicrobial peptides for detection of bacteria in biosensor assays", *Analytical Chemistry,* **77**(19), pp 6504-6508.

[39] Goldman, E., R., Mazirandeh, M., P., Mauro, J., M., King, K., D., Frey, J., C., Anderson, G., P., 2000, "Phage-displayed peptides as biosensor reagents", *Journal of Molecular Recognition*, **13**, pp 382–387.

[40] Jiří, H., Hana V., Jakub D., and Marek P., 2005, "Multi-analyte surface plasmon resonance biosensing methods", *Methods*, **37**(1), pp 26-36..

[41] Mark, P.,K., Romain, Q., Gonçal, B., and Marco, M.,P., 2006, "Quantitative detection of doping substances by a localised surface plasmon sensor", *Biosensors and Bioelectronics*, **21**(7), pp 1345-1349.

[42] Jeong-Woo, C., Young, K., Sun-Young, S., In-ho, L., 2003, "Optical biosensor consisting of glutathione-S-transferase for detection of captan", *Biosensors and Bioelectronics,* **18**, pp 1461-1466

[43] Ravi, S., K., Shuichi, T., 1999, "Patterning proteins and cells using soft lithography" *Biomaterials*, **20**, pp 2363-2376.

[44] Reid, N., O., Clark, T., G., and Craighead, H., G., 2003, "Avidin-biotin micropatterning for biosensor applications" *Biomedical devices,* **5**(1), pp 29-34.

[45] Kang, H., S., Hyun, S., K., Jinsoo, J., and Arthur, J., E., 2003, "All-polymer FET based on simple photolithographic micropatterning of electrically conducting polymer" , *Molecular crystal liquid Crystal,* **405**, pp-171-178,.

[46] Hilt, J., Z., Amit K., G., Rashid, B., and Nicholas, A., P., 2003, "Ultrasensitive Biomems sensors based on microcantilevers patterened with environmentally responsive hydrogels", *Biomedical microdevices*, **5**(3), pp 177-184.

[47] Antonios, D., Panagiotis, A., Constantinos, D., D., Konstantinos, M., Dimitra, D., and Kakabakos, E., 2001, "Photolithographic patterning of proteins with photoresists processable under biocompatible conditions", *Journal of Vacuum Science and Technology B,* **19** (6), pp 2820-2824.

[48] Sandeep K., S., Neeta, S., Ashok, K., 2003, "Biomolecules for development of biosensors and their applications", *Current Applied Physics,* **3,** pp 307–316.

[49] *Centre for Integrated Photonics*, United Kingdom. http://www.ciphotonics.com

[50] Kim, E., Xia, Y., Whitesides, G.M., 1995, "Polymer microstructures formed by moulding in capillaries", *Nature,* **376,** pp 581-584.

[51] Delamarche, E., Bernard, A., Schmid, H., Michel, B., Biebuyck, H., "Patterned delivery of immunoglobulins to surfaces using microfluidic networks" *Science* , **276,** pp 779-81.

[52] *MCNC Center for microelectronics systems technologies*, Research triangle park, NC 27709-2889.

[53] Zhang, Z., L., and MacDonald, N., C., 1992, "A RIE process for submicron silicon electromechanical structures," *Journal of Micromechanics and Microengineering*, **2** , pp 31-38.

[54] *Protolyne Microfluidic process technology*, www.micralyne.com/product_services/**protolyne**.htm.

[55] Lechuga, L., M., Sepúlveda, B., Llobera, A., Calle, A., and Domínguez, C., 2004, "Integrated micro- and nano-optical biosensor silicon devices CMOS compatible" *Proceedings SPIE - Integrated Optoelectronics Devices*, **5357**, pp 96 – 110.

[56] Avinash, K., B., 2003 "Synthesis of electrostatically actuated optical micromirrors", Masters Thesis, Concordia University.

[57] James, M., B., Howe, R., T., 1998, "Surface Micromachining for Microelectromechanical Systems", *Proceedings of IEEE*, **86**(8), pp 1552-1574

[58] Tang, W., C., Nguyen, C.,H., Howe, R.,T., 1989 "Laterally driven polysilicon resonant microstructures", *Sensors and Actuators A*, **20**, pp25–32.

[59] Nee, J., T., Conant, R., A., Muller ,R., S., Lau, K., Y., 2000, "Lightweight, optically flat micromirrors for fast beam steering", *IEEE/LEOS International Conference on Optical MEMS*, Piscataway, NJ, USA, pp. 9–10.

[60] Lee, K., B., Lin, L., 2002, "Electrolyte based on-demand and disposable microbattery", in: *Proceeding of the Fifteenth IEEE International Conference on Micro Electro Mechanical Systems*, Las Vegas, Nevada, USA, pp. 236–239.

[61] Lee, K., B., Sammoura, F., Lin, L., 2003, "Water activated disposable and long shelf life microbatteries", *16th IEEE International Conference on Micro Electro Mechanical System, MEMS*, Kyoto, Japan, pp. 387–390.

[62] Lee, K.,B., Lin, L., 2004, “Surface micromachined glass and polysilicon microchannels using MUMPs for BioMEMS applications”, *Sensors and Actuators A,* **111,** pp 44–50

[63] Sato, H., Homma, T., Kudo, H., Izumi, T., Osaka,T., Shoji, S., 2005, “Three-dimensional microfabrication process using Bi electrodeposition for a highly sensitive X-ray imaging sensor”, *Journal of Electroanalytical Chemistry,* **584** ,pp 28–33.

[64] http://www.mdl.sandia.gov/micromachine

[65] Sabat´e, N., Rubio, R., Calaza, C., Santander, J., Fonseca, L., Gr`acia, I., Can´e, C., Morenoa, M., Marcoa, S., 2005, “Mirror electrostatic actuation of a medium-infrared tuneable Fabry-Perot interferometer based on a surface micromachining process”, *Sensors and Actuators A*, **123–124** , pp 584–589

[66] Kwang, H., Kima, Y., S., Kangb, C., J., 2005, “Fabrication of piezoresistive microcantilever using surface micromachining technique for biosensors”, *Ultramicroscopy,* **105** (1-4), pp 223-227.

[67] Svenssony, L., Plaza, J., A., Benitez, M.,A., Esteve, J., and Lora-Tamayo, E., 1996, “Surface micromachining technology applied to the fabrication of a FET pressure sensor” *Journal of Micromechanics and Microengineering*, **6**, pp 80–83

[68] Jang, W., I., Choi, C., A., Jun, C., H., Kima, Y.,T., Esashi, M., 2004, “Surface micromachined thermally driven micropump”, *Sensors and Actuators A,* **115,** pp 151–158.

[69] http://www.microfab.de/technologies/surfacemm.htm

[70] Howe, R.,T., Boser, B., E., and Pisano, A., P., 1996, “Polysilicon integrated microsystems: technologies and applications,” *Sensors Actuators A*, **56**, pp. 167–177.

[71] Core, T., A., Tsang, W.,K., and Sherman, S.,J., 1993, "Fabrication technology for an integrated surface-micromachined sensor," *Solid State Technology,* **36**(10), pp. 39–47.

[72] Howe, R.,T., 1995, "Polysilicon integrated microsystems: Technology and applications," in *Proceedings of the 8th international conference on Solid-State Sensors and Actuators (Transducers 95),* Stockholm, Sweden, pp. 43–46.

[73] Kovacs, G.,T., 1998, "Micromachined transducers source handbook", WCB/McGraw Hill.

[74] *McDonald research group*, Cornell University.

[75] Hukai, X., and Lars, E., 2002, "Post CMOS processing for High Aspect ratio Integrated Silicon Microstructures", *Journal of Microelectromechanical systems*, **11**(2), pp. 93-101.

[76] Cochran, K., R., Fan, L., deVoe, D.,L., 2005, "High power optical microswitch based on direct fiber attenuation" *Sensors and Actuators A*, **119**, pp 512-519.

[77] Fujita, H., 2001, "MEMS/MOEMS application to optical communication", *Reliability, testing and characterization of MEMS, MOEMS, Proceedings of SPIE*, San Francisco, **4588**, pp 11-17.

[78] Kovacs, G.,T., Maluf, N.,E., and Petersen, K.,E., 1998, "Bulk Micromachining of silicon" *Proceedings of the IEEE*, **86**(8), pp. 1536-1551.

[79] Sharath, C., and Sriram, S., 2004, "Effect of microfabrication processes on surface roughness parameters of silicon surfaces", *Surface and coatings technology*, **188-189**, pp 581-587.

[80] Chan, W.T., Brown, K.B., Lawson, P.W., Robinson, A.M., Yuan, M. and Strembicke, D., 1999, "Gas Phase Pulse Etching of Silicon For MEMS With Xenon

difluoride" *Proceedings of the IEEE Conference on Electrical and Computer Engineering*, Edmonton, Alberta, Canada, pp 1637-1642.

[81] Winters, H., F., and Coburn, J., W., 1979, "The etching of silicon with XeF_2 vapor", *Applied Physics Letters*, **34**(1), pp. 70-73.

[82] Toda, R., Minami K., Esashi, M., 1998, "Thin beam bulk micromachining based on RIE and xenon difluoride silicon etching", *Sensors and Actuators A*, **66**, pp 268-272.

[83] Giesler, J., O'Malley, G., Williams, M., and Machuga, S., 1994, "Flip Chip on Board Connection Technology: Process Characterization and Reliability," *IEEE Trans. Components, Packaging, and Manufacturing Technology*, **17**(3:8), pp. 256-263,

[84] Richard Gerke, 2006, "MEMS and Microstructures in Aerospace Applications", *CRC Press*, Taylor & Francis Group, LLC.

[85] *Intellisense Software*, www.intellisensesoftware.com.

[86] Saleh, B., A., Teich, M., C., 1991, "Fundamentals of Photonics", *Wiley Interscience.*

[87] Allan, W., S., and John, D., L., 1983, "Optical waveguide theory", *Chapman and Hall.*

[88] Jianming, Y., and Mahmoud A., S., 2003, "Fiber-Optic Chemical Sensor Using Polyaniline as Modified Cladding Material", *IEEE Sensors Journal*, **3**(1), pp 5-12.

[89] Cao, W., Duan, Y., 2005, "Optical fiber-based evanescent ammonia sensor", *Sensors and Actuators B*, **110,** pp 252–259.

[90] Lechuga, L., M., Borja, S., Jose, S., Francisco, B., Ana, C., Carlos, D., 2004, "Integrated micro- and nano-optical biosensor silicon devices CMOS compatible" Proceedings of SPIE, **5357,** pp 96-110.

[91] Scarmozzino, R., Gopinath, A., Pregla, R., Helfert, S., 2000,"Numerical techniques for modeling guided wave photonic devices.", *IEEE journal in Quantum electronics*, **6**(1), pp 150-162.

[92] Delage, A., 1991, "Modelling of semiconductor rib waveguides by a finite difference method", *Canadian Journal of Physics*, **69**, pp 512–519.

[93] FEMLAB v 3.1, www.comsol.com

[94] R-Soft Beam PROP v 6.0.1, www.rsoftdesign.com

[95] Benson, T., M., Sewell, P., Kendall, P.,C., Sujecki, S, 1999, "Finite difference methods in optoelectronic simulation" *International Conference on Transparent Optical Networks*, pp 47 – 48.

[96] Shibayama, J., Yamahira, A., Mugita, T., Yamauchi, J., Nakano, H., 2003, "A finite-difference time-domain beam-propagation method for TE- and TM-wave analyses" *Journal of Lightwave Technology*, **21**(7), pp 1709 – 1715.

[97] Robertson, M.J., Ritchie, S., and Dayan., P., 1985 "Semiconductor waveguides: analysis of optical propagation in single rib structures and directional couplers" *IEE proceedings*, **132** (6) , pp 336-342.

[98] Powell, O., 2002, "Single Mode condition for silicon rib waveguides", *Journal of Lightwave technology*, **20** (10), pp1851-1855.

[99] Reddy, C.,J., Manohar, D., D., Cockrell, C., R., and Fred B., B., 1994, "Finite Element Method for Eigenvalue Problems in Electromagnetics", *NASA technical paper, 3485.*

[100] Rodriguez, 2005, “An Improvement of the Finite-Element Method for computing the Electric Field of waveguides with complex geometry” *Mathematical and Computer Modelling,* **41,** pp 791-805.

[101] Giguere, P., A., “Properties of Hydrogen Peroxide”, *Canadian Journal for Research*, **21B**, 156, 1943.

[102] Schulz, D., Glingener, C., E., 1994, “Novel Generalized Finite-Difference Beam Propagation Method”, *IEEE Journal of Quantum Electronics*, **30**(4), pp 1132- 1140.

[103] Ilic, I., Scarmozzino, R., Osgood Jr., R., Yardley, J.,T., Beeson, K.,W., and M. J. McFarland, 1994, “Modeling multimode-input star couplers in polymers” *Journal of Lightwave Technology*, **12**(6), pp 996-1003.

[104] Scarmozzino, R., Osgood Jr., R., M., Eldada, L., Yardley, J.,T., Liu, Y., Bristow, J., Stack, J., Rowlette, J., and Liu, Y.,S., 1997, “Design and fabrication of passive optical components for multimode parallel optical links,” in *Proceedings of SPIE Photonic West Meeting*, **3005**, p. 257.

[105] Koshiba, M., 2001, “Wavelength Division Multiplexing and Demultiplexing With Photonic Crystal Waveguide Couplers”, *Journal of Lightwave Technology*, **19**(12), pp 1970-1975.

[106] Hu, M., Huang, J.,Z., Scarmozzino, R., Levy, M., and Osgood Jr., R.,M., 1997, “Tunable Mach–Zehnder polarization splitter using height-tapered y-branches,” *Photonic. Technology Letters*, **9**, pp. 773–775.

[107] Elson, J., M., 2001, “Propagation in planar waveguides and effect of wall roughness”, *Optics Express*, **9**(9), pp. 461-475.

[108] Payne, F., P., and Lacey, J., P., 1994, "A theoretical analysis of scattering loss from planar optical waveguides", *Optical and Quantum Electronics*, **26**, pp 977-986.

[109] Grillot, F., 2004, "Size influence on the propagation loss induced by sidewall roughness on ultrasmall SOI waveguides", *IEEE Photonics technology letters*, **16**(7), pp.1661-1663.

[110] Cornel, M., Christian, T., 1997, "Vertical mirrors fabricated by Deep Reactive Ion Etching for Fiber-Optic Switching Applications", *Journal of Microelectromechanical Systems*, **6**(3), pp 277-285.

[111] *MEMS Pro v 3.1*, Tanner Research Inc., CA, USA, http:// www.tanner.com

[112] Sakaino, K., Adachi, S., 2001, "Study of Si (100) surfaces etched in TMAH solution", Sensors and Actuators A, **88**(1) pp 71-78.

[113] Yan, G., Chan, C.,H., Hsing, I., M.,2001, "An improved TMAH Si-etching solution without attacking exposed Aluminium", *Sensors and Actuators A,* **89**, pp.135-141.

[114] Landsberger, L., Kharizi, M., Pranjape, M., 1996, "On hillocks generated during anisotropic etching of silicon in TMAH*", Journal of Microelectromechanical Systems,* **5**(2), pp 106-116.

[115] http://www.cise.columbia.edu/clean/ process/

[116] *Centre Typo*, 1000, Rue Wellington, Montreal QC, H3C1T8.

[117] *Typo Express*, 1645 de Maisonneuve Blvd. (O), #301, Montreal, QC, H3H2N4.

[118] *Fine-line Imaging*, 204, Mountview Lane, Ste# 3 Colorado Springs, CO 80907 Colorado.

[119] Shikida, M., Masuda, T., Uchikawa, D., and Sato, K., 2001, "Surface roughness of Single-crystal silicon etched by TMAH solution", *Sensors and Actuators A*, **90**, pp 223-231.

[120] Muthukumaran, P., 2000, "Boundary conditioning concept applied to the synthesis of microsystems using fuzzy logic approach", Ph.D Thesis, *Concordia University*, Montreal.

[121] Lee, K., K., and Lim, D., R., 2000, "Effect of size and roughness on light transmission in Si/SiO_2 waveguide: experiments and model", *Applied Physics letters*, **77**(11), pp. 1617-1619.

[122] Divan, R., Moldovan, N., and Camon, H., 1999, "Roughening and smoothening dynamics during KOH silicon etching", *Sensors and Actuators A*, **74**, pp 18-23.

[123] Resnik, D., Vrtacnik, D., Aljancic, U., and Amon, S., 2003, "Effective roughness reduction of {100} and {311} planes in anisotropic etching of {100} silicon in 5% TMAH", *Journal of Micromechanics and Microengineering*, **13**, pp 26-34.

[124] Aalto, T., Harjanne, M., Kapulainen, M., Heimala, P. and Leppihalme, M., 2004, "Development of Silicon-on-insulator waveguide technology", *Proceedings of SPIE* - The International Society for Optical Engineering, Integrated Optics: Devices, Materials, and Technologies VIII, **5355**, pp. 81-95.

[125] Jeetender, A., Ion, S., and Muthukumaran, P., 2005, "Micro-opto mechanical biosensors for troponin detection", *SPIE conference on "Optical Biochips and Biosensors for Nucleic Acids and Proteins*, Toronto, Canada. **5969**, pp 186-196.

[126] Motomasa, T., Koji, M., Shiro, Y., Satoshi, T., Koichiro, I., Hiroshi, H. , and Isao, M., 2003, "Activation of Hydrogen Peroxide in Horseradish Peroxidase Occurs within

~200 ms Observed by a New Freeze-Quench Device", *Biophysical Journal,* **84**, pp 1998–2004

[127] Robert, K., 1981, "Substituted Hemin as Probes for Structure-Function Relationships in Horseradish Peroxidase", *Journal of biological chemistry,* **256**(13), pp. 6903-6912.

[128] Bin, L., Emmanuel, I.,I., Malcolm, R.,S., Richard, O.,K., 1997, "Effects of acetonitrile on horseradish peroxidase (HRP)-anti HRP antibody interaction, *Biosensors & Bioelectronics,* **12**(7), pp. 619-625.

[129] Haesun, K., B., and Harold V., W., 1989, "Elementary Steps in the Formation of Horseradish Peroxidase Compound I: Direct Observation of Compound 0, a new intermediate with a Hyperporphyrin Spectrum", *Biochemistry*, **28**(57), pp 5714-5719.

[130] Masaru, A., Daisuke, T., Masami, K., Hideu, K., 2001, "Structural change and catalytic activity of Horseradish Peroxidase in oxidative polymerization of phenol", *Biosciences, Biotechnology and Biochemistry*, **65**(7), pp1581-1588.

Appendix 1

MicraGeM process overview

The SOI MicraGeM process technology is an industry defined microfabrication technology available to the Canadian universities through the CMC. This process has been used to fabricate rectangular waveguides of different dimensions which have been tested for biosensing through evanescence. Other waveguide devices such as the Mach-Zehnder Interferometer, Photonic crystals and tapered waveguides have also been fabricated along with the microfluidic pump.

The MicraGeM devices consist of Silicon on Insulator structures bonded on pyrex. The other layers used in the process, and their specifications are tabulated in Table A1.

Table A1.1: Different material layers used in the MicraGeM process

Layer	Description
Pyrex	525 μm thick 7740 pyrex wafer is used. The cavities etched on the pyrex can have the depths of 2 μm, 10 μm or a combination of both giving 12 μm etch depth.
Metal 1	This layer consists of 50 nm Titanium, 50 nm Platinum and 200 nm Gold.
SOI wafer	The SOI wafer consists of a 525 μm thick Single Crystal Silicon (SCSi) handle layer , SCSi device layer of 10 μm thickness and sufficient buried oxide layer separating them.
Metal 2	This layer consists of 100 Å thick Chrome and 750 Å thick Gold.

A1.1 Process flow

Figure A1 represents schematically the process flow for the MicraGEM prototyping process for fabrication of a device.

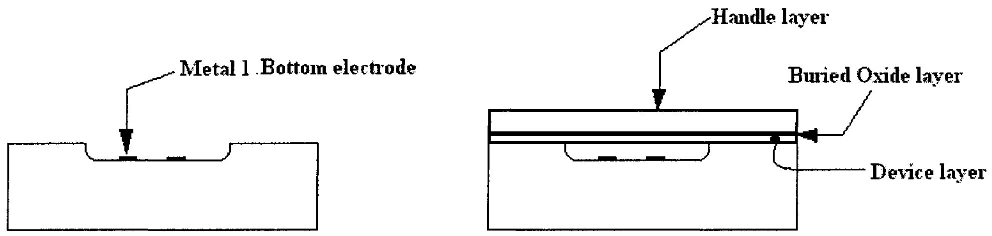

Step 1 : Pyrex etching and deposition of Metal 1 Step 2: Anodic bonding of SOI wafer to Pyrex

Step 3: Removal of handle layer and oxide in SOI Step 4: Patterning of Silicon and deposition of Metal 2.

Figure A1: Process flow of MicraGEM prototyping technique

A detailed process description for fabrication of a device with this technology is as given below:

1) On a Pyrex wafer, cavities are etched which form the gap between the SOI wafer and the bottom electrode. The depth of the cavities may be 2 μm, 10 μm or a combination of both of them to give 12 μm. Inside these pyrex cavities, metal electrodes (METAL 1), lines and bond pads for METAL 1 are patterned by the lift-off technique so as to form the bottom electrode.

2) Following the METAL 1 patterning, anodic bonding of a SOI wafer is carried out on top of the pyrex with the device layer of the SOI down. Herein, no bond alignment and

hence no compensation in design is required between the membrane and the bottom electrode.

3) The handle layer and the buried oxide layer of the SOI wafer are then etched away, so that the specimen is now left with the single crystal silicon membrane over the cavities on the pyrex wafer.

4) Low stress metal (METAL 2) is now deposited on the silicon and are etched with a wet etch process after lithographic patterning to expose the silicon.

5) Finally, DRIE with lithographic patterning is carried out in order to release the microstructures. The wafers are then diced and the final structures are revealed.

Appendix 2

Preparation of Horseradish Peroxidase

Horse Radish Peroxidase has been used as the protein for biophotonic testing of the waveguides through the principle of evanescence. This enzyme produces an instantaneous reaction upon introduction to its antibody Hydrogen Peroxide. The procedure for preparing the HRP in the required molar concentration is explained as below.

A2.1 Preparation of Phosphate Buffer Solution (PBS)

Initially, the potassium phosphate buffer solution is prepared. Potassium hydrogen Phosphate (K_2HPO_4) is a white powder in appearance whose molecular weight is 174.18 gram per mol. The number of moles of Potassium Phosphate to be added to prepare 0.1M of the buffer solution is given by the formula

$$\text{No. of moles} = (\text{weight in grams} / \text{Molecular weight}) \quad \text{(A2.1)}$$

In order to prepare 0.1 M buffer, i.e, 0.1 mole of Potassium Phosphate in 1 litre of the solution, 8.71 g of Potassium Phosphate is added to 500 ml of water. A slightly hazy colorless solution of PBS is produced and this solution is diluted with strong hydrochloric acid (HCl) in order to obtain a buffer solution with a pH of 6.0. The pH of the solution is measured using a pH meter.

A2.2 Preparation of HRP

Solid HRP is taken in a pan and weighed in physical balance. The buffer solution is added to HRP to get a liquid solution of the enzyme with a pH of 6.0. A clear amber brown solution of HRP is obtained at 10 mg per 1 ml of 0.1M potassium phosphate.

The activity of HRP is measure in terms of 'units'. In the present case, 1 mol HRP reacts with 1 mol H_2O_2 to form 1 mol of water and ½ mol of oxygen. The reduction reaction is given as per the equation

$$H_2O_2 \rightarrow H_2O + (1/2)\, O_2 \qquad (A2.2)$$

The oxygen released during this reaction is made to react with another specimen to form a separate compound through an oxidation reaction. By knowing the number of moles of the newly formed compound, the number of moles of oxygen released during the reaction is obtained, which is equivalent to the number of moles of HRP reacted with H_2O_2.

In order to find out the activity of the HRP in the buffer solution, the oxygen released during the reaction is made to react with Pyrogallol. During this reaction, Pyrogallol forms Purpurogallin and the number of moles of Purpurogallin is measured. 1 unit of HRP activity is equivalent to 1.0 mg Purpurogallin obtained from Pyrogallol in 20 sec for pH of 6.0 at 20°C. Thus for the sample prepared in the procedure mentioned above, an enzymatic activity of 250 to 330 units per mg solid HRP is obtained [125].